Imaging via photon-photon correlation of X-ray fluorescence

Dissertation zur Erlangung des Doktorgrades
an der Fakultät für Mathematik, Informatik und Naturwissenschaften
der Universität Hamburg

vorgelegt von

Fabian Trost

2023

Gutachter der Dissertation:	Prof. Dr. Dr. Henry N. Chapman Prof. Dr. Ralf Röhlsberger
Zusammensetzung der Prüfungskommission:	Prof. Dr. Arwen Pearson Prof. Dr. Tais Gorkhover Prof. Dr. Dr. Henry N. Chapman Prof. Dr. Ralf Röhlsberger Dr. Andrei Benediktovitch
Vorsitzende/r der Prüfungskommission:	Prof. Dr. Arwen Pearson
Datum der Disputation:	18.09.2023
Vorsitzender Fach-Promotionsausschuss PHYSIK:	Prof. Dr. Günter H. W. Sigl
Leiter des Fachbereichs PHYSIK:	Prof. Dr. Wolfgang J. Parak
Dekan der Fakultät MIN:	Prof. Dr.-Ing. Norbert Ritter

Abstract

This work discusses and demonstrates the imaging method 'photon-photon correlation of X-ray fluorescence', also called 'Incoherent Diffraction Imaging (IDI)'. This method corresponds to the 'intensity interferometry', known from astronomy. However, this method requires measurement or exposure times that are on the order of the coherence time of the measured radiation; for K_α fluorescence of light transition metals, this is on the order of a femtosecond – a temporal length that can be achieved by modern X-ray free electron lasers (XFELs).

In addition to the exposure time requirement, this work discusses other influencing factors that can cause a reduction in the useful correlation signal. These are the temporal shape of the excitation pulse, the sample size, the (non) polarization of the detected photons, and others. These factors, collectively called 'visibility factor', also manifest as 'speckle contrast' and can be measured without the need to perform intensity correlation. A weighting method is presented to determine the speckle contrast from a data set consisting of images with very low photon counts that fluctuate significantly from image to image. This method is applied to compare the speckle contrast of iron K_α fluorescence excited by $3\,\mathrm{fs}$ and $15\,\mathrm{fs}$ XFEL pulses. An increase in speckle contrast was found for the short pulses compared to the longer ones – a fundamental requirement for the IDI method.

Furthermore, inherent noise sources affecting the IDI are discussed. A model is derived to estimate the dependence of the signal-to-noise ratio (SNR) on the photon number per pixel, temporal coherence (or visibility factor), and the shape of the imaged object. In addition, simulations in two and three dimensions were performed to validate the model's predictions. Unlike coherent imaging methods, more detected photons do not always result in higher SNR. Moreover, larger and more complex objects generally yield poorer SNR, even when the number of measured photons is proportional to the object size or complexity.

Finally, an experiment that uses the photon-photon correlation of X-ray fluorescence photons for the first time to reconstruct a nontrivial (noncontinuous) fluorescence emitter distribution is presented. In the course of this experiment, the application of IDI to determine XFEL beam parameters such as focus and temporal pulse length is demonstrated.

Zusammenfassung

In dieser Arbeit wird die Bildgebungsmethode der “Photon-Photon Korrelation von Röntgenfluoreszenz”, auch “Incoherent Diffraction Imaging (IDI)” genannt, diskutiert und demonstriert. Diese Methode entspricht der aus der Astronomie bekannten “Intensitätsinterferometrie”. Diese Methode setzt jedoch Mess-, bzw. Belichtungszeiten voraus, die sich in der Größenordnung der Kohärenzzeit der gemessenen Strahlung befinden; für K_α Fluoreszenz leichter Übergangsmetalle befindet sich diese in der Größenordnung von einer Femtosekunde – eine zeitliche Länge die von modernen Freie Elektronen Röntgen Laser (XFELs) erreicht werden kann.

Neben der Anforderung an die Belichtungszeit werden weitere Einflussfaktoren diskutiert, die eine Reduzierung des brauchbaren Korrelationssignals bewirken können. Diese sind z.B. die zeitliche Form des Anregungspulses, die Größe der Probe, die (nicht) Polarisation der detektierten Photonen und Weitere. Diese Faktoren, zusammengefasst “Visibilitätsfaktor” genannt, manifestieren sich auch als “Specklekontrast” und können gemessen werden, ohne das eine Intensitätskorrelation durchgeführt werden muss. Es wird eine Gewichtungsmethode vorgestellt, um den Specklekontrast von einem Datenset bestehend aus Aufnahmen mit sehr niedriger, aber von Aufnahme zu Aufnahme stark fluktuierender Photonenzahl zu ermitteln. Diese Methode wird angewandt, um den Specklekontrast von Eisen K_α Fluoreszenz, angeregt durch $3\,\mathrm{fs}$ und $15\,\mathrm{fs}$ XFEL Pulsen, zu vergleichen. Dabei wurde eine Erhöhung des Specklekontrast bei den kurzen Pulsen gegenüber den längeren festgestellt, was eine elementale Voraussetzung für die IDI Methode darstellt.

Des Weiteren werden in dieser Arbeit inhärente Rauschquellen, welche die IDI beeinflussen, diskutiert. Hierfür wird ein Modell hergeleitet, um die Abhängigkeit des Signal-Rausch-Verhältnisses (SNR) von der Photonenzahl pro Pixel, der zeitlichen Kohärenz (bzw. des Visibilitätsfaktors) und der Form des abgebildeten Objekts abzuschätzen. Zusätzlich wurden Simulationen in zwei und drei Dimensionen durchgeführt, um die Vorhersagen des Modells zu validieren. Es stellt sich heraus, dass, im Gegensatz zu kohärenten Abbildungsmethoden, mehr detektierte Photonen nicht immer zu einer höheren SNR führen. Außerdem liefern größere und komplexere Objekte im Allgemeinen eine niedrigere SNR, selbst wenn die Anzahl gemessener Photonen proportional zur Objektgröße bzw. Komplexität steigt.

Abschließend wird ein Experiment vorgestellt, in dem erstmalig die Korrelation von Röntgenfluoreszenz Photonen verwendet wird, um eine nicht triviale (nicht durchgängige) Fluoreszenz Emitter Verteilung zu rekonstruieren. Im Zuge dieses Experiments wird auch die Anwendung von IDI demonstriert, um XFEL Strahlparameter wie den Fokus und die zeitliche Pulslänge zu bestimmen.

Contents

Nomenclature

Frequently used constants, symbols and abbreviations.

Abbreviations

ADU	arbitrary detector unit
CDI	coherent diffraction imaging
FEL	free electron laser
FWHM	full width at half maximum
IDI	incoherent diffraction imaging
RMS	root mean square
SASE	self-amplified spontaneous emission
SNR	signal-to-noise ratio
SOR	signal-to-offset ratio
XFEL	X-ray free electron laser

Physics constants

c_0	vacuum speed of light	$2.998 \times 10^8\,\mathrm{m\,s^{-1}}$
$h = 2\pi\hbar$	Planck constant	$4.136 \times 10^{-15}\,\mathrm{eV\,s}$

Mathematical notations

$\hat{e}$	unity vector	$\hat{e}_x := \frac{\vec{x}}{\lvert\vec{x}\rvert}$
$\vec{a} \cdot \vec{b}$	scalar product	$\vec{a} \cdot \vec{b} := \sum_j a_j b_j$
$\vec{a} \times \vec{b}$	cross product	$\vec{a} \times \vec{b} = (a_2b_3 - a_3b_2)\hat{e}_1 + (a_3b_1 - a_1b_3)\hat{e}_2 + (a_1b_2 - a_2b_1)\hat{e}_3 \,\forall\, \vec{a}, \vec{b} \in \mathbb{R}^3$
x	modulus (shortcut)	$x := \lvert\vec{x}\rvert$
∇	Nabla operator	$\nabla := \sum_j \frac{\partial}{\partial x_j}\hat{e}_j$

$\mathfrak{Re}\,(z)$	real part	$\mathfrak{Re}\,(a+ib) := a \,\forall\, a,b \in \mathbb{R}$
$\mathfrak{Im}\,(z)$	imaginary part	$\mathfrak{Im}\,(a+ib) := b \,\forall\, a,b \in \mathbb{R}$
z^*	complex conjugate	$(a+ib)^* := (a-ib) \,\forall\, a,b \in \mathbb{R}$
$\delta_{a,b}$	Kronecker delta	$\delta_{a,b} = 1$ if $a = b$ else 0
$\delta(\vec{x})$	delta distribution	$\int_{-\infty}^{\infty} \delta(\vec{x}-\vec{a}) f(\vec{x})\, d^n x = f(\vec{a})$
$\Theta(x)$	Heaviside step function	$\Theta(x) = 1$ if $x > 0$ else 0
$\langle f(x) \rangle_x$	average	$\langle f(t) \rangle_t := \lim_{T\to\infty} T^{-1} \int_{-T/2}^{T/2} f(t)\, dt$
$\mathfrak{F}\left[f(\vec{x})\right](\vec{q})$	Fourier transform	$\mathfrak{F}\left[f(\vec{x})\right](\vec{q}) := \int_{-\infty}^{\infty} f(\vec{x}) e^{i\vec{x}\cdot\vec{q}}\, d^n x$
$f * g$	convolution	$(f(t) * g(t))(\tau) := \int_{-\infty}^{\infty} f(\tau) g(t-\tau)\, dt$
$f \star g$	cross-correlation	$(f(t) \star g(t))(\tau) := \int_{-\infty}^{\infty} f^*(t') g(\tau+t')\, dt'$
$\mathrm{erf}(z)$	error function	$\mathrm{erf}(z) := \frac{2}{\sqrt{\pi}} \int_0^z e^{-t^2}\, dt$
$\mathrm{erfc}(z)$	complementary error function	$\mathrm{erfc}(z) := 1 - \mathrm{erf}(z)$

1 Introduction

Since the discovery of X-rays by Wilhelm Conrad Röntgen in 1895 [101], imaging technology has seen numerous breakthroughs. X-rays, with their very short wavelengths, can be used to image complex structures at atomic resolution. One such imaging technique is X-ray crystallography [7, 69], which has been used to determine the structures of various materials, including minerals and alloys. It has also revolutionized the study of biological molecules, such as proteins [62], vitamins [71], and DNA [23], by revealing their structure and function. X-ray crystallography is based on coherent X-ray diffraction and can be summarized as *coherent diffraction imaging (CDI)* alongside other X-ray techniques [10, 91]. In CDI, the energy of the photons and a fixed phase relation between the incoming and scattered wave field is maintained. The probability of a photon being coherently scattered by an atom is proportional to the cross-section for elastic scattering. Such a cross-section is plotted in Fig. 1.1 as a function of the incoming photons' energy. Besides the cross-section for elastic scattering, the cross-sections for Compton scattering and the photo effect are plotted. Apparently, the cross-section of the photo effect is much higher than for the elastic scattering at all relevant energies. The photo effect describes the emission of an electron from an atom after a photon is absorbed and its kinetic energy is transferred to the electron. In Fig. 1.1, a sharp edge is apparent at $7.1\,\mathrm{keV}$, where the ejection of an electron from the innermost shell becomes possible. The emerging hole in this shell is quickly filled by an electron from a higher shell, which can lead to the emission of a photon – a process called fluorescence. Fluorescence photons are mutually incoherent and thus do not contribute to the CDI signal; instead, they are generally viewed as disturbing background. This raises the question, whether the incoherently emitted fluorescence photons can also be utilized for imaging. We will address this in a moment.

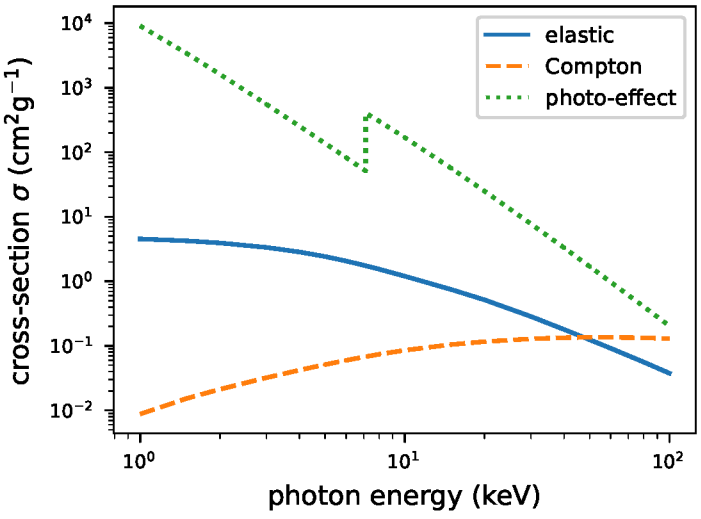

Fig. 1.1.: Cross sections of iron for elastic (coherent) scattering, Compton scattering, and photo absorption (photo-effect). The latter can lead to X-ray fluorescence. The data is taken from [109].

In 1954, Robert Hanbury Brown and Richard Q. Twiss proposed and demonstrated a method called *intensity interferometry* which was used in radio astronomy to measure the angular extent covered by a star [50, 46]. This method relies on the correlation of measured intensities (second-order correlation) instead of wave-field amplitudes (first-order correlation), as it is the case in classical radio astronomy. One consequence of the intensity-intensity correlation is that a spatial coherence of the measured radiation is not required. This has the advantage that the measurements are not sensitive to random phase shifts in the wave field as, for example, introduced by fluctuating densities in the atmosphere. Later, Hanbury Brown and Twiss (HBT) demonstrated that intensity interferometry is not restricted to radio waves but also works for visible light [47].

This demonstration of intensity interferometry was of great importance to quantum optics since it requires the interference of at least two photons. It contradicted the then-current view by Paul Dirac that "each photon [...] only interferes with itself" [18]. The first quantum mechanical explanation was given by Ugo Fano [29]. He investigated the case of two photons theoretically, each emitted by an independent emitter (e_1 and e_2) and detected by two spatially separated detectors (d_1 and d_2), detecting one photon each. When the paths of the photons are not distinguishable, and it is thus impossible to say whether detector d_1 detected the photon from e_1 or e_2, the quantum paths do interfere. In 1963, Roy J. Glauber published his groundbreaking work "The Quantum Theory of Optical Coherence" [39], thoroughly explaining interference phenomena, including the higher-order interference observed by Hanbury Brown and Twiss.

Intensity interferometry requires correlations on timescales in the order of the coherence time of the wave fields. Hanbury Brown and Twiss archived this by a sufficiently high temporal resolution of the intensity-intensity correlator. Furthermore, they increased the coherence time of the radio waves by applying a narrow frequency band filter [124].

Returning to X-ray fluorescence: if we want to utilize intensity interferometry here, we face the challenge of the coherence time being usually quite short. For example, the K-shell fluorescence of light transition metals usually has a coherence time of less than $1\,\mathrm{fs}$ [67]. Since, up to this day, the temporal resolution of the most advanced X-ray detectors is not even close to this time scale [73], sufficiently fast coincidence detection is not an option. However, current X-ray free-electron lasers (XFEL) can generate high-intensity pulses with a duration in the femtosecond range [84] and have even managed to produce pulses of tenths of attoseconds [61, 72, 97]. Such short excitation pulses enable intensity interferometry for X-ray fluorescence. Anton Classen et al. first proposed using these short pulses for intensity interferometry in 2017. They called the method *incoherent diffraction imaging (IDI)* to emphasize the X-ray fluorescence's incoherent nature and to distinguish it from CDI.

IDI has interesting features, such as sub-Abbe resolution [116] and element-specific sensitivity [53]. Therefore, it has the potential to complement CDI. Also, due to its dependence on the excitation pulse length, IDI can be used for characterizing XFEL pulses, as first demonstrated by Ichiro Inoue [58] in 2019.

In the present work, we will comprehensively discuss the properties of IDI and present the first successful experiment of imaging a non-trivial distribution of fluorescent emitters via IDI. We will introduce the basics of CDI, IDI, and photon statistics of various light sources in Chapter 2. In Chapter 3, an experimentally observed change in speckle contrast for different XFEL pulse durations is reported, an essential requirement for the feasibility of IDI. We will also discuss the parameters influencing the speckle contrast, which are crucial for IDI's signal strength. Chapter 4 is about IDI's signal-to-noise ratio (SNR), highlighting the substantial differences to CDI and the implications for possible experiments. The demonstration of an IDI experiment, imaging a simple yet non-trivial emitter distribution, is reported in Chapter 5. Also, the determination of the XFEL pulse properties, namely temporal pulse length and spatial focus size, is reported. A summary of this work and an outlook on possible further applications and experiments are given in Chapter 6.

Even though this work is focused on IDI via X-ray fluorescence, many of the concepts presented, especially about the SNR, apply to intensity interferometry in general and, thus, also yield implications for applications, e.g., in astronomy.

2 Basics

In this chapter we provide a brief overview of some fundamental concepts in classical and quantum optics. As these concepts are well-established and widely covered in textbooks [6, 96, 79, 40, 41, 75, 107, 128], we will provide a concise summary without delving into extensive detail.
We will also go through the basics of *incoherent diffraction imaging (IDI)*, also known as intensity interferometry of fluorescence correlation imaging.

2.1 Electromagnetic waves

The field of (classical) optics is based on the well-known microscopic Maxwell's equations [83]. These equations describe the interaction between free charges and the electric field, the interaction between free currents and the electric field, and the interaction between the electric and magnetic fields:

$$\begin{aligned} \nabla \cdot \vec{E} &= \frac{\rho_{\text{free}}}{\epsilon_0}\,, & \nabla \times \vec{E} &= -\frac{\partial}{\partial t}\vec{B}\,, \\ \nabla \cdot \vec{B} &= 0\,, & \nabla \times \vec{B} &= \mu_0 \vec{j}_{\text{free}} + \frac{1}{c_0^2}\frac{\partial}{\partial t}\vec{E}\,, \end{aligned} \tag{2.1}$$

where the electric field is represented by $\vec{E}$, the magnetic field by $\vec{B}$; c_0, ϵ_0, and μ_0 denote the vacuum speed of light, vacuum permittivity, and vacuum permeability, respectively[1]. To set up the wave-equation, we assume that there are neither free charges ($\rho_{\text{free}} = 0$) nor free currents ($\vec{j}_{\text{free}} = 0$). Using the vector relation[2] $\nabla \times \left(\nabla \times \vec{A}\right) = \nabla \cdot \left(\nabla \cdot \vec{A}\right) - \triangle \vec{A}$, we obtain the free wave equations as

$$\begin{aligned} \frac{1}{c^2}\frac{\partial^2}{\partial t^2}\vec{E} - \triangle \vec{E} &= 0\,, \\ \frac{1}{c^2}\frac{\partial^2}{\partial t^2}\vec{B} - \triangle \vec{B} &= 0\,. \end{aligned} \tag{2.2}$$

In this work, we only consider the electric field for simplicity. A simple solution to the wave equation is the plane wave:

$$\vec{E}(\vec{r}, t) = \vec{E}_0 \cos\left(\vec{k} \cdot \vec{r} - \omega t\right), \tag{2.3}$$

with the wave-vector $\vec{k}$ and angular frequency ω. In vacuum, the relation $\omega = ck$ holds as a result of Eqn. (2.2). The modulus of the wave-vector, called wave-number $k = \left|\vec{k}\right|$ is linked to the wavelength λ by $k = 2\pi/\lambda$.

[1] $\epsilon_0 = 8.854 \times 10^{-12}\,\mathrm{F\,m^{-1}}$, $\mu_0 = 1.257 \times 10^{-6}\,\mathrm{H\,m^{-1}}$ [118]
[2] The Laplace operator is defined by $\triangle := \nabla \cdot \nabla$.

In vacuum, the wave vector $\vec{k}$ is perpendicular to the electric field, and the direction of the electric field is called polarization vector $\vec{E}_0/|\vec{E}_0| = \hat{e}_\mathcal{P}$.
In this work, we make use of the scalar wave approximation, where we neglect the vectorial nature of the electric field.

$$V(\vec{r},t) = \psi_0 \cos\left(\vec{k}\cdot\vec{r} - \omega t\right), \tag{2.4}$$

is a solution of the scalar wave equation (also known as d'Alembert equation [14] for the case $f(\vec{r},t) \equiv 0$):

$$\left(\frac{1}{c^2}\frac{\partial^2}{\partial t^2} - \triangle\right) V(\vec{r},t) = f(\vec{r},t)\,, \tag{2.5}$$

that can be interpreted as one dimensional version (or projection) of Eqn. (2.2). However it is important to note that there are solutions of V, that if it is interpreted as one dimension of $\vec{E}$, the individual dimensions do no longer satisfy the same wave equation. One prominent example is the spherical wave solution

$$V(r,t) = \frac{\cos(kr - \omega t)}{kr}\,, \tag{2.6}$$

where[3] $r = \sqrt{x^2+y^2+z^2} = |\vec{r}|$. This spherical wave cannot be a solution of the vectorial wave equation (Eqn. (2.2)), since it is not possible to construct a 2-sphere (a topological sphere in the three dimensional space) with a non-vanishing continuous tangent vector field, for proof see the "hairy ball theorem" [87]. However, the spherical scalar wave is an extraordinarily useful concept where for example the Huygens–Fresnel [56] principle is based on, which we will discuss later in this chapter.

A commonly and very useful convention is to write the wave-solutions as complex exponential function. For example Eqn. (2.4) can be written as

$$V(t,\vec{r}) = V_0\,\mathfrak{Re}\left(e^{i(\vec{k}\cdot\vec{r}-\omega t)}\right) = \frac{1}{2}\left(e^{i(\vec{k}\cdot\vec{r}-\omega t)} + e^{i(-\vec{k}\cdot\vec{r}+\omega t)}\right). \tag{2.7}$$

Often[4], it is sufficient to only consider the *complex amplitude* [6] $\psi(t,\vec{r})$ from

$$V(t,\vec{r}) = \mathfrak{Re}\left(\psi(t,\vec{r})\right). \tag{2.8}$$

It should be emphasized, that ψ is a solution of Eqn. (2.5) itself. In the following, we will refer to ψ as *wave field*.

In this work, we are focusing on waves in the X-ray regime ($\omega > 1.5\times10^{18}\,\mathrm{s}^{-1}$) and thus have no experimental access to a temporal resolved amplitude. Therefore, we will usually consider only the time independent part $\psi(\vec{r})$ of the wave field from

$$\psi(t,\vec{r}) = \psi(\vec{r})e^{-i\omega t}\,. \tag{2.9}$$

This time independent part must satisfy the *Helmholtz equation* at each source-free point

$$\left(\triangle + k^2\right)\psi(\vec{r}) = 0\,. \tag{2.10}$$

[3] For the sake of readability, we choose the notation $a = |\vec{a}|$.
[4] In general in linear optics or when only the time average of a quadratic expression is required [6].

2.1.1 Free space propagation and Fourier optics

Here, we recapitulate on how to propagate an arbitrary wave field along the *optical axis* $\hat{e}_z$. We start with the plane wave solution of Eqn. (2.10), as given by

$$\psi_{\text{PW}}(x,y,z) = e^{i(k_x x + k_y y)} e^{iz\sqrt{k^2-k_x^2-k_y^2}}\,, \tag{2.11}$$

where the components along the optical axis and the perpendicular components have been separated, using the relation $k^2 = k_x^2 + k_y^2 + k_z^2$. The unpropagated wave than reads $\psi_{\text{PW}}(x,y,z=0) = e^{i(k_x x + k_y y)}$, which allows us to identify the Helmholtz propagation term as $e^{iz\sqrt{k^2-k_x^2-k_y^2}}$. Any unpropagated wave field can be expressed by its Fourier transform

$$\psi(x,y,z=0) = \frac{1}{2\pi}\iint_{-\infty}^{\infty} \tilde{\psi}(k_x,k_y,z=0) e^{i(k_x x + k_y y)}\, dk_x\, dk_y\,, \tag{2.12}$$

where $\tilde{\psi}(k_x,k_y,z=0)$ denotes the 2D Fourier transform of $\psi(x,y,z=0)$. This representation can be interpreted as the decomposition of $\psi(x,y,z=0)$ into plane wave fields [96]. This expression allows to propagate each of these plane waves along the optical axis:

$$\psi(x,y,z) = \frac{1}{2\pi}\iint_{-\infty}^{\infty} \tilde{\psi}(k_x,k_y,z=0) e^{iz\sqrt{k^2-k_x^2-k_y^2}} e^{i(k_x x + k_y y)}\, dk_x\, dk_y\,. \tag{2.13}$$

We can identify the *Helmholtz propagator* as[5]

$$P_{\text{H}}(x,y,z) = \frac{1}{2\pi}\iint_{-\infty}^{\infty} e^{iz\sqrt{k^2-k_x^2-k_y^2}} e^{i(k_x x + k_y y)}\, dk_x\, dk_y\,, \tag{2.14}$$

that can be used to propagate wave fields via convolution[6,7] of the propagator with the unpropagated wave field

$$\psi(x,y,z) = \psi(x,y,z=0) * P_{\text{H}}(x,y,z)\,. \tag{2.15}$$

In the next step, we assume that the wave field is paraxial, which means that the wave vector, at any point of the wave field, only slightly deviates from the direction of the optical axis $k_z^2 \gg k_x^2 + k_y^2$. That justifies a Taylor expansion within the propagator of Eqn. (2.14) in terms of k and cutting at linear order:

$$\sqrt{k^2 - k_x^2 - k_y^2} \approx k - (k_x^2 + k_y^2)/(2k)\,. \tag{2.16}$$

[5] A detailed derivation can be found in [96, 120].
[6] The convolution is defined as follows $(f * g)(x) = \int_{-\infty}^{\infty} f(x')g(x-x')\,dx'$.
[7] The Fourier-convolution theorem is used: $\mathfrak{F}\left[(f*g)(x)\right](k) = \mathfrak{F}\left[f(x)\right](k)\ \mathfrak{F}\left[g(x)\right](k)$.

Substituting Eqn. (2.16) into Eqn. (2.14) yields

$$\frac{1}{2\pi}\iint_{-\infty}^{\infty} e^{ikz} e^{-\frac{k_x^2+k_y^2}{2k}} e^{i(k_x x+k_y y)}\, dk_x\, dk_y\,, \tag{2.17}$$

where we are now able to execute the integrals and obtain the *Fresnel propagator* as

$$P_{\mathrm{F}}(x,y,z) = -\frac{ik}{2\pi z} e^{ikz} e^{i\frac{k}{2z}(x^2+y^2)}\,. \tag{2.18}$$

This propagator can be used in analogous fashion to the Helmholtz propagator (see Eqn. (2.15)) for propagating paraxial wave fields in free space (vacuum).

For the next step, we write the convolution with the Fresnel propagator explicitly as

$$\begin{aligned}\psi(x,y,z) &\approx -\frac{ik}{2\pi z} e^{ikz} \iint_{-\infty}^{\infty} \psi(x,y,z=0) e^{i\frac{k}{2z}\left((x-x')^2+(y-y')^2\right)}\, dx'\, dy' \\ &= -\frac{ik}{2\pi z} e^{ikz} e^{i\frac{k}{2z}(x^2+y^2)} \iint_{-\infty}^{\infty} \psi(x,y,z=0) e^{-i\frac{k}{z}(xx'+yy')} e^{i\frac{k}{2z}\left((x')^2+(y')^2\right)}\, dx'\, dy'.\end{aligned} \tag{2.19}$$

When we assume that the extent of the non-zero unpropagated wave field in the x, y plane is much smaller than the propagation distance times the wavelength ($kb^2/(2\pi z) \ll 1$, where b is the diameter of the unpropagated wave field with non-zero contributions), we call this the *far field approximation*. In this case, we can drop the $e^{i\frac{k}{2z}\left((x')^2+(y')^2\right)}$ term in Eqn. (2.19) and obtain the *Fraunhofer diffraction* [96] as

$$\psi(x,y,z) \approx -\frac{ike^{ikz}}{z} e^{\frac{ik}{2z}(x^2+y^2)}\, \tilde{\psi}\left(k_x = \frac{kx}{z}, k_y = \frac{ky}{z}, z=0\right)\,. \tag{2.20}$$

Since we are usually measuring the intensity $I = |\psi|^2$, the terms prior to the Fourier transformed unpropagated wave field ($\tilde{\psi}(k_x, k_y, z=0)$) can be neglected except the (constant) factor k/z. The fact that far field propagation of wave fields basically computes the Fourier transform physically, has lead to the development of the so called 'Fourier Optics' [40].
In this work, we will make use of this approximation ($\psi(x,y,z) \propto \tilde{\psi}(k_x, k_y, z=0)$) whenever we are dealing with two-dimensional wave fields (e.g. resulting from two dimensional emitter distributions).

2.1.2 Coherent diffraction

Here, we recapitulate the interaction of a plane wave field with point scatters (like atoms). Thereby, we keep the approximations of the scalar wave field, made in the previous section. Furthermore, we assume elastic scattering, which means, that the wave field maintains its wavelength during the scattering process. We modify the homogeneous Helmholtz equation of Eqn. (2.10) to the *inhomogeneous Helmholtz equation*[8]

$$\left(\triangle + k^2\right)\psi(\vec{r}) = k^2(1 - n^2(\vec{r}))\psi(\vec{r})\,, \tag{2.21}$$

where $n(\vec{r})$ denotes the refractive index, which is unity in vacuum. These kind of differential equations can be solved for arbitrary $n(\vec{r})$ with the so called Greens function $G(\vec{r})$ [43, 16] by convoluting the right hand side of Eqn. (2.21) with G:

$$\psi(\vec{r}) = \psi_0(\vec{r}) - \frac{k^2}{4\pi}\iiint_{-\infty}^{\infty}\left(1 - n^2(\vec{r}')\right)\psi(\vec{r}')G(\vec{r} - \vec{r}')\,d^3r'\,, \tag{2.22}$$

where $\psi_0(\vec{r})$ denotes the solution of the homogeneous (free) Helmholtz equation. In general, the Greens function is the impulse response function[9] ($(1 - n^2(\vec{r}))\psi(\vec{r}) = -4\pi\delta(\vec{r})$)

$$\begin{aligned}\left(\triangle + k^2\right)G(\vec{r}) &= -4\pi\delta(\vec{r}) \\ \Rightarrow\; G(\vec{r}) &= \frac{e^{\pm ikr}}{|\vec{r}|}\,,\end{aligned} \tag{2.23}$$

and in this special case the spherical wave. However, Eqn. (2.22) is still not easily solvable, since it contains a recursion of $\psi(\vec{r})$. This can be solved, in analogous fashion to *perturbation theory* [106] known from quantum mechanics, by iteratively substituting the ψ under the integral with the current guess, starting with ψ_0:

$$\begin{aligned}\psi(\vec{r}) = \psi_0(\vec{r}) &- \frac{k^2}{4\pi}\iiint_{-\infty}^{\infty}(1 - n^2(\vec{r}'))G(\vec{r} - \vec{r}')\psi_0(\vec{r}')\,d^3r' \\ &+ \frac{k^4}{(4\pi)^2}\iiint_{-\infty}^{\infty}\iiint_{-\infty}^{\infty}(1 - n^2(\vec{r}'))(1 - n^2(\vec{r}''))G(\vec{r} - \vec{r}')G(\vec{r}' - \vec{r}'')\psi_0(\vec{r}'')\,d^3r''\,d^3r' \\ &- \dots\,.\end{aligned} \tag{2.24}$$

When the scattering is weak ($1 - n^2 \ll 1$) we can cut off Eqn. (2.24) after the linear order in G. This is also known as 'first Born approximation' [5], and corresponds to the case that every photon can only be scattered once (the scattered waves do not interact with the scatterers, again). This single-scattering approximation is also known as 'kinematic theory' [24].

[8] The derivation is done in analogous fashion to Eqn. (2.10), however the macroscopic Maxwells equation are used instead of the microscopic ones [96].
[9] The factor (-4π) is introduced by convention.

Assuming the incident wave-field to be a plane wave $\psi_0(\vec{r}) = e^{i\vec{k}_0\cdot\vec{r}}$, and the Greens function given by Eqn. (2.23), we obtain

$$\psi(\vec{r}) = e^{i\vec{k}_0\cdot\vec{r}} - \frac{k^2}{4\pi^2}\iiint_{-\infty}^{\infty} \frac{e^{\pm ik|\vec{r}-\vec{r}'|}}{|\vec{r}-\vec{r}'|}(1-n^2(\vec{r}'))e^{i\vec{k}_0\cdot\vec{r}'}\,d^3r'\,. \tag{2.25}$$

In the next step, we apply the Fraunhofer (far field) approximation, following the same criteria as for the derivation of Eqn. (2.20), namely $n(\vec{r}') \neq 1$ only for $r' \ll r$ the scatterers are concentrated within a small volume in comparison to the distance, where the wave field is evaluated. This allows the following approximation:

$$\begin{aligned} |\vec{r}-\vec{r}'| &= \sqrt{x^2+y^2+z^2+x'^2+y'^2+z'^2-2(xx'+yy'+zz')} \\ &\approx \sqrt{r^2-2\vec{r}\cdot\vec{r}'} \approx r^2 - \vec{r}\cdot\vec{r}'\,, \end{aligned} \tag{2.26}$$

where the last approximation is done via a Taylor expansion around $r' = 0$ and truncation after linear order. Now we can write Eqn. (2.25) as

$$\psi(\vec{r}) = e^{i\vec{k}_0\cdot\vec{r}} + \frac{k^2 e^{ikr}}{4\pi r}\iiint_{-\infty}^{\infty}\left(n^2(\vec{r}')-1\right)e^{i\vec{q}\cdot\vec{r}'}\,d^3r'\,, \tag{2.27}$$

with $\vec{q} := k\vec{r}/|r| - \vec{k}_0$ denoting the difference between the out-going (scattered) and in-coming wave vector. We can see that the wave-field, scattered by a scatterer density $\rho(\vec{r}) \propto (n^2(\vec{r})-1)$ is actually proportional to the Fourier transform of the scatterer distribution

$$\psi_{\text{out}}(\vec{q}) \propto \iiint_{-\infty}^{\infty}\rho(\vec{r})e^{i\vec{q}\cdot\vec{r}}\,d^3r\,. \tag{2.28}$$

This relationship is denoting that the scattered wave describes the Fourier transform of the scatterer distribution. This was a breakthrough for X-ray crystallography, which now is a major tool to investigate structures of matter (e.g. proteins) [37]. We will refer to imaging techniques based on this principle of elastic scattering as *coherent diffraction imaging (CDI)*.

2.2 Coherence

Up to this point, we have assumed perfect spatial and temporal coherence. However, since this work is about *incoherent diffraction imaging*, it is necessary to define coherence and discuss how to quantify it. This is the purpose of this section.

Coherence refers to the ability of waves to interfere, which requires, that the phases ϕ of the wave-fields $\psi \propto \psi_0 e^{i\vec{k}\cdot\vec{r}+i\phi}$ is constant over space and time [51]. To quantify coherence, Albert A. Michelson [86] defined the visibility of interference fringes as

$$\nu := \frac{I_{\text{max}} - I_{\text{min}}}{I_{\text{max}} + I_{\text{min}}}\,, \tag{2.29}$$

where I_{max} and I_{min} are the maximal and minimal measured intensities of the fringes. Frederik Zernike later on defined [132] the *degree of coherence* and identified it as the visibility in special cases. However, Pieter H. van Cittert noted [125] that the degree of coherence is equal to his earlier introduced quantity 'Korrelation' (correlation) [126, 127]. Nevertheless, the term 'degree of coherence' has prevailed and therefore we will use it in the following. In order to quantitatively describe coherence, we will distinguish between temporal and spatial coherence and discuss each separately.

2.2.1 temporal coherence

The temporal coherence describes the stability of a wave field $\psi(t) \propto Ae^{i\omega t}$ in terms of frequency $\omega(t)$ and a amplitude $A(t)$ over time. To quantify the coherence, we make use of the so called *complex degree of coherence* [41], which is defined by

$$\gamma(\tau) := \frac{\langle \psi(t)\psi^*(t+\tau)\rangle_t}{\langle \psi(t)\psi^*(t)\rangle_t}\,, \tag{2.30}$$

where $\langle f(t)\rangle_t = T^{-1}\int_{-T/2}^{T/2} f(t)\,dt$ is the temporal average over a period T in the limit $T \to \infty$. As F. Zernike pointed out [132], the modulus of the complex degree of coherence does indeed quantify the expected visibility of interference fringes in a Michelson interferometer (see Fig. 2.1) as described in Eqn. (2.29) $|\gamma| = \nu$.

To define the coherence time as a more practical measure of the temporal coherence property, it is tempting to use the time τ, where the visibility falls to one over the Euler number $|\gamma(\tau_c)| = 1/e$. However this is not always possible, since $|\gamma(\tau)|$ is not necessarily a monotonic function (see for example Fig. 3.7b in Section 3.1.4). Leonard Mandel therefore proposed [78, 80] to define the coherence time as follows:

$$\tau_c := \int_{-\infty}^{\infty} |\gamma(\tau)|^2\,d\tau\,, \tag{2.31}$$

and this definition prevailed [41].

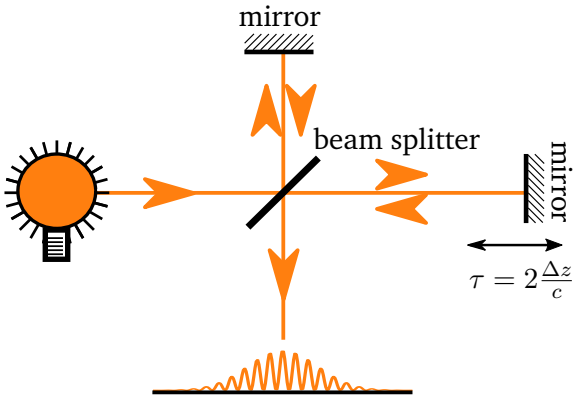

Fig. 2.1.: Simplified sketch of a Michelson interferometer. The light beam gets equally split and a time delay $\tau = 2\Delta z/c$ can be created by moving one of the mirrors Δz, from which the split beams gets reflected.

Second order temporal correlation of chaotic light

In addition to the degree of coherence, which is also known as the first-order temporal correlation, we can define the *second-order temporal correlation* as

$$g^{(2)}(\tau) = \frac{\langle \psi(t)\psi(t+\tau)\psi^*(t)\psi^*(t+\tau)\rangle_t}{\langle \psi(t)\psi^*(t)\rangle_t^2} = \frac{\langle I(t)I(t+\tau)\rangle_t}{\langle I(t)\rangle_t^2}\,, \tag{2.32}$$

which is also called the temporal intensity correlation function.
For chaotic light, such as light emitted by many independent emitters, the intensity correlation is related to the degree of coherence by the Siegert relation [113]

$$g^{(2)}(\tau) = 1 + |\gamma(\tau)|^2\,. \tag{2.33}$$

Providing a detailed derivation is refrained at this point. However, the approach is similar to that to be discussed in Section 2.5.1, where the second order of spatial correlation is derived in detail.
An important consequence of Eqn. (2.33) is the so-called *photon bunching* effect. Since $|\gamma(\tau = 0)|^2 = 1$ and $\lim_{\tau\to\infty}|\gamma(\tau)|^2 = 0$, for chaotic light, the probability to measure multiple photons in a short time is higher than implied by the average photon count. This effect was first described by Robert Hanbury Brown and Richard Q. Twiss [50, 47] and thus called *Hanbury Brown and Twiss (HBT) effect*.

Spectrum of the wave field

Any wave field, with changing frequency and or amplitude over time, can be expressed as superposition of monochromatic wave fields

$$\psi(t) = \int_{-\infty}^{\infty} F(\omega)e^{i\omega t}\,dt\,. \tag{2.34}$$

The complex weight function $F(\omega) \in \mathbb{C}$ hereby is apparently the Fourier transform of our wave field

$$F(\omega) = \frac{1}{2\pi} \int_{-\infty}^{\infty} \psi(t) e^{-i\omega t}\, dt\,. \tag{2.35}$$

The modulus square of this weight function $|F(\omega)|^2$ is called *power spectrum* and can be experimentally obtained by various spectroscopic methods [119].
For example, the power spectrum for a light source with a Lorentzian spectrum around the frequency ω_0 and a full width at half maximum (FWHM) of 2Γ reads

$$|F_{\mathrm{L}}(\Delta\omega)|^2 = \frac{1}{\Gamma^2 + (\omega - \omega_0)^2}\,. \tag{2.36}$$

This power spectrum corresponds to a monochromatic wave field with exponentially decaying envelope

$$\psi_{\mathrm{L}}(t) \propto e^{i\omega_0 t} e^{-\Gamma t} \Theta(t)\,, \tag{2.37}$$

where $\Theta(t) = 1\,\forall\, t > 0$, else 0 denotes the Heaviside step function. The wave field, along with the power spectrum and the degree of coherence is plotted in Fig. 2.2 for an exponential decaying envelope (Fig. 2.2a to 2.2c) and a Gaussian wave package (Fig. 2.2d to 2.2f). It should be noted, that for the first example τ_c actually represents the time, where the wave fields envelope falls to $1/e$, however, this is not the case for the Gaussian shaped pulse, where the time between the points, where the envelope is $1/e$ of its maximum is $\tau_{1/e} \approx 1.6\tau_c$.

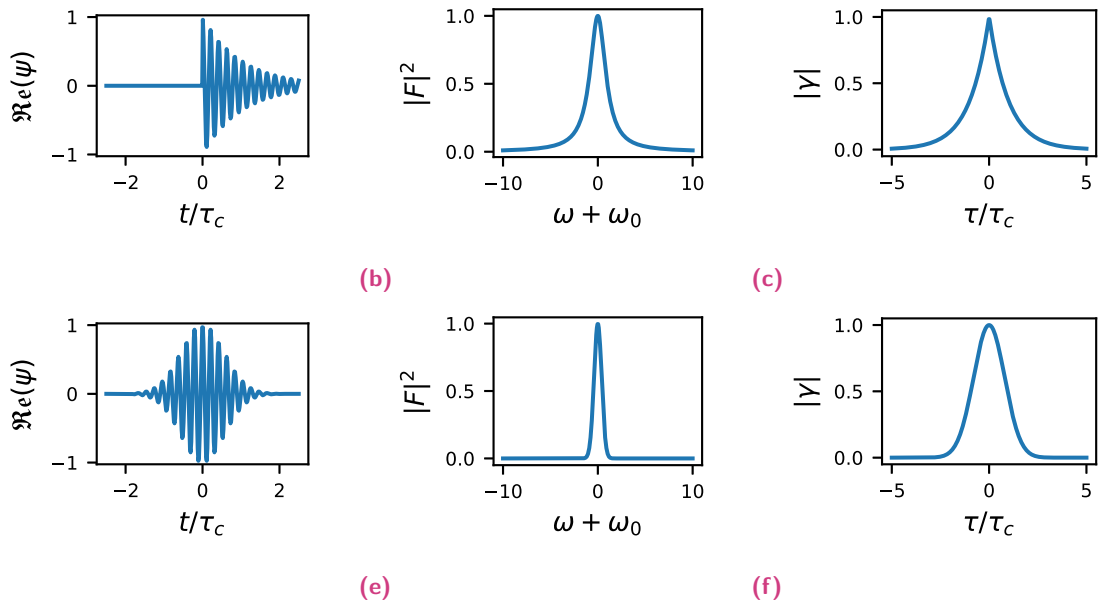

Fig. 2.2.: **(a** & **d)** Wave field, **(b** & **e)** power spectrum and **(c** & **f)** degree of coherence for exponential decaying envelope (a-c) and Gaussian wave packet (d-f). For these examples $\omega_0 = 30/\tau_c$ was chosen.

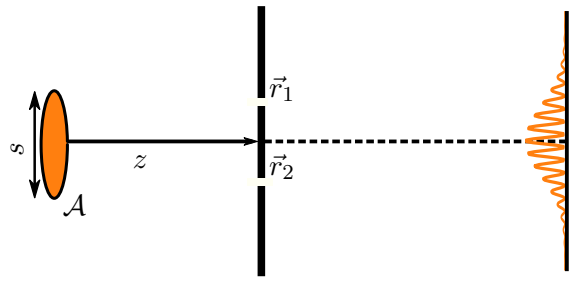

Fig. 2.3.: Simplified sketch of a Young interferometer to measure the visibility of interference fringes, generated by two pinholes at $\vec{r}_1$ and $\vec{r}_2$. In the illustrated case, the pinholes are in an opaque mask, located at a distance of z from a light source with the width s.

2.2.2 spatial coherence

Complementary to the temporal coherence, the spatial coherence describes the phase (and amplitude) relations between two spatially separated points in the wave field. To quantify the spatial coherence, we define the normalized cross-correlation function[10] in analogous fashion to Eqn. (2.30):

$$g^{(1)}(\vec{r}_1, \vec{r}_2) = \frac{\langle \psi(t, \vec{r}_1)\psi^*(t, \vec{r}_2)\rangle_t}{\sqrt{\langle \psi(t, \vec{r}_1)\psi^*(t, \vec{r}_1)\rangle_t \langle \psi(t, \vec{r}_2)\psi^*(t, \vec{r}_2)\rangle_t}}\,. \tag{2.38}$$

The visibility of the interference fringes, measured using a Young interferometer [131] (see Fig. 2.3), is then quantified by the modulus of the cross correlation $|g^{(1)}|$.

Van-Cittert Zernike theorem

We assume a two dimensional extended chaotic light source in the x, y-plane, with the area $\mathcal{A}$. Chaotic light source means, that the phase ϕ of the wave field emitted by the source is independent and random at any point within the source:

$$\psi(x, y, z = 0) \propto \begin{cases} \sqrt{I_0(x, y)}e^{i\phi(x,y)} \text{ for } x, y \in \mathcal{A}\,, \\ 0 \text{ else}\,. \end{cases} \tag{2.39}$$

We propagate ψ along the z-axis into the far field, using the Fraunhofer propagation (recall Eqn. (2.20)):

$$\psi(x, y, z) = \sqrt{I_0} \int_{\mathcal{A}} \sqrt{I_0(x', y')}e^{i\phi(x',y')} e^{i\frac{k}{z}xx'} e^{i\frac{k}{z}yy'}\, dx\, dy\,. \tag{2.40}$$

Substituting this into Eqn. (2.38), with $\vec{r}_1 = (x_1, y_1, z)^\top$ and $\vec{r}_2 = (x_2, y_2, z)^\top$, we obtain for the numerator of Eqn. (2.38) the following term:

$$g^{(1)}(\vec{r}_1, \vec{r}_2) \propto$$
$$I_0 \int_{\mathcal{A}}\int_{\mathcal{A}} \sqrt{I_0(x', y')}\sqrt{I_0(x'', y'')}e^{i\frac{k}{z}(x_1x' - x_2x'')} e^{i\frac{k}{z}(y_1y' - y_2y'')} \langle e^{i\phi(x',y')} e^{-i\phi(x'',y'')}\rangle\, dx'\, dy'\, dx''\, dy''\,. \tag{2.41}$$

[10] The normalized cross-correlation function is also called *complex degree of mutual coherence* [41].

Assuming completely uncorrelated and random phases, the average over the phase term $\langle e^{i(\phi(\vec{r}\,'_1)-\phi(\vec{r}\,'_2))}\rangle = \delta(\vec{r}\,'_1 - \vec{r}\,'_2)$ is zero for $\vec{r}\,'_1 \neq \vec{r}\,'_2$. With this, we can write the expression of $g^{(1)}$, for arbitrary intensity distributions $I_0(x, y, z = 0)$, as

$$g^{(1)}(\vec{r}_1, \vec{r}_2) = \frac{\int_{\mathcal{A}} I(x', y') e^{i\frac{k}{z}(x_1-x_2)x'} e^{i\frac{k}{z}(y_1-y_2)y'}\, dx'\, dy'}{\int_{\mathcal{A}} I(x', y')\, dx'\, dy'}\,. \tag{2.42}$$

This equation is known as the *Van Cittert-Zernike theorem* [11, 132]. It basically is a Fourier transform of the intensity distribution of the light source. As the light propagates along the z-axis, the phase fluctuation becomes smoother, and therefore the spatial coherence grows. An infinitesimal small point source, for example, always emits perfect spatially coherent light. The coherence area, defined by

$$A_\mathrm{c} = \iint_{-\infty}^{\infty} \left|g^{(1)}(\Delta x, \Delta y)\right|^2 d\Delta x\, d\Delta y\,, \tag{2.43}$$

is depending only on the difference coordinates $\Delta x, \Delta y$. For uniformly bright but spatially incoherent sources of area $\mathcal{A}_\mathrm{s}$, the coherence area is given by [41]

$$A_\mathrm{c} = \frac{(\lambda z)^2}{\mathcal{A}_\mathrm{s}}\,. \tag{2.44}$$

2.3 Photon statistics

To accurately describe photon statistics, classical wave theory falls short and quantum optics have to be utilized. Therefore, we will make use of the Dirac notation [17], without introducing it in detail.

2.3.1 Quantization of the electromagnetic field and Fock states

To quantize the electromagnetic field, we assume that the field is confined within a cubic volume $V = L^3$, with periodic boundary conditions. As result, only waves of frequencies such that an integer number of wavelengths fits into the volume $\omega_k = 2\pi ck/L$ are permitted. With this assumption, the electric field, from Eqn. (2.3), can be quantized [128, 107] and we obtain the electric field operator as

$$\begin{aligned}
&\hat{E}_k(\vec{r},t) = \sum_k \sum_{s=1}^{2} \vec{\epsilon}_{k,s} E_{0,k} \left(\hat{E}_k^{(+)}(\vec{r},t) + \hat{E}_k^{(-)}(\vec{r},t) \right) \text{ with} \\
&\hat{E}_k^{(+)}(\vec{r},t) = E_{0,k} e^{i(\vec{k}\cdot\vec{r}-\omega_k t)} \hat{a}_k \text{ and} \\
&\hat{E}_k^{(-)}(\vec{r},t) = E_{0,k} e^{i(-\vec{k}\cdot\vec{r}+\omega_k t)} \hat{a}_k^\dagger = \left(\hat{E}_k^{(+)} \right)^\dagger ,
\end{aligned} \tag{2.45}$$

where $E_{0,k} = \sqrt{\frac{\hbar\omega_k}{2\epsilon_0}}$. The polarization is determined by the unit polarization vectors $\vec{\epsilon}_{k,s}$, which in vacuum are orthogonal to the wave vector $\vec{\epsilon}_{k,s} \cdot \vec{k} = 0$, with $s = 1, 2$ denoting the two independent polarization states. However, for the following treatment we will, as before, neglect the polarization (scalar wave approximation). $\hat{a}_k$ and its adjoint $\hat{a}_k^\dagger$ represents the so called annihilation operator and creation operator, respectively. They are obeying the commutation[11] relation for bosons

$$\begin{aligned}
&[\hat{a}_k, \hat{a}_j^\dagger] = \delta_{k,j} \text{ and} \\
&[\hat{a}_k, \hat{a}_k] = [\hat{a}_k^\dagger, \hat{a}_k^\dagger] = 0 ,
\end{aligned} \tag{2.46}$$

where $\delta_{k,j} = (1 \text{ if } k = j, \text{ else } 0)$ denotes the *Kronecker delta*.
The Hamilton operator represents the total energy of the radiation field within the assumed cubic volume V and reads [128]

$$\hat{\mathcal{H}} = \sum_k \hbar\omega_k \left(\hat{a}_k^\dagger \hat{a}_k + \frac{1}{2} \right) . \tag{2.47}$$

We identify the number operator $\hat{n}_k = \hat{a}_k^\dagger \hat{a}_k$ with its eigenvalues n_k and eigenstates $|n_k\rangle$, where n_k yield the number of photons occupying the mode k and therefore $n_k \geq 0$ is integer. The eigenstates of $\hat{n}_k$ are also called *number* or *Fock states* and can be constructed as follows: starting with the *ground state* $|0_k\rangle$ we obtain the 'vacuum fluctuation energy' of mode k as

$$E_{k,0} = \langle 0_k | \hat{\mathcal{H}} | 0_k \rangle = \frac{1}{2} \hbar\omega_k . \tag{2.48}$$

[11] The commutator is defined by $[a, b] := ab - ba$.

The creation and annihilation operators are adding, or removing a photon from the number state, namely

$$\begin{aligned} \hat{a}_k^\dagger |n_k\rangle &= \sqrt{n_k+1}|n_k+1\rangle \text{ and} \\ \hat{a}_k |n_k\rangle &= \sqrt{n_k}|n_k-1\rangle \,. \end{aligned} \tag{2.49}$$

With these relations it is possible to create arbitrary number states by successive applying the creation operator to the ground state:

$$|n_k\rangle = \frac{(\hat{a}_k^\dagger)^{n_k}}{\sqrt{n_k!}}|0_k\rangle \,. \tag{2.50}$$

Properties of the Fock states are orthogonality $\langle n_k|m_k\rangle = \delta_{n,m}$ and completeness $\sum_{n_k=0}^{\infty} |n_k\rangle\langle n_k| = \hat{\mathbb{1}}$, and thus any state can be expressed in terms of Fock states.
In an experimental context, the number of photons at a detector is the observable. Assuming an arbitrary state $|\psi\rangle$, that is composed of Fock states, we obtain the probability of measuring exactly n photons in the mode k by

$$P(n) = |\langle n_k|\psi\rangle|^2 \,. \tag{2.51}$$

2.3.2 Coherent states

Glauber [38] introduced the *coherent states* as[12]

$$|\alpha\rangle = e^{-\frac{1}{2}|\alpha|^2} \sum_{n=0}^{\infty} \frac{\alpha^n}{\sqrt{n!}}|n\rangle \,. \tag{2.52}$$

These states are eigenstates of the annihilation $\alpha|\alpha\rangle = \hat{a}|\alpha\rangle$ and creation operator $\alpha^*|\alpha\rangle = \hat{a}^\dagger|\alpha\rangle$, and thus eigenstates of the electric field components $\hat{E}^{(+)}$ and $\hat{E}^{(-)}$. Therefore, the coherent states are a convenient form to describe classical wave fields.
Please note, that coherent states are not orthogonal. However, the scalar product $\langle\alpha|\alpha'\rangle$ decreases in absolute magnitude as α and α' recede from each other [38], with

$$|\langle\alpha|\alpha'\rangle|^2 = e^{-|\alpha-\alpha'|^2} \,. \tag{2.53}$$

Therefore, $|\alpha\rangle$ and $|\alpha'\rangle$ can be assume as approximately orthogonal, if $|\alpha-\alpha'| \gg 1$.
Although of their non orthogonal nature, coherent states are (over) complete[13]:

$$\frac{1}{\pi}\int \alpha|\alpha\rangle\langle\alpha|\, d^2\alpha = \hat{\mathbb{1}} \,. \tag{2.54}$$

[12] For sake of simplicity, we drop the mode index in the following: $|n_k\rangle = |n\rangle$.

[13] Proof: $\int |\alpha\rangle\langle\alpha|\, d^2\alpha = \sum_{n,m}^{\infty} \frac{1}{\sqrt{n!m!}}|n\rangle\langle m| \int \alpha e^{-|\alpha|^2}\alpha^n(\alpha^*)^m\, d^2\alpha$. The integral is solved using polar coordinates $\alpha = re^{i\varphi}$: $\int \alpha e^{-|\alpha|^2}\alpha^n(\alpha^*)^m\, d^2\alpha = \int_0^\infty re^{-r^2}r^{n+m}\, dr \int_0^{2\pi} e^{i(n-m)\varphi}\, d\varphi$. The latter integral evaluates to $2\pi\delta_{n,m}$. Now, the remaining integral evaluates to $2\pi\int_0^\infty re^{-r^2}r^{2n}\, dr = \pi n!$, and due to the $\delta_{n,m}$ term, we obtain $\sum_{n,m}^{\infty}\frac{1}{\sqrt{n!m!}}|n\rangle\langle m|\delta_{n,m} = \sum_n^\infty \frac{1}{n!}|n\rangle\langle n|$, so that $\frac{1}{\pi}\int|\alpha\rangle\langle\alpha|\, d^2\alpha = \sum_n^\infty |n\rangle\langle n|$ ■.

Since $\alpha \in \mathbb{C}$ is complex, the integral goes over the whole complex plane (therefore the integration over two dimensions $d^2\alpha$).
The expected mean photon count μ is calculated by projecting the number operator onto the coherent state

$$\mathbb{E}(n) = \langle\alpha|\hat{n}|\alpha\rangle = |\alpha|^2 = \mu\,, \tag{2.55}$$

and the variance

$$\mathrm{Var}_{\mathrm{coh}} = \langle\alpha|\hat{n}^2|\alpha\rangle - \langle\alpha|\hat{n}|\alpha\rangle^2 = |\alpha|^2 = \mu\,. \tag{2.56}$$

The probability distribution for measuring n photons is identified as the *Poisson distribution*[14]

$$|\langle n|\alpha\rangle|^2 = \frac{e^{-|\alpha|^2}|\alpha|^{2n}}{n!} = \frac{e^{-\mu}\mu^n}{n!} = P_{\mathrm{Poisson}}(n|\mu)\,. \tag{2.57}$$

2.3.3 Thermal states

States of *thermal light sources (TLS)*, also known as chaotic light, can be described by a number of similar but statistically independent sources of light. The *thermal states* can be expressed in terms of coherent states, as shown by Glauber in [38].
Since the coherent states are (over) complete, they can be used as a basis set for the density operator $\hat{\rho}$, as

$$\hat{\rho} = \int P(\alpha)|\alpha\rangle\langle\alpha|\, d^2\alpha\,. \tag{2.58}$$

Note that $P(\alpha)$ may only be interpreted as probability density if α is slowly varying and thus they can be interpreted as orthogonal (recall Eqn. (2.53)).
With this notation, the probability density can be written

$$P(\alpha) = \frac{1}{\pi\mu} e^{-\frac{|\alpha|^2}{\mu}}\,, \tag{2.59}$$

as derived in detail in [38].
In the following we will discuss this equation and derive it in a handwavy, yet graphical classical analogy. As discussed previously, the coherent states are eigenstates of the annihilation and creation operator and thus also eigenstates of the electric field operator. Therefore, in the first step, we construct a classical, chaotic wave field. Consider N independent classical emitters at a common location, each emitting a (scalar) wave $\psi \propto e^{i\phi_j}$ with random and independent phase $\phi_j = [0, 2\pi)$. This can be viewed as a random walk in the complex plane, as illustrated in Fig. 2.4. The resulting wave field then reads

$$\psi \propto \sum_{j=1}^{N} e^{i\phi_j}\,, \tag{2.60}$$

[14] The notation of probability distributions used in this work is described in Appendix A.1.

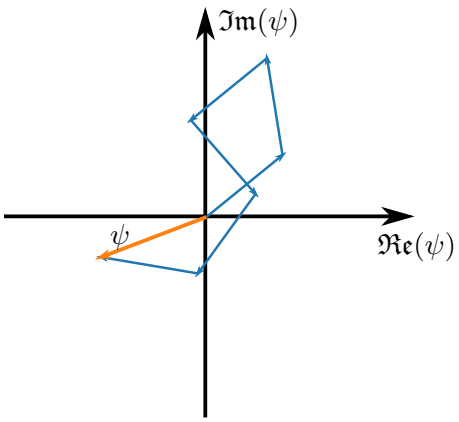

Fig. 2.4.: Sketch of a random walk in the complex plane, with equal step size but random orientation.

where in the limit of large N, $a = |\psi|^2$ follows an exponential distribution

$$P_{\text{Exp}}(a|\mu) = \frac{1}{\mu} e^{-\frac{a}{\mu}}\,, \tag{2.61}$$

with the expectation value $\mathbb{E}(a) = \mu \propto N$ and the variance $\text{Var}(a) = \mu^2$. With this classical illustration, we go back to the Gaussian density operator, that is obtained by inserting Eqn. (2.59) into Eqn. (2.58), as

$$\hat{\rho} = \frac{1}{\pi\mu} \int e^{-\frac{|\alpha|^2}{\mu}} |\alpha\rangle\langle\alpha|\, d^2\alpha\,. \tag{2.62}$$

Then, the probability distribution for measuring n photons reads

$$P_{\text{BE}}(n|\mu) = \langle n|\hat{\rho}|n\rangle = \frac{1}{1+\mu}\left(\frac{\mu}{1+\mu}\right)^n\,. \tag{2.63}$$

We identify this equation as the *Bose-Einstein distribution*, with the expectation value $\mathbb{E}(n) = \mu$ and the variance $\text{Var}(n) = \mu + \mu^2$. It should be emphasized that the Bose-Einstein distribution is also the compound distribution of the exponential and Poisson distribution[15].

2.3.4 Independent modes

The Fock single-mode states, introduced in Section 2.3.1, can be generalized to multi-mode states. Therefore, we assume, that the modes are orthogonal and therefore their creation and annihilation operators do not commute, recall Eqn. (2.46). Because of this, we can express the multi-mode Fock state as product of single mode states

$$|n_1, n_2, \ldots\rangle = \prod_j |n_j\rangle =: |\{n_j\}\rangle\,. \tag{2.64}$$

In the usual definition, modes are associated with their wave vector $\vec{k}$, as described in Eqn. (2.45). In this work, however, we are going to use the term 'mode' slightly differently. We will refer to (independent) 'modes' to express that they cannot interfere with each other.

[15] Proof: The compound probability distribution can be calculated by assuming a random exponential distributed value x', which is than used as expectation value to calculate the Poisson distributed value x. This is done for every possible x', for a given μ by integration: $\int_0^\infty \frac{1}{\mu} e^{-x'/\mu} \frac{x'^x}{x!} e^{-x'}\, dx' = P_{\text{BE}}(x|\mu)$. The result is indeed the Bose-Einstein distribution ■.

An example of two independent modes would be an orthogonal polarization. As a second example, to come back to the random walk in the complex plain of emitters emitting with random phases, imagine all emitters would be simultaneously assigned a new random phase after half of the emission time. This would also lead to two independent modes in that definition as the photons (wave field packages) before and after the phase shift are temporally separated and thus cannot interfere. The integrated intensity of such an M-mode random walk for a classical wave field of N-emitters can be expressed as

$$I(\vec{k}) = \psi(\vec{k})\psi^*(\vec{k}) \propto \frac{1}{M}\sum_{m=1}^{M}\left|\sum_{j=1}^{N} e^{i\phi_j}\right|^2 . \tag{2.65}$$

In the limit of large N, $a = |\psi|^2$ follows an *Erlang distribution*

$$P_{\text{Erlang}}(a|\mu, M) = \frac{a^{M-1}e^{-\frac{aM}{\mu}}}{\left(\frac{\mu}{M}\right)^M (M-1)!}\,\Big|\, M \in \mathbb{N}\,, \tag{2.66}$$

with the expectation value $\mathbb{E}(a) = \mu$ and the variance $\text{Var}(a) = \mu^2/M$.
The given definition of modes as orthogonal states typically restricts the number of modes to integers, although each mode may contain a varying number of photons. However, within this work, we relax this requirement and allow for non-integer (i.e., floating point) numbers of modes. Such non-integer values may represent an average over multiple measurements, with the actual number of modes fluctuating slightly, or they may reflect variations in the expected number of photons per mode [12]. In Appendix A.2.1, we discuss why this approximation is acceptable for the scope of this work.
The assumption of $M \in \mathbb{R}$, $M \geq 1$, will turn out to be very convenient for the discussions in Chapter 3 and Chapter 4. With this interpretation of modes, Eqn. (2.66) becomes a *Gamma distribution*

$$P_{\text{Gamma}}(a|\mu, M) = \frac{a^{M-1}e^{-\frac{aM}{\mu}}}{\left(\frac{\mu}{M}\right)^M \Gamma(M)}\,\Big|\, M \in \mathbb{R}\,, \tag{2.67}$$

where $\Gamma(x)$ denotes the gamma function. The expectation value $\mathbb{E}(a) = \mu$ and variance $\text{Var}(a) = \mu^2/M$, stays the same as for the Erlang distribution.
Following the same argumentation as given in Section 2.3.3, we can write a density operator for each mode separately. Following Eqn. (2.63), the photons of each mode then follows the Bose-Einstein distribution. Under the assumption that each mode has the same expectation value $\mu_0 = \mu/M$, the total expectation value stays $\mu = \sum_{m=1}^{M} \mu_0$. However, since the modes are independent, the variance is also given as the sum of the single mode variances and thus is modified to

$$\text{Var} = \sum_{m=1}^{M} \mu_0 + \mu_0^2 = \mu + \frac{1}{M}\mu^2 . \tag{2.68}$$

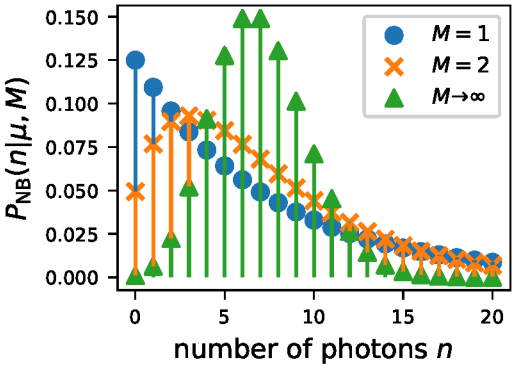

Fig. 2.5.: Probability for negative-binomial distributed values with $\mu = 7$ and $M = 1$ (Bose Einstein distributed), $M = 2$, and $M \to \infty$ (Poisson distributed).

The probability distribution, that gives exactly the expected expectation value (μ) and variance ($\mu + \mu^2/M$), can be obtained by calculating the compound distribution of the Gamma and the Poisson distribution

$$\int_0^\infty P_{\text{Gamma}}(a|\mu, M) P_{\text{Poisson}}(n|a)\, da = \frac{M^M \mu^n \Gamma(M+n)}{(M+\mu)^{M+n} n! \Gamma(M)} = P_{\text{NB}}(n|\mu, M)\,, \tag{2.69}$$

which we identify as the *negative binomial distribution* P_{NB}. For a derivation, using the combination of (integer) M Bose-Einstein distributions, see Appendix A.2. An example with $M = 2$, along side the Bose-Einstein limit ($M = 1$) and Poisson limit $M \to \infty$ is plotted in Fig. 2.5. It is important to mention that for non constant expected numbers of photons per mode, Eqn. (2.69) is only an approximation. To obtain the exact distribution it is required to know the expected number of photons per mode, a requirement that usually cannot be fulfilled.

2.4 X-ray fluorescence

In this work, the emitters we are dealing with are atoms that fluoresce in the X-ray spectrum. When an atom is ionized by high energy X-ray radiation, a vacancy is created in its inner shell, and a photon can be emitted. The ionization probability, given by the cross section of the photo-effect, is highest at the absorption edges for the corresponding electron shell (recall Fig. 1.1). A sketch of an atom with electron shells (here in the picture/approximation of Niels Bohr [4]) is shown in Fig. 2.6a.

After the vacancy is created, it is replaced by an electron from a higher shell. This can occur radiation-free by emitting an electron of an outer shell (known as the Auger-Meitner effect [85]), or 'radiatively' by emitting a fluorescence photon. We call the probability of the radiative decay *fluorescence yield* Y. There are different paths in which the decay can occur, resulting in different photon energies (lines), as shown in Fig. 2.6b. The line-ratio R_{line} indicates the probability of a certain decay line. The K-edge of iron, for example, is at an energy of $7.112\,\text{keV}$, a fluorescence yield of $Y = 0.343$ and the line-ratios by $R_{\text{K}_{\alpha,1}} = 0.581$, $R_{\text{K}_{\alpha,2}} = 0.297$ and $R_{\text{K}_\beta} = 0.122$ [105, 60]. The edge- and line-energies, besides line-ratios of selected light transition metals can be found in Tab. 2.1.

The power-spectrum of the X-ray fluorescence is well described as Lorentzian (recall Fig. 2.2c), as the K-fluorescence of the elements, we are discussing in this work, occurs on the femtosecond timescale and thus effects such as Doppler-broadening can be neglected [129]. For example, iron $K_{\alpha,1}$-fluorescence has a FWHM linewidth[16] of $\Gamma_l = 1.62\,\mathrm{eV}$ [67], which corresponds to a coherence time of $\tau_c = 2\hbar/\Gamma_l = 0.8\,\mathrm{fs}$. The line widths and coherence times of selected elements can be found in Tab. 2.2.

Other properties of fluorescence are: it is emitted isotropic, unpolarized, and chaotic which means there is no phase relation between the emitted photons from two independent emitters (spatial incoherence).

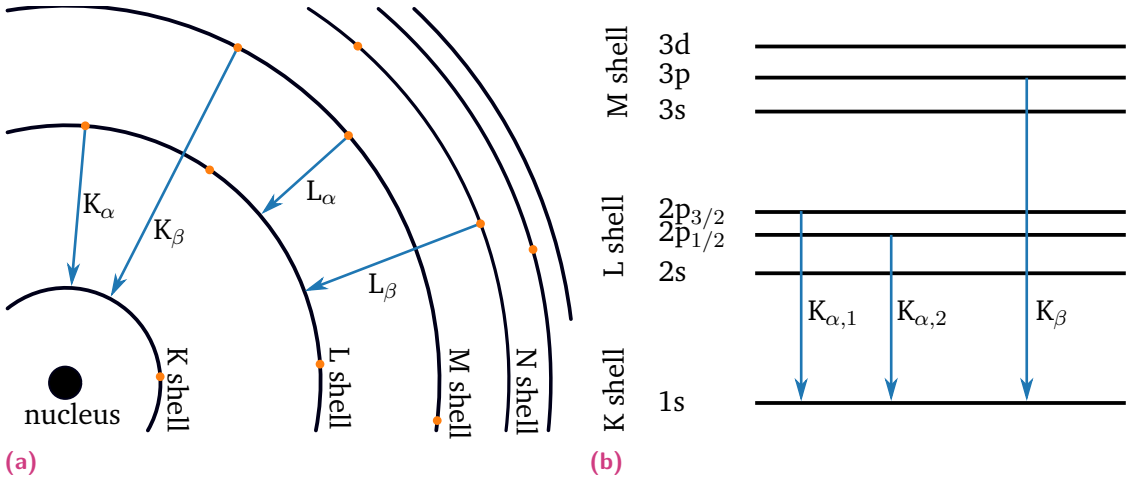

Fig. 2.6.: **(a)** Rutherford-Bohr atom model sketch with some indicated K and L transitions. **(b)** Atomic levels, with indicated $K_{\alpha,1}$, $K_{\alpha,2}$ and K_β transitions.

Element (Z)	K-edge (keV)	$K_{\alpha,1}$ (keV)	$R_{K_{\alpha,1}}$	$K_{\alpha,2}$ (keV)	$R_{K_{\alpha,2}}$	K_β (keV)	R_{K_β}
Sc (21)	4.4928	4.0906	0.586	4.0861	0.296	4.461	0.118
Ti (22)	4.9664	4.5109	0.584	4.5049	0.296	4.932	0.119
V (23)	5.4651	4.9522	0.583	4.9446	0.296	5.427	0.12
Cr (24)	5.9892	5.4147	0.585	5.4055	0.298	5.947	0.118
Mn (25)	6.539	5.8987	0.582	5.8876	0.297	6.49	0.122
Fe (26)	7.112	6.4039	0.581	6.3909	0.297	7.058	0.122
Co (27)	7.7089	6.9303	0.581	6.9153	0.297	7.649	0.122
Ni (28)	8.3328	7.4781	0.58	7.4609	0.297	8.265	0.122
Cu (29)	8.9789	8.0478	0.581	8.0279	0.298	8.905	0.121
Zn (30)	9.6586	8.6389	0.579	8.6158	0.298	9.572	0.124

Tab. 2.1.: Energy of K-edge and K-fluorescence for selected light transition metals, and line-ratio, taken from [105]. Note, that usually the element with $Z-1$ can be used to filter K_β form the element Z. However, this is not always the case, see Ti and Sc.

[16] Γ_l is the FWHM of the power-spectrum usually in units of electron volts. It should not be confused with the Γ of Eqn. (2.36) which is the decay constant of the wave field, given in s^{-1}. They obey the relation $\Gamma = \Gamma_l/(2\hbar)$.

Element (Z)	Fluorescence-yield Y	$K_{\alpha,1}$-line width FWHM(eV)	$\tau_c(K_{\alpha,1})$ (fs)	$K_{\alpha,2}$-line width FWHM(eV)	$\tau_c(K_{\alpha,2})$ (fs)
Sc (21)	0.196	1.05	1.25	1.06	1.24
Ti (22)	0.226	1.16	1.13	1.18	1.12
V (23)	0.256	1.26	1.04	1.28	1.03
Cr (24)	0.289	1.35	0.98	1.37	0.96
Mn (25)	0.321	1.48	0.89	1.5	0.88
Fe (26)	0.355	1.61	0.82	1.62	0.81
Co (27)	0.388	1.76	0.75	1.76	0.75
Ni (28)	0.421	1.94	0.68	1.96	0.67
Cu (29)	0.454	2.11	0.62	2.17	0.61
Zn (30)	0.486	2.32	0.57	2.39	0.55

Tab. 2.2.: Fluorescence yield and fluorescence line widths with emission coherence time for selected light transition metals, taken from [105, 67].

2.5 Photon-photon correlation imaging / incoherent diffraction imaging (IDI)

Section 2.1.2 covered the basics of coherent diffraction, which relies on a fixed relationship between the incoming and scattered (diffracted) wave field. However, here we assume that each scatterer applies a random phase shift instead, and thus, there is no determined phase relationship at all.

To distinguish this type of incoherent scattering from coherent diffraction, we will refer to the scatterers as "emitters." Although this work primarily focuses on X-ray fluorescence, many of the concepts we discuss apply to other sources of incoherent emissions, such as band-filtered (monochromatic) thermal light sources (e.g., astronomical objects such as stars). Therefore, the ideas and concepts presented in this work may have broader applications beyond X-ray fluorescence.

2.5.1 IDI in the classical limit

We start with the classical approximation. There, the process of incoherent emission can be described by assigning an independent and random phase factor $e^{i\phi}$, with $\phi = [0, 2\pi)$ to each emitter. The scalar wave field, in the far field approximation, for N-emitters can then be expressed as

$$\psi(\vec{k}) \propto \sum_{j=1}^{N} e^{i\left(\vec{k}\cdot\vec{r}_j+\phi_j\right)} . \tag{2.70}$$

This equation is the incoherent analogue to Eqn. (2.28). For simplicity, the emitter density $\rho(\vec{r})$ is changed to a discrete point like emitters collection, and also, the $1/|\vec{r}|$ decay is neglected.

This implicitly assumes that the detection for different $\vec{k}$ happens in the far-field and at equal distances to the emitter distribution. Also, the far-field approximation assumes that the extent of the emitter distribution is small compared to the distance to the detector.
For each emission process, we assume a new random and uncorrelated set of phases (no spatial coherence at the emitting object). Therefore, the measured intensity is integrated over time, and thus over many phase realizations, $\langle I(\vec{k})\rangle = \langle \psi(\vec{k})\psi^*(\vec{k})\rangle_{\{\phi\}}$ turns out to be flat

$$\langle I(\vec{k})\rangle \propto \sum_{j=1}^{N}\sum_{l=1}^{N} e^{i\vec{k}\cdot(\vec{r}_j-\vec{r}_l)}\langle e^{i(\phi_j-\phi_l)}\rangle_{\{\phi\}} = N\,, \tag{2.71}$$

since the phase-factor $\langle e^{i(\phi_j-\phi_l)}\rangle_{\{\phi_j,\phi_l\}} = \delta_{j,l}$ is only unequal zero for $j = l$. No structural information on the emitter distribution can be obtained from this.

However, when we correlate the integrated intensities of two different wave vectors ($\vec{k}_1$ and $\vec{k}_2$), measured within sufficiently short time spans such that the phases can be assumed constant (within the coherence time) and average many of these correlations, we can indeed obtain structural information. Therefore, we write the intensity-intensity correlation as a four-fold sum over the participating wave fields emitted by the individual emitters:

$$\begin{aligned}\langle I(\vec{k}_1), I(\vec{k}_2)\rangle &\propto \langle \psi(\vec{k}_1)\psi^*(\vec{k}_1)\psi(\vec{k}_2)\psi^*(\vec{k}_2)\rangle_{\{\phi\}} \\ &= \sum_{j=1}^{N}\sum_{j'=1}^{N}\sum_{l=1}^{N}\sum_{l'=1}^{N} e^{i\vec{k}_1\cdot\left(\vec{r}_j-\vec{r}_{j'}\right)} e^{i\vec{k}_2\cdot(\vec{r}_l-\vec{r}_{l'})}\langle e^{i\left(\phi_j-\phi_{j'}+\phi_l-\phi_{l'}\right)}\rangle_{\{\phi\}}\,.\end{aligned} \tag{2.72}$$

The phase term $\langle e^{i\left(\phi_j-\phi_{j'}+\phi_l-\phi_{l'}\right)}\rangle_{\{\phi\}}$ is unequal zero only when the exponent becomes zero. That occurs in two different cases:

Case 1: $j = j'$ and $l = l'$:
Then Eqn. (2.72) reduces to

$$\sum_{j=1}^{N}\sum_{l=1}^{N} e^{i\vec{k}_1\cdot(\vec{r}_j-\vec{r}_j)} e^{i\vec{k}_2\cdot(\vec{r}_l-\vec{r}_l)} = N^2\,, \tag{2.73}$$

which is a constant distribution without any structural information. We will refer to this as *offset*.

Case 2: $j = l'$ and $l = j'$:
Here we obtain

$$\sum_{j=1}^{N}\sum_{l=1}^{N} e^{i\vec{k}_1\cdot(\vec{r}_j-\vec{r}_l)} e^{i\vec{k}_2\cdot(\vec{r}_l-\vec{r}_j)} = \sum_{j=1}^{N}\sum_{l=1}^{N} e^{i\left(\vec{k}_1-\vec{k}_2\right)\cdot(\vec{r}_j-\vec{r}_l)} = \left|\sum_{j=1}^{N} e^{i\vec{q}\cdot\vec{r}_j}\right|^2\,, \tag{2.74}$$

with the substitution $\vec{q} = \vec{k}_1 - \vec{k}_2$ in the last step. If we assume an emitter density $\rho(\vec{r})$ instead of discrete emitters, we can write Eqn. (2.74) as integral

$$\left|\int \rho(\vec{r}) e^{i\vec{q}\cdot\vec{r}}\, d^3r\right|^2 = \left|\mathfrak{F}\left[\rho(\vec{r})\right](\vec{q})\right|^2\,. \tag{2.75}$$

We identify this as the modulus Fourier transform of the emitter density $|\mathfrak{F}\left[\rho(\vec{r})\right](\vec{q})|$. We will refer to the contribution of this second case as *usable signal*.
By normalization and combining both cases, we obtain

$$\frac{\langle I(\vec{k})I(\vec{k}+\vec{q})\rangle_{\vec{k},\{\phi\}}}{\langle I(\vec{k})\rangle^2_{\vec{k},\{\phi\}}} = 1 + \frac{|\mathfrak{F}\left[\rho(\vec{r})\right](\vec{q})|^2}{|\mathfrak{F}\left[\rho(\vec{r})\right](0)|^2}\,. \tag{2.76}$$

In this notation, the averaging is performed over the random phases, but also all available (measured) $\vec{k}_1$ and $\vec{k}_2$ with $\vec{k}_1 - \vec{k}_2 = \vec{q}$. Thus, the average over the $\vec{k}$ vectors represents a spatial auto-correlation. In the following, we will use the notation

$$\begin{aligned} G^{(1)}(\vec{q}) &= \langle \psi(\vec{k})\psi^*(\vec{k}+\vec{q})\rangle = \mathfrak{F}\left[\rho(\vec{r})\right](\vec{q})\,, \\ g^{(1)}(\vec{q}) &= \frac{\mathfrak{F}\left[\rho(\vec{r})\right](\vec{q})}{\mathfrak{F}\left[\rho(\vec{r})\right](0)}\,, \end{aligned} \tag{2.77}$$

and

$$\begin{aligned} G^{(2)}(\vec{q}) &= \langle I(\vec{k})I(\vec{k}+\vec{q})\rangle\,, \\ g^{(2)}(\vec{q}) &= \frac{\langle I(\vec{k})I(\vec{k}+\vec{q})\rangle}{\langle I(\vec{k})\rangle^2}\,. \end{aligned} \tag{2.78}$$

$g^{(1)}$ is the normalized auto-correlation of the wave field and $g^{(2)}$ the second order auto-correlation (intensity auto-correlation).
Now, we can convert Eqn. (2.76) into the following form

$$g^{(2)}(\vec{q}) = 1 + \beta\left|g^{(1)}(\vec{q})\right|^2\,, \tag{2.79}$$

the (modified) so-called Siegert relation [113]. The modification consists of the visibility factor β, which scales the usable signal. The derivation of Eqn. (2.76) assumes that the phases are not changing during the measurement of $I(\vec{k})$ and that all wave fields are able to interfere. This is not necessarily the case since the polarization can be different, and/or the measurement time might be longer than the coherence time, which leads to changing phases during the measurement. The visibility factor is used to parameterize all factors that prevent wave fields from interfering, and thus, is the reciprocate number of modes $\beta = 1/M$ introduced in Section 2.3.4. Since we only expect a positive number of modes with $M \geq 1$, the visibility factor ranges from $0 \leq \beta \leq 1$. An in-depth analysis of how the visibility factor can be calculated and measured is discussed and demonstrated in Chapter 3.

2.5.2 Non-classical light sources

In the case of very few (single photon) emitters, the classical derivation of the previous section faces some limits. Therefore, we will discuss the second-order correlation from a quantum optic point of view. To do so, we use the electric field operators defined in Eqn. (2.45) and obtain the correlation function (in an analogous fashion to Eqn. (2.72))

$$G^{(2)}(\vec{k}_1,\vec{k}_2) = \left\langle \hat{E}^{(-)}(\vec{k}_1)\hat{E}^{(-)}(\vec{k}_2)\hat{E}^{(+)}(\vec{k}_1)\hat{E}^{(+)}(\vec{k}_2)\right\rangle . \tag{2.80}$$

We will only discuss the single mode case here, and thus the mode subscript was dropped $\hat{E}_k^{(\pm)} \rightarrow \hat{E}^{(\pm)}$. The electric field operator (in the far field) for a field generated by N equally strong emitters is given by

$$\left(\hat{E}^{(+)}\right)^\dagger = \hat{E}^{(-)}(\vec{k}) \propto \sum_{j=1}^{N} e^{i\left(-\vec{k}\cdot\vec{r}_j+\phi_j\right)}\hat{a}_j^\dagger . \tag{2.81}$$

We can write $G^{(2)}$ as a four-fold sum again (similar to Eqn. (2.72))

$$G^{(2)}(\vec{k}_1,\vec{k}_2) = \sum_{j=1}^{N}\sum_{j'=1}^{N}\sum_{l=1}^{N}\sum_{l'=1}^{N} e^{i\vec{k}_1\cdot(\vec{r}_j-\vec{r}_{j'})}e^{i\vec{k}_2\cdot(\vec{r}_l-\vec{r}_{l'})}\langle e^{i\left(\phi_j-\phi_{j'}+\phi_l-\phi_{l'}\right)}\hat{a}_j^\dagger\hat{a}_l^\dagger\hat{a}_{j'}\hat{a}_{l'}\rangle . \tag{2.82}$$

As before, we distinguish the cases of j, j', l, l' combinations, where the phase term is unequal zero:

case 1: $j = j'$ and $l = l'$ but $j \neq l$:
here we obtain $\langle\hat{a}_j^\dagger\hat{a}_l^\dagger\hat{a}_j\hat{a}_l\rangle = \langle\hat{n}\rangle^2$, since $\hat{a}_l^\dagger$ and $\hat{a}_j$ commutate ($[\hat{a}_l^\dagger,\hat{a}_j] = 0$ for $l \neq j$). So the remaining term becomes the constant *offset*:

$$\sum_{j=1}^{N}\sum_{l=1}^{N}(1-\delta_{j,l})e^{i\vec{k}_1\cdot(\vec{r}_j-\vec{r}_j)}e^{i\vec{k}_2\cdot(\vec{r}_l-\vec{r}_l)} = N^2 - N . \tag{2.83}$$

case 2: $j = l'$ and $j' = l$ but $j \neq j'$:
again, we obtain $\langle\hat{a}_j^\dagger\hat{a}_l^\dagger\hat{a}_l\hat{a}_j\rangle = \langle\hat{n}\rangle^2$ and the *usable signal* term as

$$\sum_{j=1}^{N}\sum_{l=1}^{N}(1-\delta_{j,l})e^{i\vec{k}_1\cdot(\vec{r}_j-\vec{r}_l)}e^{i\vec{k}_2\cdot(\vec{r}_l-\vec{r}_j)} = \left|\sum_{j=1}^{N} e^{i\vec{q}\cdot\vec{r}_j}\right|^2 - N = \left|G^{(1)}(\vec{q})\right|^2 - N , \tag{2.84}$$

with $\vec{q} = \vec{k}_1 - \vec{k}_2$

case 3: $j = j' = l = l'$:
here we obtain the operator term

$$\langle\hat{a}^\dagger\hat{a}^\dagger\hat{a}\hat{a}\rangle = \langle\hat{a}^\dagger(\hat{a}\hat{a}^\dagger + [\hat{a}^\dagger,\hat{a}])\hat{a}\rangle = \langle\hat{n}^2\rangle - \langle\hat{n}\rangle , \tag{2.85}$$

where the commutator relation of Eqn. (2.46) was used ($[\hat{a}^\dagger, \hat{a}] = -1$). The remaining term becomes N.

Combining all three cases, we obtain the non-normalized form of the intensity (photon-photon) correlation as

$$G^{(2)}(\vec{q}) = N^2\langle\hat{n}\rangle^2 - 2N\langle\hat{n}\rangle^2 + N\left(\langle\hat{n}^2\rangle - \langle\hat{n}\rangle\right) + \left|G^{(1)}(\vec{q})\right|^2 . \tag{2.86}$$

The normalized form is obtained by dividing through $(N^2\langle\hat{n}\rangle^2)$, as

$$g^{(2)}(\vec{q}) = 1 + \frac{\langle\hat{n}^2\rangle - \langle\hat{n}\rangle}{N\langle\hat{n}\rangle^2} - \frac{2}{N} + \left|g^{(1)}(\vec{q})\right|^2 . \tag{2.87}$$

In the case of *single photon emitters*, where only the Fock state $|1\rangle$ is present, the squared number operator yields $\langle 1|\hat{n}^2|1\rangle = 1$. Therefore, we obtain the single photon emitter $g^{(2)}$ function as

$$g^{(2)}_{\mathrm{SPE}}(\vec{q}) = 1 - \frac{2}{N} + \left|g^{(1)}(\vec{q})\right|^2 . \tag{2.88}$$

In the case of thermal light sources, however, we obtain[17], by utilizing the Bose-Einstein distribution of Eqn. (2.63), $\langle\hat{n}^2\rangle = N + 2N^2$ with $\langle\hat{n}\rangle = N$, the normalized $g^{(2)}$ as

$$g^{(2)}_{\mathrm{TLS}}(\vec{q}) = 1 + \left|g^{(1)}(\vec{q})\right|^2 , \tag{2.89}$$

which equates to the classical term derived in Section 2.5.1.
This work mainly discusses X-ray fluorescence, and a fluorescing atom can be considered as a single photon emitter. However, we also focus on objects with many emitters ($N \gg 1$), and in this limit, the photon statistics become irrelevant for the $g^{(2)}$-signal. Therefore, we will use the classically deviated $g^{(2)}$ of Eqn. (2.79) for all further discussions.

2.5.3 Properties of incoherent diffraction imaging

Here, we discuss some properties of IDI and the main differences from CDI.
As discussed in Section 2.1.2, scatterers, in a CDI context, scatter photons elastically from an incoming beam. The signal $I(\vec{q}) \propto |\mathfrak{F}\left[\rho(\vec{r})\right](\vec{q})|^2$ is determined by photon counts measured at detector positions that correspond to $\vec{k}_{\mathrm{out}}$ and thus to $\vec{q}$ values with $\vec{q} = \vec{k}_{\mathrm{out}} - \vec{k}_{\mathrm{in}}$, as illustrated in Fig. 2.7a. In IDI, however, the $\vec{q}$ value is determined by the difference of two (freely selectable) positions $\vec{q} = \vec{k}_1 - \vec{k}_2$, as illustrated in Fig. 2.7b. One consequence is that IDI can have twice the resolution for the same detector geometry as CDI. Furthermore, a single CDI measurement gives only entries on a (two-dimensional) surface (for crystals known as the *Ewald sphere* [27]); therefore, the sample must be rotated to obtain a complete image. IDI measurements, however, give three-dimensional information from a single sample orientation [13].

[17] In this case, strict proof is not provided, but the interested reader is recommended to review the work of Anton Classen [12].

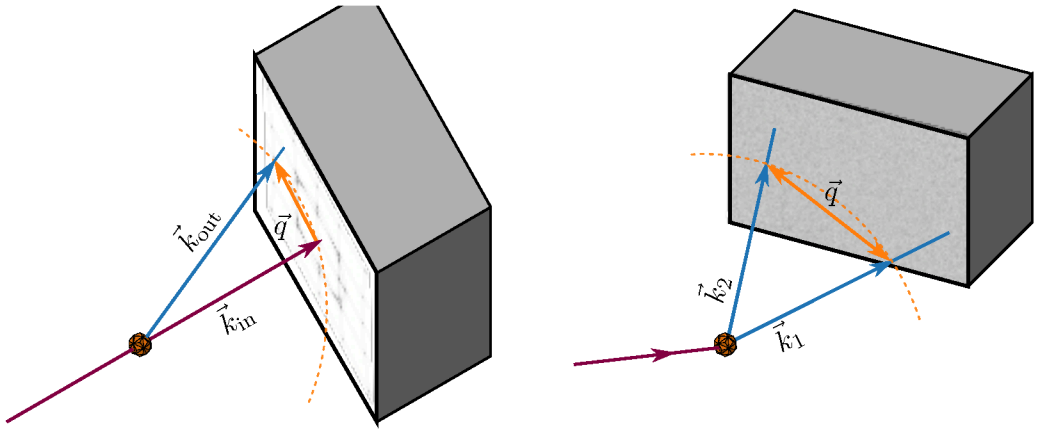

(a) (b)

Fig. 2.7.: **(a)**Sketch of a CDI experiment setup. The position at the detector determines the $\vec{q}$ value. **(b)** sketch of an possible IDI experiment setup. Here, the distance between two pixels determines the $\vec{q}$ value.

This is illustrated in Fig. 2.8, displaying a simulated[18] $g^{(2)}$ signal of the iron atoms in a $10\times10\times10$ unit cells 1FDN ferredoxin [22] crystal emitting $K_{\alpha,1}$ fluorescence. The shown signal is obtained using only one crystal orientation and a fixed $35\,\text{mm}\times35\,\text{mm}$-sized detector placed at a distance of $25\,\text{mm}$ from the interaction point.

Elastic scattering of X-ray photons on weakly bound electrons (often denoted as 'free electrons') is well approximated by the Thomson scattering [117, 59] with the differential cross section for polarized photons, given by

$$\frac{\mathrm{d}\sigma_{\mathrm{T}}}{\mathrm{d}\Omega} = r_{\mathrm{e}}\left(1-\cos^2(\phi)\,\sin^2(\theta)\right)\,, \tag{2.90}$$

where r_{e} denotes the classical electron radius[19], ϕ the angle between the polarization vector and scattering plane, and θ the scattering angle. For example, beams of polarized X-rays are given when X-rays are generated by an electron beam passing through a bending magnet or insertion devices such as undulators [130], which is the case at synchrotrons and XFELs. The consequence for CDI is that scattering at angles of $90°$ and parallel to the polarization vector is suppressed. Fluorescence, on the other hand, is isotropic and unpolarized. Therefore IDI is insensitive to this effect. The experiment, which we will discuss in Chapter 3, used the suppression of elastic scattering by polarization at $90°$ to eliminate 'coherent background' [122].

While CDI is imaging the electron density, IDI is based on fluorescence and, therefore, sensitive to certain elements that can be chosen by the energy of the photons in the excitation beam, as recently suggested by Phay J. Ho et al. [53]. IDI could, for example, be used in addition to CDI to track certain elements.

[18] Details about the simulation can be found in Appendix A.4.1
[19] $r_{\mathrm{e}} \approx 2.8179\times10^{-15}\,\mathrm{m}$ [118].

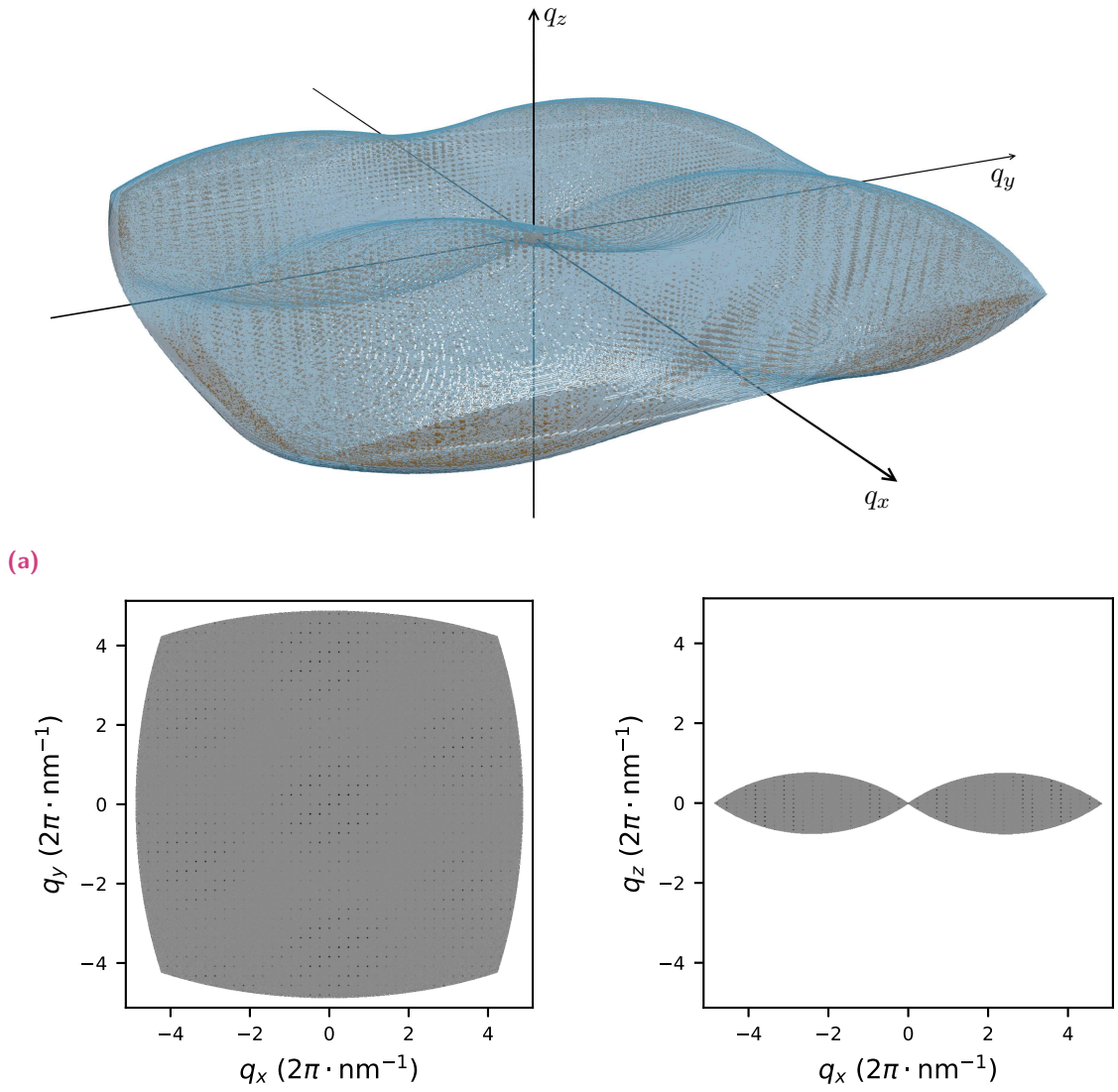

Fig. 2.8.: Illustration of the 3D information gained from single orientation IDI measurements. The Detector consists of 350×350 pixels with a pixel size of $100\,\mu\mathrm{m} \times 100\,\mu\mathrm{m}$, placed at a distance of $25\,\mathrm{mm}$ from the interaction point. The simulated sample is the distribution of iron atoms in a 1FDN ferredoxin crystal emitting $\mathrm{K}_{\alpha,1}$ fluorescence. **(a)** Render of the covered $g^{(2)}$ volume with the containing Bragg peaks (diameter of spheres is proportional to the signal strength). **(b)** Cut through the $q_x - q_y$ plane at $q_z = 0$. **(c)** Cut through the $q_x - q_z$ plane at $q_y = 0$.

3 Visibility factor and speckle contrast measurements

This chapter discusses the visibility factor β, which modulates (reduces) the usable signal part of $g^{(2)} = 1 + \beta|g^{(1)}|^2$. The visibility is decreased when photons cannot interfere, or there is no perfect temporal coherence during the measurement process. We, therefore, also use the term *modes*, where the photons in one mode are mutually coherent (giving rise to interference), similar to the mode term introduced in Section 2.3.4. The number of independent modes is reciprocal to the visibility factor

$$\beta = \frac{1}{M} \,. \tag{3.91}$$

Simulated speckle patterns with different visibility factors are shown in Fig. 3.1, with Fig. 3.1a to 3.1c in a high photon count ($\mu = 100$) and Fig. 3.1d to 3.1f in a low photon count ($\mu = 0.01$) regime. While the effect of the visibility factor is quite apparent in the high photon count regime, it becomes harder to see it directly in the limit of sparse signals. In this chapter, we will focus on how to retrieve the visibility factor in the very low photon count regime.

3.1 Visibility factor calculation

So far, we have assumed that the phases of the emitter do not change during the measurement. This can be assumed when the measurement time is significantly shorter than the coherence time. This work focuses on X-ray fluorescence of light transition metals, where the coherence time is in the order of, or less than one femtosecond. There are X-ray detectors with a temporal resolution of around hundreds of picoseconds [73], which would be at least five orders of magnitude longer than the coherence time of X-ray fluorescence. However, instead of fast gating, we can utilize short pulses for exciting the fluorescence.

As mentioned previously, besides the gating time or pulse duration, there are more factors reducing the visibility, which we will address in the following individually. The final visibility factor can then be calculated as the product of all partial visibility factors:

$$\beta = \beta_\mathrm{p}\, \beta_c\, \beta_\mathrm{pol}\, \beta_\mathrm{lines}\, \beta_\mathrm{SPS}\, \beta_? \,. \tag{3.92}$$

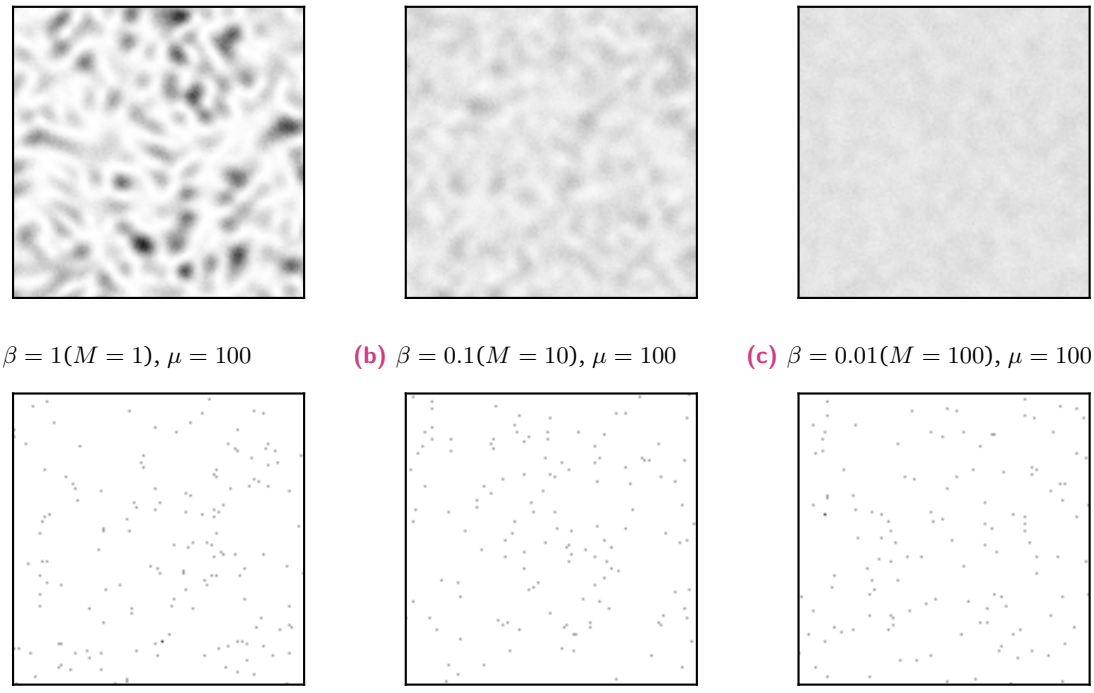

(a) $\beta = 1 (M = 1)$, $\mu = 100$ (b) $\beta = 0.1 (M = 10)$, $\mu = 100$ (c) $\beta = 0.01 (M = 100)$, $\mu = 100$

(d) $\beta = 1 (M = 1)$, $\mu = 0.01$ (e) $\beta = 0.1 (M = 10)$, $\mu = 0.01$ (f) $\beta = 0.01 (M = 100)$, $\mu = 0.01$

Fig. 3.1.: Illustration of speckle patterns with different visibility (number of modes) and expected photon counts per pixel. While the effect of the visibility factor is obvious in the high count regime, it becomes harder to see in the low count regime.

3.1.1 Excitation pulse-shape factor β_p

Here we discuss the dependency of the visibility (or speckle contrast) on the excitation pulse duration and shape. Therefore we define the partial visibility factor β_p, which neglects all other contributions to the visibility factor other than the pulse shape and the degree of coherence of the emitted radiation. We assume a pulse shape $I_\mathrm{p}(t)$ of a finite extent that excites the fluorescence emitters. For convenience, we use the normalized pulse shape

$$P(t) = \frac{I_\mathrm{p}(t)}{\int_{-\infty}^{\infty} I_\mathrm{p}(t)\, dt}\,. \tag{3.93}$$

The probability that an emitter gets excited, and, therefore, an emission process is triggered, is proportional to $P(t)$. For now, we assume that the complete decay happens within only one decay path (neglecting multiple spectral lines for now), illustrated in Fig. 3.2 as a simplified Jablonski diagram [34]. That is approximately the case when the fluorescence happens after a core-shell electron gets extracted by the photo effect, which occurs within tens of attoseconds or faster [95, 94]. As a consequence, the wave function of the emission of frequency ω_0 excited at $t = 0$ can be expressed as [129]

$$\psi(t) \propto e^{i\omega_0 t} e^{-t/\tau_c} \Theta(t)\,, \tag{3.94}$$

where the step function $\Theta(t) = 1$ for $t \geq 1$ and 0 otherwise. That means that the emission process is assumed to start immediately after the excitation. The wave function of Eqn. (3.94) corresponds to a Lorentzian power spectrum (recall Eqn. (2.36) and Fig. 2.2b), with FWHM $= 2\Gamma$ and $\Gamma = 1/\tau_c$. The intensity is given by $I_{\text{fl}}(t) \propto e^{-2t/\tau_c}\Theta(t)$.
The degree of coherence is then given by

$$|\gamma(\tau)| = \frac{\left|\int_{-\infty}^{\infty} \psi(t)\psi^*(t+\tau)\,dt\right|}{\int_{-\infty}^{\infty}|\psi(t)|\,dt} = e^{-\frac{|\tau|}{\tau_c}}\,. \tag{3.95}$$

Subsequently, the coherence time can be calculated from the degree of coherence (recall Eqn. (2.31)) as

$$\int_{-\infty}^{\infty} e^{-\frac{|\tau|}{\tau_c}}\,d\tau = \tau_c\,, \tag{3.96}$$

and thus identifying the parameter τ_c with this quantity. it should be emphasized that, in our case, the coherence time is twice the lifetime τ_l which is defined as $I_{\text{fl}}(\tau_l) = e^{-1}I_{\text{fl}}(0)$, or $\tau_l = 1/\Gamma_0$, when Γ_0 is the decay constant, obtained as FWHM of the Lorentzian power spectrum ($\Gamma_0 = 2\Gamma$). However, in some publications (e.g., [13]), the lifetime and coherence time were used interchangeably, which is not the case; see [41].

The partial visibility factor β_{p} for two processes triggered at t_1 and t_2 is given by $\beta_{\text{p}}(t_1, t_2) = |\gamma(t_2 - t_1)|^2$, which corresponds to the 'usable signal' part of the second order temporal correlation $g^{(2)}(t_2 - t_1) = 1 + |\gamma(t_2 - t_1)|^2$. The probability that these processes are triggered with the temporal separation $\tau = |t_2 - t_1|$ is given by

$$\Pi(\tau) = \int_{-\infty}^{\infty} P(t)P(t+\tau)\,dt\,, \tag{3.97}$$

the auto-correlation of the normalized pulse shape.
Please note that there are two contradicting approaches on how to continue to calculate β_{p}. In this work, we are using the approach of Lohse et al. [74]. However, there is a second approach by Inoue et al. [58], which is discussed in Appendix A.3.1. There is also demonstrated, for Gaussian pulse shapes, that the difference between both approaches vanishes when the excitation pulse duration outruns the coherence time by a factor 2 or greater.
As mentioned, following the approach of [74], we obtain the partial visibility factor as

$$\beta_{\text{p}}[P(t)] = \int_{-\infty}^{\infty} \Pi(\tau)|\gamma(\tau)|^2\,d\tau\,. \tag{3.98}$$

In the following, we will discuss a few example pulse shapes.

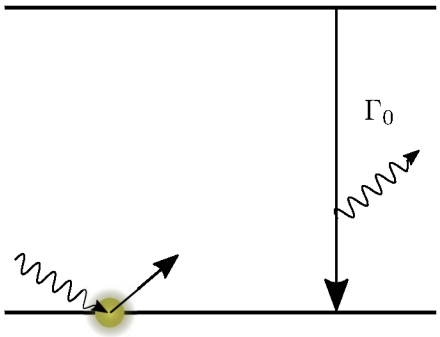

Fig. 3.2.: Simplified Jablonski decay diagram of a single path decay. Note, that the photoeffect is assumed to be instantaneous.

Box-like pulse shape

We assume a box-like pulse shape with the width T:

$$P_T(t) = \begin{cases} 1/T & \text{for } |t| \leq T/2\,, \\ 0 & \text{else}\,. \end{cases} \tag{3.99}$$

The auto-correlation is then given by the triangle function $\Pi(t) = (1/T)\Lambda(\tau/T)$, with $\Lambda(\tau) = 1 - |\tau|$ for $|\tau| \leq 1$ and zero otherwise. The partial visibility factor then evaluates to

$$\beta_{\mathrm{p,box}}(\tau_c, T) = \frac{\tau_c}{T} + \frac{1}{2}\left(\frac{\tau_c}{T}\right)^2 \left(e^{-2(T/\tau_c)} - 1\right)\,, \tag{3.100}$$

which is shown in Fig. 3.3. The short pulse duration limit ($T \ll \tau_c$) returns unity, as expected, and the limit of longer pulse duration yields

$$\lim_{T \gg \tau_c} \beta_{\mathrm{p,box}}(\tau_c, T) = \frac{\tau_c}{T}\,. \tag{3.101}$$

This boxed pulse shape corresponds [41] to the case of a gated detector with T as the exposure time.

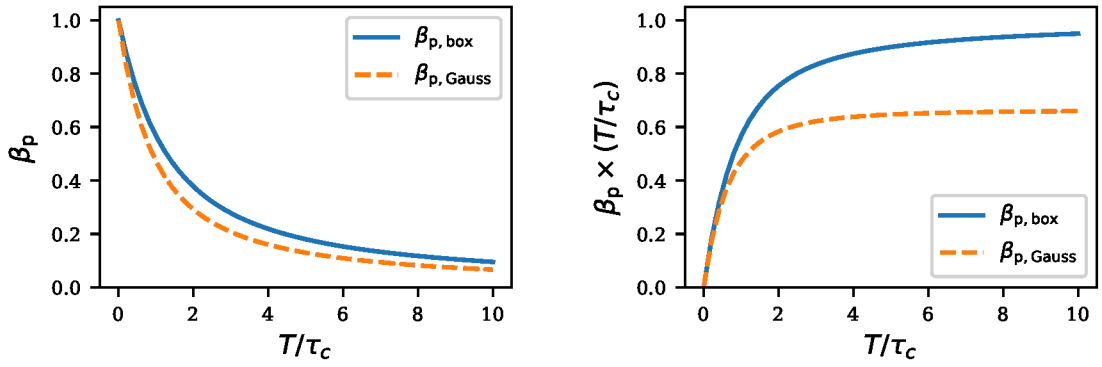

(a) (b)

Fig. 3.3.: **(a)** $\beta_{\mathrm{p,box}}$ and $\beta_{\mathrm{p,Gauss}}$ plotted as a function of T/τ_c. **(b)** Same as (a) but multiplied by the factor T/τ_c to illustrate the convergence $(T/\tau_c)\beta_{\mathrm{p,box}} \to 1$ and $(T/\tau_c)\beta_{\mathrm{p,Gauss}} \to\approx 0.67$ for $T \gg \tau_c$.

Gaussian pulse shape

Next, we assume a Gaussian pulse shape

$$P(t) = \frac{2\sqrt{\ln(2)/\pi}}{T} e^{-\frac{4\ln(2)}{T^2}t^2}\,, \tag{3.102}$$

with the full width at half maximum (FWHM) T. Eqn. (3.98) then evaluates to

$$\beta_{\text{p,Gauss}}(\tau_c, T) = e^{T^2/(\tau_c^2 \ln(4))} \left(1 - \text{erf}\left(\frac{T}{\tau_c\sqrt{\ln(4)}}\right)\right)\,, \tag{3.103}$$

see Fig. 3.3. As expected, the limit $T \ll \tau_c$ returns unity, and the limit of long pulses yields

$$\lim_{T \gg \tau_c} \beta_{\text{p,Gauss}}(\tau_c, T) = \sqrt{\frac{\ln(4)}{\pi}}\frac{\tau_c}{T} \approx \frac{\tau_c}{1.5T}\,. \tag{3.104}$$

For the evaluations of experimental data in this work, we assume a Gaussian pulse shape and therefore use $\beta_{\text{p}} = \beta_{\text{p,Gauss}}$.

SASE pulse

Modern XFELs operate in the self-amplified spontaneous emission (SASE) regime, where the temporal pulse structure is composed of multiple spikes [104, 76]. We will not discuss details of the SASE process in this work. Instead, numerical simulations based on the model presented in [100] were used to obtain examples of SASE pulse shapes. Simulated example pulses for two different mean FWHM pulse durations ($3\,\text{fs}$ and $15\,\text{fs}$) are plotted in Fig. 3.4a and 3.4b, and the corresponding auto correlations in Fig. 3.4c and 3.4d. Therefore, a photon energy of $E = 7.15\,\text{keV}$ and an energy bandwidth of $0.1\,\%$ was assumed. While the pulse shapes are pretty spiky, their auto-correlations are much smoother and have a quite Gaussian-like shape.

1000 pulses for $3\,\text{fs}$ and $15\,\text{fs}$ each were simulated, and the corresponding partial visibility factors for emission with a coherence time of $\tau_c = 0.8\,\text{fs}$ were calculated. The resulting mean partial visibility factors are

$$\begin{aligned}\langle\beta_{\text{p,SASE}}(T = 3\,\text{fs}, \tau_c = 0.8\,\text{fs})\rangle &= 0.168 \pm 6.2 \times 10^{-4}\,,\\ \langle\beta_{\text{p,SASE}}(T = 15\,\text{fs}, \tau_c = 0.8\,\text{fs})\rangle &= 0.0355 \pm 6.8 \times 10^{-5}\,.\end{aligned} \tag{3.105}$$

The second case is as good as equivalent to the corresponding $\beta_{\text{p,Gauss}}$; however, $\langle\beta_{\text{P,SASE}}(T = 3\,\text{fs}, \tau_c = 0.8\,\text{fs})\rangle$ is approximately $6\,\%$ lower than it would be for the Gaussian pulse case. Justified by these quite similar results of $\beta_{\text{P,SASE}}$ and $\beta_{\text{p,Gauss}}$, we will assume Gaussian-shaped excitation pulses for the analysis of experimental data in this work.

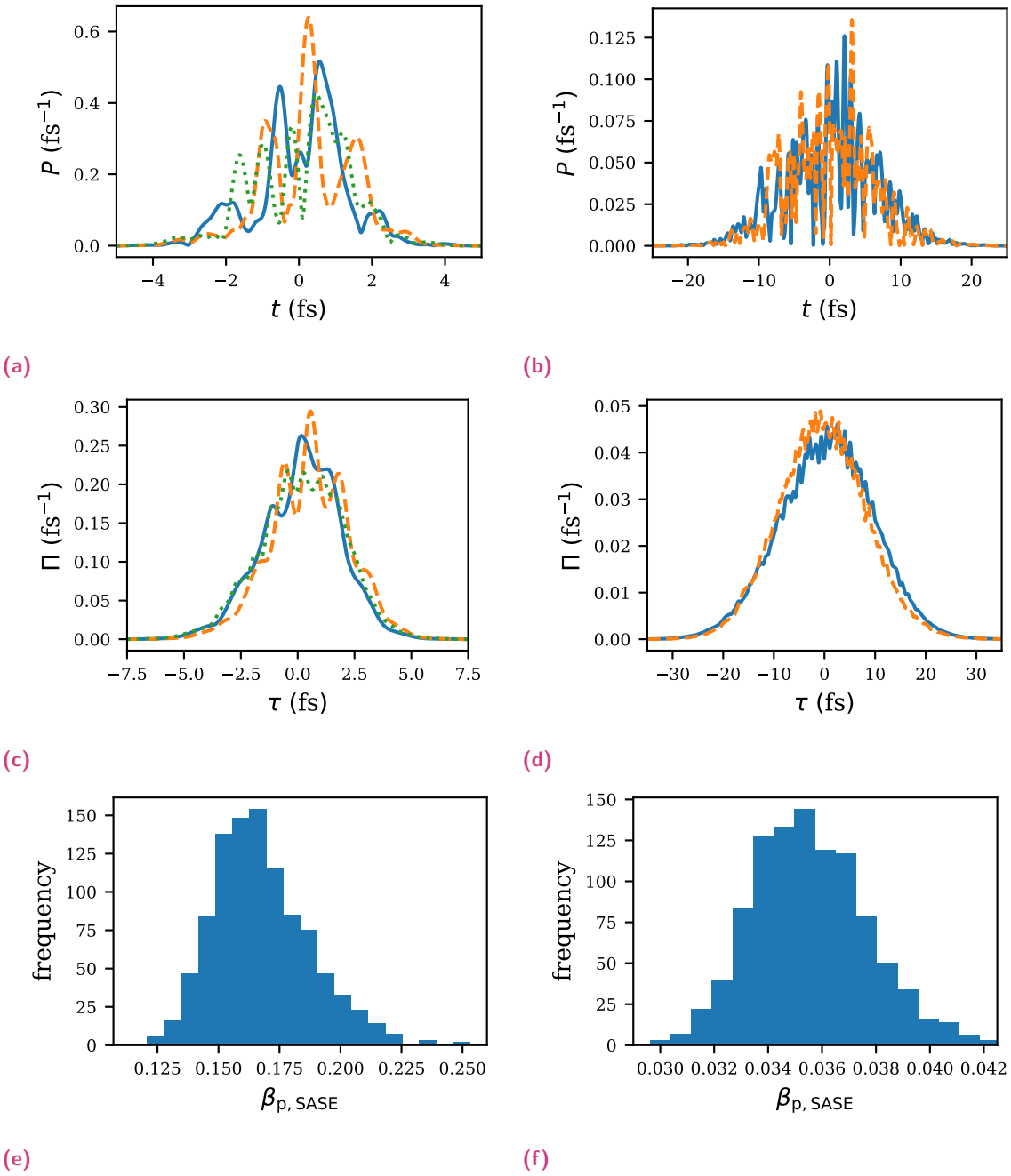

Fig. 3.4.: Simulated SASE pulses for photon energy of $E = 7.15\,\mathrm{keV}$ and an energy bandwidth of $0.1\,\%$. **(a)** Three examples of pulses with an average FWHM pulse duration of $T = 3\,\mathrm{fs}$, and **(b)** two examples with $T = 15\,\mathrm{fs}$. The corresponding auto-correlations $\Pi(\tau)$ are plotted in **(c)**, corresponding to the pulses in (a) and in **(d)** corresponding to (b), respectively. **(e)** partial visibility factor $\beta_{\mathrm{P,SASE}}$ for 3 fs average FWHM pulse duration and an assumed coherence time of $\tau_c = 0.8\,\mathrm{fs}$. The mean visibility is $\langle\beta_{\mathrm{P,SASE}}(T = 3\,\mathrm{fs}, \tau_c = 0.8\,\mathrm{fs})\rangle = 0.168$ with a RMS of $\sigma_{\mathrm{P,SASE}} = 0.02$. **(f)** partial visibility factor $\beta_{\mathrm{P,SASE}}$ for 15 fs average FWHM pulse duration and $\tau_c = 0.8\,\mathrm{fs}$. The mean visibility is $\langle\beta_{\mathrm{P,SASE}}(T = 15\,\mathrm{fs}, \tau_c = 0.8\,\mathrm{fs})\rangle = 0.0355$ with a RMS of $\sigma_{\mathrm{P,SASE}} = 0.002$.

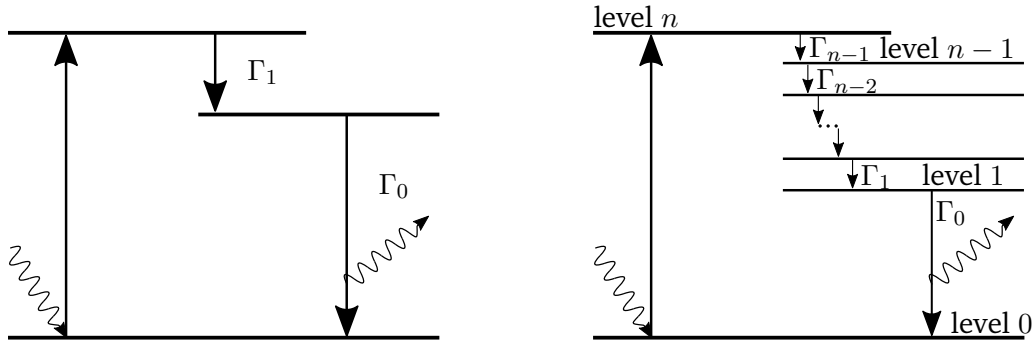

Fig. 3.5.: Simplified Jablonski decay diagrams. **(a)** Two-step decay schema. **(b)** Multi-step decay schema. Γ_0 refers to the decay rate that produces the photon we are interested in.

Multi-stage decay

So far, we have assumed that the emission process starts immediately after absorption. However, this is rather a special case. When the excitation does not happen by ejecting an electron, the radiative decay of interest is often only the last of many (radiative or non-radiative) decays. This is mostly the case when working in a regime of lower energies than X-rays (visible light, ultraviolet, infrared, et c.) [21]. First, we discuss the case of a two-step decay: one prior to the fluorescence of interest, with the decay constant Γ_1 and the photon emitting decay with the decay constant Γ_0. The simplified Jablonski diagram is shown in Fig. 3.5a. Since we assume that the second decay is stationary (constant in phase), we are only interested in the rate at which the intermediate level gets excited. In the case of exponential decay, this is given by the convolution of the exciting pulse with the first decay $I_\mathrm{P}(t) * \exp(-\Gamma_1 t)$. With this, we can define an effective normalized excitation pulse shape as

$$\tilde{P}(t) = \frac{\int_{-\infty}^{\infty} I_\mathrm{P}(t'+t)\exp(-\Gamma_1 t')\,dt'}{\int_{-\infty}^{\infty}\int_{-\infty}^{\infty} I_\mathrm{P}(t'+t)\exp(-\Gamma_1 t')\,dt'\,dt}\,, \tag{3.106}$$

which excites the level from which the fluorescence of interest is triggered. The partial visibility factor is then calculated as described in Eqn. (3.98), with $\tilde{\Pi}(\tau) = \tilde{P} * \tilde{P}$ instead of $\Pi(\tau)$. Multiple-step decays with n decays prior to the fluorescence decay of interest, are illustrated in Fig. 3.5b. In that case $\tilde{P}$ can be calculated by multiple convolutions as

$$\tilde{P}(t) = P(t) * \left(\Gamma_n e^{-\Gamma_n t}\right) * \left(\Gamma_{n-1} e^{-\Gamma_{n-1} t}\right) * \cdots * \left(\Gamma_1 e^{-\Gamma_1 t}\right)\,. \tag{3.107}$$

Please note that such multi-stage decays prior to the fluorescence can significantly reduce the visibility factor and are impractical for any photon-photon correlation imaging attempts. In these cases a gating detector might be favorable, which Eqn. (3.100) can describe, as mentioned earlier.

3.1.2 Finite speed of light factor β_c

When the spatial extent of the emitter distributions exceeds the speed of light times coherence time $\Delta r > c_0 \tau_c$, the visibility factor might suffer. Here we quantify this effect and discuss the implied limitations for experimental setups. Therefore, we assume two emitters at the positions $\vec{r}_1$ and $\vec{r}_2$ that get excited by an excitation pulse, propagating along the z-axis, as illustrated in Fig. 3.6. Considering a delta distributed pulse, the time delay of the excitation is given by the spatial distance projected onto the z-axis

$$\tau_0 = \frac{1}{c_0} (\vec{r}_2 - \vec{r}_1) \cdot \hat{e}_z \,. \tag{3.108}$$

The integrated intensity at $I(\vec{k}_1)$ is composed of the emission from both emitters, with an emission time delay given by the projection of their distance at the direction of $\vec{k}_1$

$$\tau_1 = \frac{1}{c_0} (\vec{r}_1 - \vec{r}_2) \cdot \frac{\vec{k}_1}{|\vec{k}_1|} \,. \tag{3.109}$$

Note that the minuend and subtrahend were swapped compared to the calculation of τ_0. The time emission time delay for τ_2 for the integrated intensity measured in the direction of $\vec{k}_2$ is calculated equivalently ($\tau_2 = c_0^{-1} (\vec{r}_1 - \vec{r}_2) \cdot \vec{k}_2 / |\vec{k}_2|$).
The combined visibility factor $\beta_\mathrm{p}\beta_c$ can then be expressed as [74]

$$\beta_\mathrm{p}\beta_c = \int_{-\infty}^{\infty} \Pi(\tau) \, |\gamma(\tau + \tau_0 + \tau_1)| \, |\gamma(\tau + \tau_0 + \tau_2)| \, d\tau \,, \tag{3.110}$$

for arbitrary auto correlated normalized pulse shapes $\Pi(\tau)$ (recall Eqn. (3.97)). Apparently, the effect of the finite speed of light cannot be separated from the excitation pulse shape and duration. Also, β_c comes with the quite cumbersome property of being dependent on the direction of $\vec{k}_1$ and $\vec{k}_2$. A variation of the visibility factor for the usable signal in $g^{(2)}$, not only depending on $\vec{q}$ but also on the individual $\vec{k}$ vectors, could render a real 'challenge' (problem) to imaging attempts.
For the sake of simplicity, we assume that $\tau_1 \approx \tau_2$ and define $\Delta\tau := \tau_0 + \tau_1$, so we can express β_c as

$$\beta_c = \frac{\int_{-\infty}^{\infty} \Pi(\tau) \, |\gamma(\tau + \Delta\tau)|^2 \, d\tau}{\int_{-\infty}^{\infty} \Pi(\tau) \, |\gamma(\tau)|^2 \, d\tau} \,. \tag{3.111}$$

Assuming a Gaussian excitation pulse with FWHM T, a minimum estimation of β can be given by

$$\beta_c(\Delta\tau, T) \geq e^{-\ln(4)\left(\frac{\Delta\tau}{T}\right)^2} \,. \tag{3.112}$$

A derivation is given in Appendix A.3.2. Interestingly, this minimum estimation is independent of the coherence time τ_c. However, as a rule of thumb, a longer coherence time yields a higher β_c.

The detector geometry and emitter distribution with the highest possible $\Delta\tau$ would be a detector placed in the backward direction (in the direction where the excitation pulse origins from) so that $\Delta\tau = 2r/c$ when two emitters are placed along the z-axis, separated by the distance r. For example, assuming a sample with a diameter of $r = 100\,\mathrm{nm}$ and an excitation

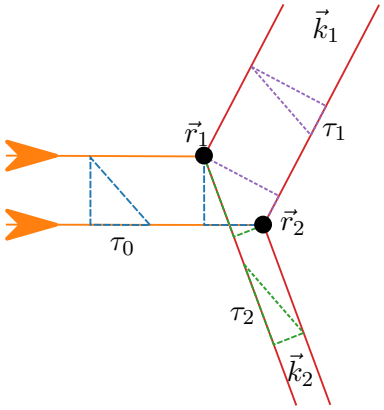

Fig. 3.6.: Sketch of two emitters at the positions $\vec{r}_1$ and $\vec{r}_2$, that radiate in the directions (wave-vectors) $\vec{k}_1$ and $\vec{k}_2$. For details see text.

pulse FWHM of $T = 3\,\mathrm{fs}$, the lowest possible contribution with the most unfavorable possible detector placement would yield a $\beta_c(\vec{k}_1, \vec{k}_2) \geq 0.93 \,|\, \forall\, \vec{k}_1, \vec{k}_2$.
The analysis in this section suggests that for the design of an IDI experiment, detector size and placement must be considered together with the sample size. Also, there could be rare occasions where a slight increase in the excitation pulse duration could help to get a clearer usable signal. For the experiments presented in this work, β_c contributions were neglected since the samples used in the experiment, presented later on in this chapter, were sufficiently small for the given pulse durations, and the setup of Chapter 5 was designed in a 'forward geometry', where $\tau_1 \approx \tau_2 \approx -\tau_0$ and thus $\beta_c \approx 1$.

3.1.3 Polarization factor β_{pol}

Photons only interfere if they are in the same polarization state. Therefore, if the emission is not polarized (which is usually the case for fluorescence) or only partially polarized, the visibility factor needs to be adjusted. Therefore we define the polarization visibility factor as

$$\beta_{\mathrm{pol}} = \frac{1 + \mathcal{P}^2}{2}\,, \tag{3.113}$$

with the degree of polarization $\mathcal{P} = 0$ for unpolarized and $\mathcal{P} = 1$ for fully polarized emission. Eqn. (3.113) can be derived, following Goodman's argumentation [41], by assuming two uncorrelated partial intensities $I = I_1 + I_2$. The correlation can therefore be written as

$$\begin{aligned} &\langle (I_1(t) + I_2(t))\,(I_1(t+\tau) + I_2(t+\tau))\rangle_t \\ &= \langle I_2(t) I_2(t+\tau)\rangle_t + \langle I_2(t) I_2(t+\tau)\rangle_t + 2\langle I_1(t) I_2(t+\tau)\rangle_t\,. \end{aligned} \tag{3.114}$$

The first two summands (using Siegerts relation, recall Eqn. (2.33)) evaluate to

$$\langle I_j(t) I_j(t+\tau)\rangle_t = \langle I_j(t)\rangle_t^2 \left(1 + |g^{(1)}(\tau)|^2\right) \,|\, j = \{1, 2\}\,, \tag{3.115}$$

and since I_1 and I_2 are uncorrelated ($|g^{(1)}| = 0$) we obtain

$$2\langle I_1(t) I_2(t+\tau)\rangle_t = 2\langle I_1(t)\rangle_t \langle I_2(t)\rangle_t\,. \tag{3.116}$$

We define the means of the partial intensities, using the degree of polarization $\mathcal{P}$ as

$$\begin{aligned}\langle I_1(t)\rangle_t &= \frac{1}{2}\langle I(t)\rangle_t\,(1+\mathcal{P})\ ,\\ \langle I_2(t)\rangle_t &= \frac{1}{2}\langle I(t)\rangle_t\,(1-\mathcal{P})\ .\end{aligned} \tag{3.117}$$

By substituting Eqn. (3.117) into Eqn. (3.118) and using Eqn. (3.115) and Eqn. (3.116), we obtain

$$\begin{aligned}&\langle (I_1(t)+I_2(t))\,(I_1(t+\tau)+I_2(t+\tau))\rangle_t\\ &= \langle I(t)\rangle_t\left(1+\frac{1}{2}\left(1+\mathcal{P}^2\right)|g^{(1)}(\tau)|^2\right)\ ,\end{aligned} \tag{3.118}$$

where we identify the polarization visibility factor as stated in Eqn. (3.113).

3.1.4 Multi emission lines factor β_{lines}

It is not always possible to distinguish between the fluorescence lines. In this work, we are using K-line fluorescence, which can be split into $\mathrm{K}_{\alpha,1}$, $\mathrm{K}_{\alpha,2}$, and K_{β} fluorescence (as discussed in Section 2.4). It is often possible to filter the K_{β} fluorescence by using the element with the atomic number $Z-1$ prior to one of the emitters, with the atomic number Z, since the K-edge of the $Z-1$ element is often placed between the K_{α} and K_{β} emission, see Tab. 2.1. The K_{α} lines, however, can usually not be distinguished.

Assume that we have filtered everything (K_{β}, coherently scattered photons, et cetera) but $\mathrm{K}_{\alpha,1}$ and $\mathrm{K}_{\alpha,2}$. Then $\mathrm{K}_{\alpha,1}$-photons do only interfere with $\mathrm{K}_{\alpha,1}$-photons and $\mathrm{K}_{\alpha,2}$- with $\mathrm{K}_{\alpha,2}$-photons, respectively. We, therefore, need to calculate the probability of detecting two photons from the same line. The line ratio, after filtering, is calculated as

$$R_j = \frac{R_{\mathrm{K}_{\alpha,j}}}{R_{\mathrm{K}_{\alpha,1}}+R_{\mathrm{K}_{\alpha,2}}}\ \text{for}\ j=\{1,2\}\,, \tag{3.119}$$

and we obtain the partial visibility factor as

$$\beta_{\text{lines}} = R_1^2+R_2^2\,. \tag{3.120}$$

For the elements displayed in Tab. 2.1, where $R_{\mathrm{K}_{\alpha,1}} \approx 2R_{\mathrm{K}_{\alpha,2}}$, the partial visibility factor is approximately $\beta_{\text{lines}} \approx 5/9$.
Eqn. (3.120) can simply be extended for arbitrarily many lines (as long as they have approximately the same line width) as

$$\beta_{\text{lines}} = \sum_{j=1}^{n} R_j^2\,. \tag{3.121}$$

It should be mentioned that Eqn. (3.121) assumes the lines to be clearly separated. If this is not the case, β_{lines} must be adjusted by the then-occurring optical beats.

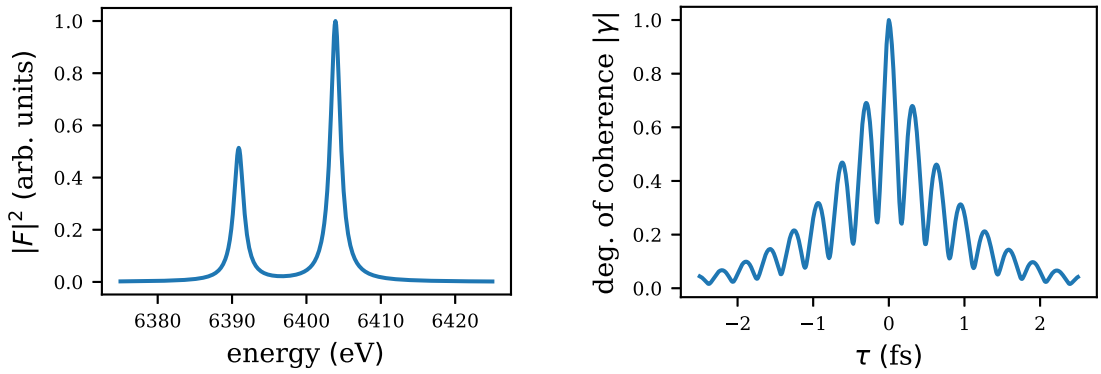

(a) (b)

Fig. 3.7.: **(a)** Power spectrum of iron K_α fluorescence, calculated from values given in Tab. 2.1 and 2.2. **(b)** Degree of coherence, calculated from (a).

Another way to model the effect of multiple lines is via the complex degree of coherence. However, this presumes the β_p calculation as proposed by Inoue et al. [58], discussed in Appendix A.3.1. For example, the power spectrum of iron $K_{\alpha,1}$ and $K_{\alpha,2}$ fluorescence is given in Fig. 3.7a. The degree of coherence can be calculated from this spectrum (recall the discussion in Section 2.2.1) and is displayed in Fig. 3.7b. The effective coherence time $\tau_{c,\mathrm{eff}}$, calculated from this degree of coherence, equates nearly exactly $\tau_{c,\mathrm{eff}} = (R_1^2 + R_2^2)\tau_c \approx 0.45\,\mathrm{fs}$, where $\tau_c = 0.82\,\mathrm{fs}$ is the coherence time of one single line.

3.1.5 Speckle sampling factor β_SPS

Spatially larger emitter distributions lead to smaller speckles (recall the coherence area obtained by the Van Cittert-Zernike theorem Eqn. (2.44)). If the speckle size is smaller than the detector (or rather a detector-pixel), the detector will integrate over multiple speckles and, therefore, over independent contributions, which leads to a decrease in visibility. To quantify this effect, we assume a symmetric 2D Gaussian emitter distribution with the RMS value σ_ρ. Further, we assume that the emitters are emitting light with the wavelength λ, which is detected by a pixelated detector placed at the distance z. For this discussion, we also assume the classical limit of continuous intensity. The $g^{(2)}$ signal is then given by a Gaussian on top of an offset as $g^{(2)}(q_x, q_y) = 1 + e^{-(q_x^2+q_x^2)/(2\sigma^2)}$ with the RMS given by

$$\sigma = \frac{z\lambda}{\sqrt{8}\pi\sigma_\rho}\,. \tag{3.122}$$

A square detector pixel with the area $\Delta x \times \Delta x$ can be described by the top-head function defined by

$$\Xi(x,y) := \begin{cases} \dfrac{1}{(\Delta x)^2} & \text{for } |x| < \Delta x/2 \text{ and } |y| < \Delta x/2\,, \\ 0 & \text{else}\,, \end{cases} \tag{3.123}$$

that is convolved with the measured integrated intensities (photon counts) $I_{\text{measured}} = (I * \Xi)(x,y)$. For the $g^{(2)}$ signal this means a convolution with the cross-correlation[1] of $\Xi(x,y)$ as $g^{(2)}_{\text{measured}} = (g^{(2)} * (\Xi \star \Xi))(q_x, q_y)$. This cross-correlation of the top-hat function has the following form

$$(\Xi \star \Xi)(x,y) = \begin{cases} \dfrac{1}{(\Delta x)^2}\left(1 - \dfrac{|x|}{\Delta x}\right)\left(1 - \dfrac{|y|}{\Delta x}\right) & \text{for } |x| < \Delta x \text{ and } |y| < \Delta x\,, \\ 0 & \text{else}\,. \end{cases} \tag{3.124}$$

As we will discuss later in Section 4.1.1, in the classical limit and only in the classical limit, the visibility factor can be expressed by $\beta = g^{(2)}_{\text{cl}}(0) - 1$. Therefore we can define the speckle sampling visibility factor as[2]

$$\beta_{\text{SPS}} := \left(g^{(2)}_{\text{cl}} * (\Xi \star \Xi) - 1\right)(q_x = 0, q_y = 0)\,. \tag{3.125}$$

We can now calculate β_{SPS} for the Gaussian emitter distribution with its also Gaussian-shaped $g^{(2)}$-signal as

$$\begin{aligned} \beta_{\text{SPS, Gaussian}}(\sigma, \Delta x) = 1 &+ 4e^{-\frac{\Delta x^2}{\sigma^2}}\left(e^{\frac{\Delta x^2}{2\sigma^2}} - 1\right)^2 \frac{\sigma^4}{\Delta x^4} \\ &+ 4\sqrt{2\pi}\left(e^{-\frac{\Delta x^2}{2\sigma^2}} - 1\right)\operatorname{erf}\!\left(\frac{\Delta x}{\sqrt{2}\sigma}\right)\frac{\sigma^3}{\Delta x^3} + 2\pi \operatorname{erf}\!\left(\frac{\Delta x}{\sqrt{2}\sigma}\right)^2 \frac{\sigma^2}{\Delta x^2}\,. \end{aligned} \tag{3.126}$$

This is plotted in Fig. 3.8 as a function of $\sigma/\Delta x$. When the FWHM of the speckle has the same size as the pixel edge, the expected visibility is halved: $\beta_{\text{SPS, Gaussian}}(\sigma/\Delta x \approx 1/2.355) \approx 0.5$. For double sized speckles we obtain $\beta_{\text{SPS, Gaussian}}(\sigma/\Delta x \approx 2/2.355) \approx 0.81$ and as a rule of thumb, one can say that when the FWHM speckle size exceeds four times the pixel size, the β_{SPS} contribution can be neglected $\beta_{\text{SPS, Gaussian}}(\sigma/\Delta x > 4/2.355) > 0.94$.

Please note that this discussion assumed only two dimensions. For detectors covering a huge solid angle and, therefore, a non-negligible q_z, the speckle shape is different for pixels located at different $\vec{k}$. For example, think of a flat 2D detector placed close to the sample: the pixels in the center will cover significantly smaller solid angles than the ones at the edges. In that case, the here-discussed β_{SPS} can only be seen as an approximation.

3.1.6 Further contributions $\beta_?$

Besides the previously mentioned partial factors of the visibility factor, there can be further partial factors that are not quantified at this point. The β_{p} factor, for example, assumes that the degree of coherence stays constant during the excitation. This is not the case if the pulse is very

[1] The cross-correlation is defined by $(f \star g)(\vec{x}) := \int_{-\infty}^{\infty} f^*(\vec{x}')g(\vec{x} + \vec{x}')\, d^n x'$.

[2] neglecting all other contributions (partial visibility factors) to the visibility factor.

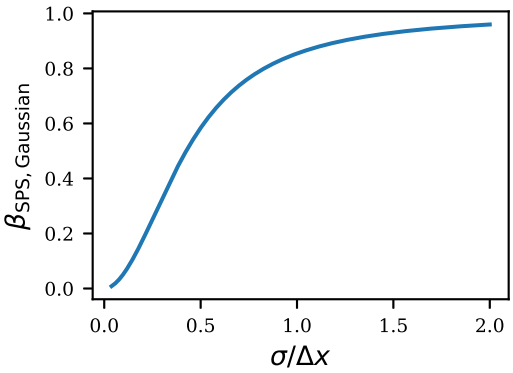

Fig. 3.8.: β_{SPS} plotted as a function of $\sigma/\Delta x$ to illustrate insufficient speckle sampling. Δx denotes the pixel edge length and σ the RMS size of assumed Gaussian shaped speckles.

intense so that the absorption of the emitters saturates. A shortening of XFEL pulse duration via such saturable absorption was demonstrated (using IDI) by Inoue et al. in 2021 [57]. Motivated by that experiment, Sebastian Cardoch investigated the change in fluorescence duration and the energy spectrum depending on the excitation pulse intensity [9]. However, up to this date, no quantitative estimations on the dependency of β on the excitation beam intensity were made and are also not part of this work. IDI and precision measurements of β could be useful tools for further experimental investigations of saturable absorption and quick plasma generation via XFELs.

Further contributions to the visibility factor could also be a background that cannot be distinguished from the signal originating from the sample (e.g., when investigating iron fluorescence, there could be a background from fluorescing beam line components which are containing iron).

3.2 Speckle contrast experiment

The K_α fluorescence of iron nanoparticles (wavelength $\lambda_{Fe,K_\alpha} = 1.94\,\text{Å}$) has been measured using two different excitation pulse durations and where a change in speckle contrast has been observed. The increase in β for the shorter excitation pulse in comparison to the longer one is a clear indication of the feasibility of incoherent diffractive imaging via X-ray fluorescence. The results of this experiment have already been published in [122].

The measurements were carried out at the *Macromolecular Femtosecond Crystallography (MFX)* instrument at the *Linac Coherent Light Source (LCLS)* using the scheme depicted in Fig. 3.9a. The nanoparticles, referred to as iron nanostars [30], had an irregular, star-like shape with a mean diameter of about $50\,\text{nm}$ to $100\,\text{nm}$, see Fig. 3.9b. The nanostars were suspended in toluene at a concentration of $7.9 \times 10^{19}\,\text{mL}^{-1}$ ($0.13\,\text{mol}\,\text{L}^{-1}$). The sample was injected across the focused X-ray beam as a liquid jet formed by a double-flow-focusing nozzle [92, 65]. The jet had a diameter of $2.2\,\mu\text{m}$ and a velocity of $60\,\text{m}\,\text{s}^{-1}$. The XFEL pulses came at a repetition rate of $120\,\text{Hz}$, and the injection ensured that a fresh sample was present for each exposure. The LCLS was operated in two different modes for our measurements to produce pulses of $\sim$15 fs, as estimated using the X-band Transverse Deflecting Cavity (XT-CAV) [68], and $\sim$3 fs, as estimated by settings of the electron pulse compression in the accelerator. The incident X-ray beam of $7.15\,\text{keV}$ was focused to a size of approximately $4\,\mu\text{m}$.

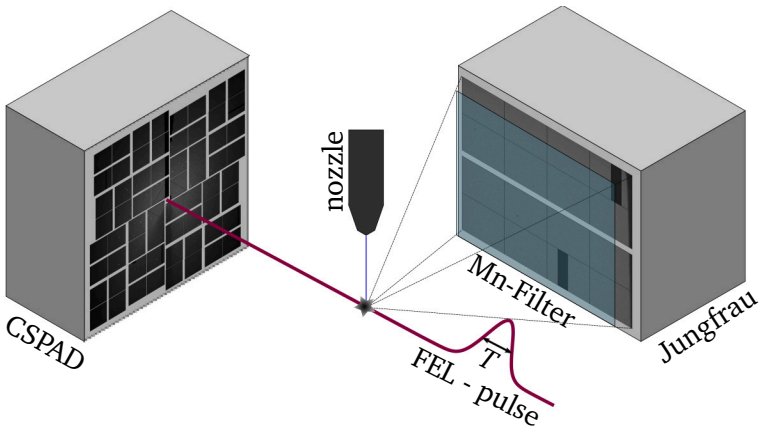

(a)

(b)

Fig. 3.9.: **(a)** Sketch of the experimental setup at the MFX beamline at LCLS. Illustration taken from [122] and modified. **(b)** Transmission electron microscope image of the iron nanoparticles. These figures were already published in [122].

From estimates of the beamline transmission, the mean pulse energy at the interaction point was about $0.1\,\mathrm{mJ}$ for the short and $1.5\,\mathrm{mJ}$ for the long pulses, which corresponds to a peak X-ray intensity at the sample of $8 \times 10^{17}\,\mathrm{W\,cm^{-2}}$ for the long and $2.7 \times 10^{17}\,\mathrm{W\,cm^{-2}}$ for the short pulses, respectively. The fluorescence was measured using a Jungfrau detector [89] oriented at a scattering angle of $90°$ in the horizontal plane. This orientation was chosen to minimize the coherent scattering since the incident X-ray pulse was linearly polarized in the horizontal direction. The detector, with 1000×1000 square pixels, each $75\,\mu\mathrm{m}$ wide, was placed $120\,\mathrm{mm}$ away from the interaction point. A $32.4\,\mu\mathrm{m}$ thick manganese filter was placed in front of the detector to attenuate the K_β fluorescence by the factor 1.4×10^{-4} and any coherently scattered photons by the factor 1.8×10^{-4} while transmitting $24.5\,\%$ of the K_α fluorescence [52].

The concentration of the nanoparticles was adjusted such that, on average, $11\,\%$ of the pulses intersected a particle. This hit rate was measured simply from the sum of fluorescence photon counts (above a certain threshold) on the Jungfrau detector, monitored using the program *OnDA* [82].

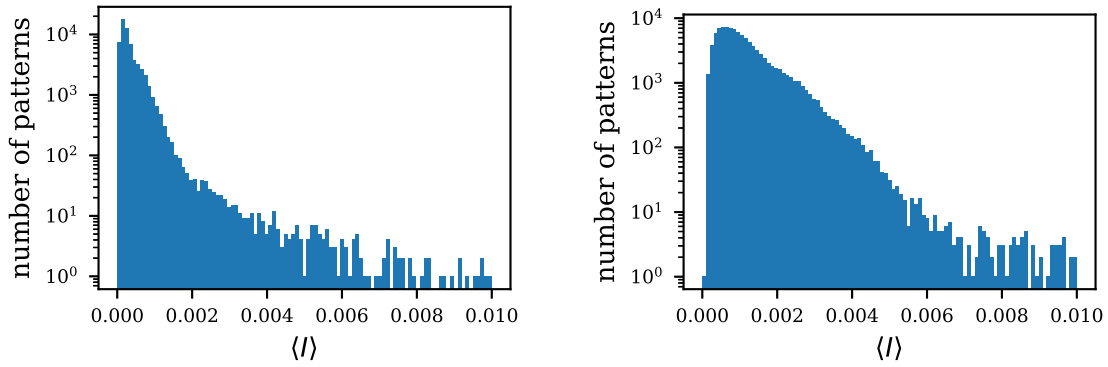

(a) (b)

Fig. 3.10.: **(a)** Mean photon count per pixel at Jungfrau detector for 3 fs XFEL pulse patterns with an average mean photon count of $\langle\langle I\rangle\rangle = 1.2 \times 10^{-3}$ and **(b)** for 15 fs XFEL pulse patterns with an average mean photon count of $\langle\langle I\rangle\rangle = 3.8 \times 10^{-4}$. These figures were already published in [122].

After the experiment, the frames containing fluorescence counts were processed by masking bad pixels and shadows of the shielding around the edges, leaving 895 000 'good' pixels per frame. The conversion of each detector frame from arbitrary detector units (ADU) to photon counts is described in Appendix B.1. The number of frames with detected photons, 'events', was 98 000 and 61 000 for the 'long' 15 fs and 'short' 3 fs, respectively. Histograms of the mean number of photons $\langle I\rangle$, in each event, are given in 3.10b for the short and in 3.10a for the long pulses. We can see that in both cases, the mean photon counts are less than one photon per 100 pixels for almost all frames. We also recognize that the mean counts vary considerably in both datasets. This fluctuation of the measured counts was in part due to the sample delivery, where the nanoparticles arrive randomly in the beam focus, and in part due to the fluctuations of the pulse energy of the XFEL beam.

3.2.1 Expected speckle contrast

We assume a Gaussian-shaped pulse (FWHM T) for the excitation. The coherence time of iron K_α, with a line-width (FWHM) of $\Gamma = 1.61\text{eV}$ [67], is $\tau_c = 2\hbar/\Gamma = 0.8\text{fs}$. Furthermore, iron has a line ratio of around two to one between $K_{\alpha,1}$ and $K_{\alpha,2}$.
Based on these considerations, the maximal speckle contrast, combined from $\beta_{\text{max. expected}} = \beta_{\text{p,Gauss}}\beta_{\text{pol}}\beta_{\text{lines}}$, that can be expected is

$$\begin{aligned} \beta_{\text{max. expected}}(T) &\approx \frac{5}{27}\frac{0.8\text{fs}}{T}\,, \\ \beta_{\text{max. expected}}(3\text{fs}) &\approx 0.049\,, \\ \beta_{\text{max. expected}}(15\text{fs}) &\approx 0.01\,. \end{aligned} \tag{3.127}$$

However, as previously discussed, more factors act to reduce the achievable speckle contrast below the estimate of Eqn. (3.127). E.g., the speckle sampling would affect the expected speckle contrast, as discussed in Section 3.1.5.

When we assume that the sample size (diameter) between $50\,\mathrm{nm}$ and $100\,\mathrm{nm}$ can be approximated by a Gaussian emitter distribution with FWHM of $\sigma = 75\,\mathrm{nm}$ Eqn. (3.126) returns a value of $\beta_{\mathrm{SPS}} \approx 0.88$.

3.3 Estimation of speckle contrast

The low mean photon counts of our measurements is a situation not uncommon in the analysis of X-ray speckle patterns, most of which are made under the assumption of very limited signal levels [54, 99, 55]. Given that the measured counts follow the negative binomial distribution of Eqn. (2.69), the most straightforward method to determine the speckle contrast of a low-signal pattern is to estimate the expectation value of the mean photon counts μ from the measured mean photon count $\langle I \rangle$ and the variance $\mathrm{Var}(I)$ from the square of the standard deviation of the photon count values I. Then simply solving $\mathrm{Var}(I) = \mu + \beta\mu^2$ (recall Eqn. (2.68)) for the visibility factor yields

$$\beta_{\mathrm{V}} = \frac{\mathrm{Var}(I) - \langle I \rangle}{\langle I \rangle^2}\,. \tag{3.128}$$

We call the speckle contrast estimated this way β_{V}.
Another approach is to count the detector pixels that measure one or two photons [54, 88, 115]. Given the measured frequency (estimate for probability) of one-photon values, $P_1 = P_{\mathrm{NB}}(1|\langle I \rangle, \beta)$, and the two-photon values, P_2, we find from Eqn. (2.69)

$$\beta_{1,2} = \frac{2P_2 - P_1\langle I \rangle}{(P_1 - P_2)\langle I \rangle}\,, \tag{3.129}$$

where the subscripts 1 and 2 stand for the use of only 1 and 2 photon counts. Note that for $\mu = 1$, $\beta_{1,2}$ is not defined since $P_1 = 2P_2\,|\,\forall\beta$. This estimate does not appear to have any advantage over β_{V} but has some significant disadvantages when the mean photon count approaches or exceeds 1, as we will discuss later in this section. However, since approximated forms of $\beta_{1,2}$ are often mentioned in literature [54, 88, 115], which we discuss in Appendix A.3.3, we include $\beta_{1,2}$ in the following analysis. Furthermore, speckle contrast estimation requires a minimum number of simultaneously measured values (e.g., pixels) when the expected mean photon count is not perfectly constant between the individual measurements. Even though the number of pixels was not a concern in our experiments, the effect of an insufficient pixel count is discussed in Appendix A.3.4. Applying Eqn. (3.128) or Eqn. (3.129) to each of the $61\,000$ short-pulse patterns and separately to each of the $98\,000$ long-pulse patterns, then averaging the results, we obtain the following speckle contrast estimates

$$\begin{aligned}
\langle \beta_{\mathrm{V}}(3\mathrm{fs}) \rangle &= 0.54 \pm 0.32\,,\\
\langle \beta_{\mathrm{V}}(15\mathrm{fs}) \rangle &= 0.0250 \pm 0.0007\,,\\
\langle \beta_{1,2}(3\mathrm{fs}) \rangle &= 0.14 \pm 0.11\,,\\
\langle \beta_{1,2}(15\mathrm{fs}) \rangle &= -0.050 \pm 0.011\,.
\end{aligned} \tag{3.130}$$

These estimates are much higher than the optimistic expectations of Eqn. (3.127), except for the negative value for $\beta_{1,2}$ at $15\,\mathrm{fs}$. The largest estimate is even unphysical since a speckle contrast of $\beta = 0.5$ corresponds to perfectly coherent but unpolarized light, which is completely impossible here since we did not discriminate between $\mathrm{K}_{\alpha,1}$ and $\mathrm{K}_{\alpha,2}$ fluorescence. Also, the differences between $\langle\beta_\mathrm{V}\rangle$ and $\langle\beta_{1,2}\rangle$ are unreasonably significant. These estimates can not be trusted. The reason for this is a very low mean photon count for the vast majority of patterns combined with a significant variation of $\langle I\rangle$ from pattern to pattern, as evident in Fig. 3.10b and Fig. 3.10a. Histograms of the individual (single pattern) estimates are shown in Fig. 3.11a and Fig. 3.11b for the short and the long pulses, respectively. The abscissae of both plots are logarithmic, highlighting the long-tailed distribution of these single pattern speckle contrast estimations, which severely skews the means given in Eqn. (3.130). Hints for how to find better estimates if the speckle contrast can be found by subsets of patterns chosen from various bins of $\langle I\rangle$ in the histogram of Fig. 3.11c. We find that the distributions of β estimates depend on the mean counts $\langle I\rangle$, as seen in Fig. 3.11d. While a low $\langle I\rangle$ leads to a large fluctuation of β estimates, this transmutes to a more compact Gaussian-like distribution for larger $\langle I\rangle$ values. This observation that the shape of the single pattern speckle contrast estimates is highly dependent on the mean photon counts suggests that a weighted average is more appropriate than an arithmetical mean.

3.3.1 Weighted speckle contrast

To underline the importance of weighting the speckle contrast estimates from the individual patterns, 15^5 speckle patterns with an expectation value of $\mu = 1 \times 10^{-4}$ photons per pixel, 15^5 more patterns with $\mu = 3 \times 10^{-4}$, and 1.5×10^4 speckle patterns with $\mu = 3 \times 10^{-2}$, have been simulated. That was done simply by generating random numbers that follow the Bose-Einstein distribution (recall Eqn. (2.63)), corresponding to full contrast ($\beta_0 = 1$). Each pattern consisted of one million pixels – that is, one million random numbers – similar to that of our experiment and sufficiently large to ensure that the mean estimate converged to the correct value, as demonstrated in Appendix A.3.4.

Histograms of the per-pattern speckle contrast estimates are plotted in Fig. 3.12 for three different expectation photon counts. For the lowest signal level of 10^{-4} counts per pixel (corresponding to an average of only 100 photons per pattern), the probability of observing at least one two-photon hit is vanishingly small (approximately $1\,\%$). Thus, most patterns do not have any pixel with a value of 2 or higher. In this case $P_{j\geq 2} = 0$ and $P_1 = \langle I\rangle$, and therefore $\mathrm{Var}(I) = \langle I\rangle - \langle I\rangle^2$, so that Eqn. (3.128) evaluates to $\beta_\mathrm{V} = -1$. Likewise Eqn. (3.129) with $P_2 = 0$ immediately returns $\beta_{1,2} = -1$. These values occur predominantly for $\langle I\rangle < 8.34 \times 10^{-4}$, as seen in the histograms of Fig. 3.12a and 3.12b. Conversely, a pattern containing at least one pixel with a value of 2 or higher will return an overly large β estimate using Eqn. (3.128) or Eqn. (3.129).

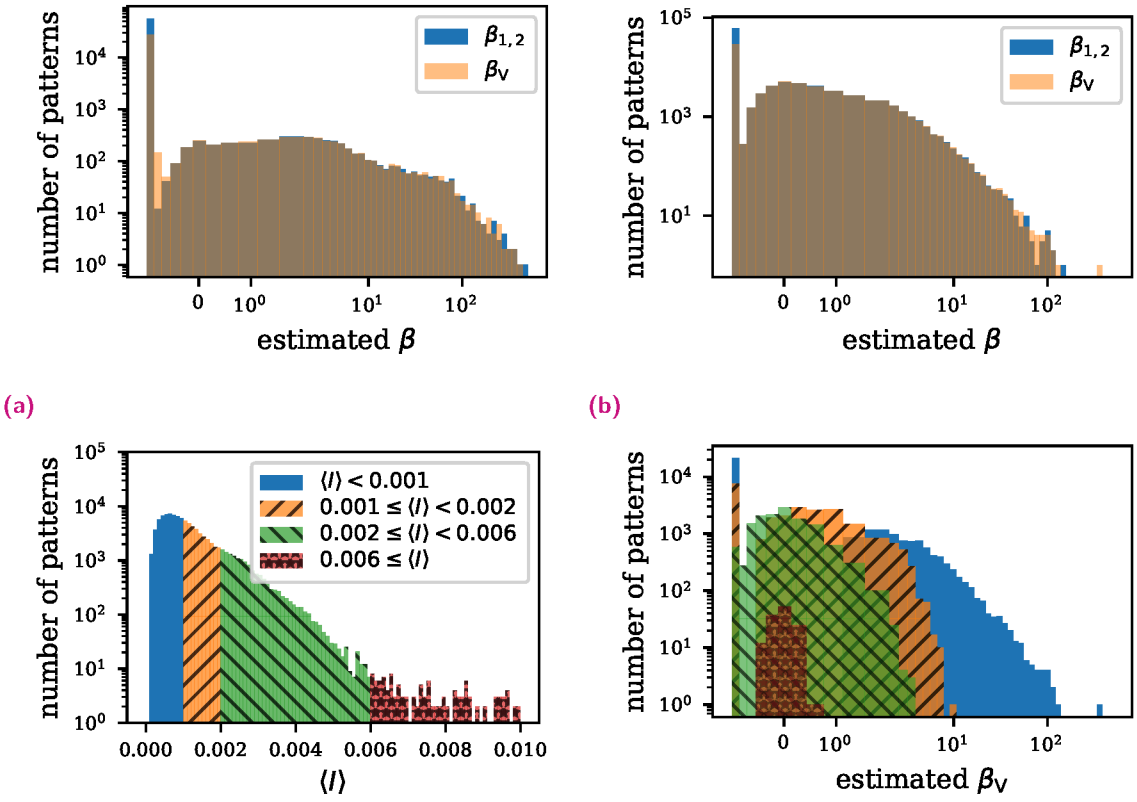

Fig. 3.11.: Histograms of single patterns speckle estimates $\beta_{1,2}$ and β_V, obtained from X-ray fluorescence photons emitted by iron nano-stars. **(a)** Fluorescence excited by 3 fs FEL pulses. **(b)** Fluorescence excited by 15 fs FEL pulses. Note the long tailed distribution with many entries at -1 and quite some high β estimates, along with the high sample variance. **(c)** Mean photon count per pixel at Jungfrau detector for for 15 fs XFEL pulse patterns (equivalent to Fig. 3.10b), with marked regions of $\langle I \rangle$. **(d)** Histograms of speckle contrast estimates for different regions of mean photon counts. Note the transition from a long-tailed distribution with large peak at $\beta = -1$ at low $\langle I \rangle$ (blue) to a more Gaussian-like distribution for higher $\langle (I) \rangle$ (red). These figures were already published in [122].

From Fig. 3.12, it is apparent that the shape of the distribution of β estimates changes with $\langle I \rangle$. In Fig. 3.12a with $\mu = 10^{-4}$, most entries are at $\beta = -1$, and a few entries are distributed over a wide range of large β values. At a slightly higher value $\mu = 3 \times 10^{-4}$, shown in Fig. 3.12b, this transmutes to a distribution consisting of peaks (caused by patterns with one two-photon value, two two-photon values, and so on). Finally, the distribution takes on a Gaussian shape, centered at β_0 for sufficiently large μ, as seen in Fig. 3.12c. Despite the differences in the distributions, the averages of the β estimates in each of the cases presented in Fig. 3.12 all have the correct value of $\langle \beta \rangle = 1$ (equal to β_0). However, this is only true when averaging over patterns with the same expectation value (approximated by the mean count) $\mu \approx \langle I \rangle$. With significant intensity fluctuations, β estimates are averaged over values sampled from a significantly different distribution. It is unlikely in that case that the $\beta \gg 1$ estimates, which are obtained in patterns with two-photon counts and very low $\langle I \rangle$, will be appropriately balanced by the $\beta = -1$ estimates obtained when there are no two-photon counts.

The observation suggests that it might not be prudent to assign equal weight to estimate β from patterns with different $\langle I \rangle$. In order to obtain a reliable speckle contrast value from datasets with varying mean intensities, it is necessary to use an appropriately weighted mean of the single pattern estimates. Therefore, we use the inverse of the expected variance as weights,

$$\bar{\beta} = \frac{\sum_{j=1}^{N_\mathrm{P}} \beta_j \sigma_{\beta,j}^{-2}}{\sum_{j=1}^{N_\mathrm{P}} \sigma_{\beta,j}^{-2}}\,, \tag{3.131}$$

with N_P denoting the number of patterns, β_j the estimated speckle contrast of the j^{th} pattern, and $\sigma_{\beta,j}^2$ the expected variance of $\beta_j(\langle I \rangle, \beta_0)$. The variance of the weighted mean speckle contrast is then given by

$$\sigma_{\bar{\beta}}^2 = \frac{\sum_{j=1}^{N_\mathrm{P}} \left(\beta_j - \bar{\beta}\right)^2 \sigma_{\beta,j}^{-4}}{\left(\sum_{j=1}^{N_\mathrm{P}} \sigma_{\beta,j}^{-2}\right)^2}\,. \tag{3.132}$$

However, to apply this weighting, we need to know the expected variance of each β_j, namely $\sigma_{\beta,j}^2$. In the following, we derive and examine schemes for evaluating weighted averages of $\beta_{1,2}$ and β_V.

Weighted mean of $\beta_{1,2}$

As derived in Appendix A.3.5, the variance $\sigma_{\beta_{1,2}}^2$ can be expressed as

$$\sigma_{\beta_{1,2}}^2(\langle I \rangle, \beta) \approx \frac{(1+\beta)(1+\beta\langle I \rangle)}{(\langle I \rangle - 1)^2 \langle I \rangle^2} \left((1+\beta)\langle I \rangle + (2 + \langle I \rangle + 3\beta\langle I \rangle)(1+\beta\langle I \rangle)^{2+\beta^{-1}}\right)\,. \tag{3.133}$$

This is plotted as a function of $\langle I \rangle$ as solid lines in Fig. 3.13a for several true values of the speckle contrast β_0. To verify this expression, also calculations were carried out on simulated data.

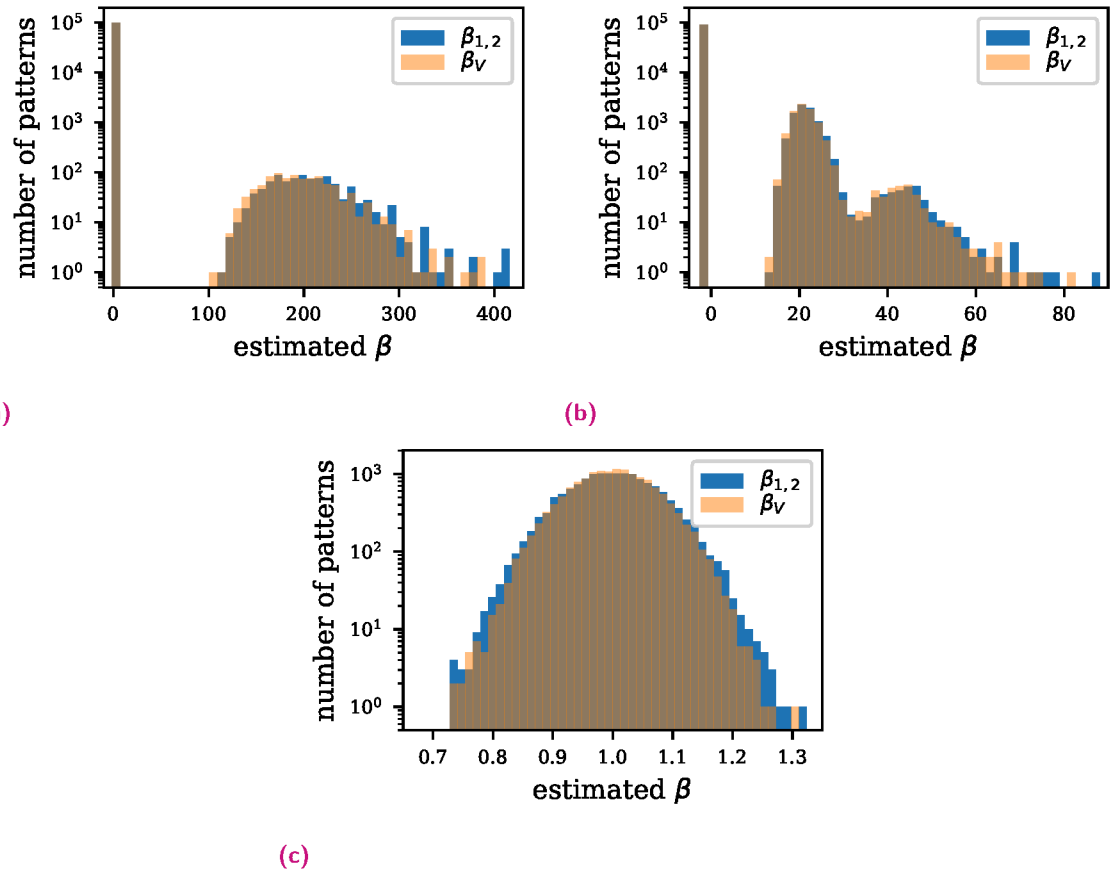

Fig. 3.12.: Histograms of single patterns speckle estimates $\beta_{1,2}$ and β_V, obtained from simulated patterns, each consisting of one million random numbers following a Bose-Einstein distribution ($\beta_0 = 1$) and with photon count expectation values of **(a)** $\mu = 10^{-4}$, **(b)** $\mu = 3 \times 10^{-4}$ and **(c)** $\mu = 3 \times 10^{-2}$. For (a) and (b) most of the entries are at $\beta = -1$ and a minority at very high values. These figures were already published in [122].

As for the simulations above, sets containing 10^6 random numbers each were generated following a negative binomial distribution, corresponding to patterns recorded with a one-megapixel detector. Groups of patterns were simulated for constant β_0 and $\langle I \rangle$, for values of $\langle I \rangle$ spanning[3] 1×10^{-5} to 1. The number of simulated patterns per group decreased[4] from 10^5 for the smallest $\langle I \rangle$ to 5000 patterns for the largest. For each pattern $\beta_{1,2}$ was calculated using Eqn. (3.129) from which sample variances were determined and plotted as dots in Fig. 3.13a. As seen in that figure, the theoretical and simulated variances $\sigma^2_{\beta_{1,2}}$ are in good agreement. Slight deviations between them can be explained by the fact that the assumed independence (see Appendix A.3.5) of the observables P_1, P_2, and $\langle I \rangle$ is slightly violated, given that there is a finite number of pixels.

Next, 5×10^5 patterns of one-megapixel size and with $\beta_0 = 1$, but now with fluctuating mean counts, were simulated. The mean counts $\langle I \rangle$ for each pattern were chosen randomly from a negative exponential distribution with the expectation value $\mathbb{E}(\langle I \rangle) = 0.01$. A histogram of these is given in Fig. 3.14a. This distribution corresponds to a SASE process [63, 103] with a single mode, for example, yielding measurements with an average of 0.01 counts per pixel per pattern and a maximum value of $\langle I \rangle = 0.1$. For each simulated pattern, $\beta_{1,2}$ was calculated using Eqn. (3.129). To examine the effectiveness of the inverse variance weighting, the patterns were divided into two subsets depending on whether $\langle I \rangle$ was smaller or larger than a particular threshold, I_{split}.

For both the low-intensity and high-intensity subsets obtained for various choices of I_{split}, the weighted mean $\bar{\beta}_{1,2}$ and its standard deviation $\sigma_{\bar{\beta}_{1,2}}$, as well as the unweighted mean $\langle \beta_{1,2} \rangle$ and its standard deviation, were calculated. The standard deviations $\sigma_{\langle \beta_{1,2} \rangle}$ of the unweighted means for the low-intensity and high-intensity subsets are plotted as a function of I_{split} as the solid orange line and the dashed orange line, respectively, in Fig. 3.14b. The inverse variance weighted standard deviations $\sigma_{\bar{\beta}_{1,2}}$ for the two subsets are plotted in Fig. 3.14c also as solid orange, and dashed orange lines.

Comparing the orange lines in Fig. 3.14b with those in Fig. 3.14c shows reductions of the standard deviations for both the low-intensity and high-intensity subsets when applying the weighting scheme. This improvement is also apparent when using the entire set of patterns, as when the threshold of the low-intensity subset is equal to the maximum value of $I_{\text{split}} = 0.1$ or (equivalently) for the high-intensity subset at $I_{\text{split}} = 0$. In this case, the weighting scheme yields a standard deviation of 4×10^{-8}, compared with 10^{-4} for the unweighted mean. It is also noted that the unweighted mean $\langle \beta_{1,2} \rangle$ of the high-intensity bin ($\langle I \rangle \geq I_{\text{split}}$, orange dashed line) becomes worse if data with a lower mean photon count than about 0.01 are included. That is, the unweighted mean $\langle \beta_{1,2} \rangle$ suffers from a higher uncertainty when all data are included compared with when the very-low intensity patterns are neglected. With inverse variance weighting, on the other hand, including all data, no matter how low the mean counts, the uncertainty of $\bar{\beta}_{1,2}$ reduces.

It may seem circular that we need β to calculate $\sigma^2_{\beta_{1,2}}$, which is then used to determine $\bar{\beta}_{1,2}$, but it turns out that exact knowledge of β is not crucial, and an initial guess can be used to determine $\bar{\beta}_{1,2}$ recursively.

[3] There is a typo in [122] claiming a range of $\langle I \rangle = [5 \times 10^{-3}, 1]$, which should be $\langle I \rangle = [1 \times 10^{-5}, 1]$.

[4] This decrease was implemented because the calculation of negative binomial variables with high μ is significantly more computational expensive and the simulations are converging much faster for higher $\langle I \rangle$.

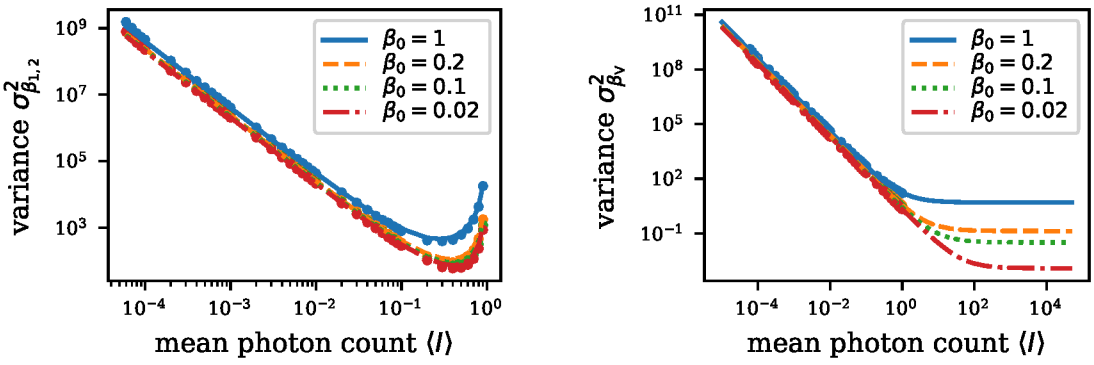

(a) (b)

Fig. 3.13.: **(a)** Variance of $\beta_{1,2}$ as a function of $\langle I \rangle$ as computed using Eqn. (3.133) (solid lines) and simulated values (dots). The variance decreases with increasing $\langle I \rangle$ for low signals and then increases as $\langle I \rangle$ approaches 1. **(b)** Variance of β_V as a function of $\langle I \rangle$ as computed using Eqn. (3.134) (solid lines) and simulated values (dots). Note that $\sigma^2_{\beta_V}$ saturates at high $\langle I \rangle$. These figures were already published in [122].

To put things into perspective, in the presented example, the standard deviation of the mean unweighted β is about 3500 times higher than that of the weighted mean, considering the entire dataset. This means that, in order to obtain a similar accuracy, 1.2×10^7 times as many patterns would be required. However, when discarding the low-photon-count data (in the present case, around 76 % of the whole dataset), the standard deviation can be reduced by a factor of 3×10^{-4}. Then the difference to the weighted case is relatively small, but still, the accuracy stays lower.

Weighted mean of β_V

An evaluation of the inverse variance-weighting of $\bar{\beta}_V$ was performed similarly to the case of $\bar{\beta}_V$ presented above. The variance of β_V, required for the weighting, is approximated by

$$\sigma^2_{\beta_V} \approx \frac{2 + 2\beta^3\langle I \rangle^2 + \beta^2\langle I \rangle(4 + 3\langle I \rangle) + \beta(2 + 4\langle I \rangle)}{\langle I \rangle^2}. \tag{3.134}$$

A detailed derivation of this equation can be found in Appendix A.3.6, and a verification of the expression is presented in Fig. 3.13b utilizing the same simulated dataset as previously used for $\sigma^2_{\beta_{1,2}}$.

Plots of the variances of estimates of the unweighted $\langle \beta_V \rangle$ as well as the inverse variance-weighted $\bar{\beta}_V$ are given in Fig. 3.14b and Fig. 3.14c, respectively. As above, the dataset was divided into high-intensity (dashed blue line) and low-intensity (solid blue line) sets. The standard deviations are quite similar to those observed for $\beta_{1,2}$.

Significant differences in the β_V and $\beta_{1,2}$ methods only become apparent for mean counts higher than about 0.1. To investigate these, a set of patterns with $\beta_0 = 1$ and a negative exponential distribution with a higher expectation value $\mathbb{E}(\langle I \rangle) = 0.2$ and a maximum of 2.0 photons per pixel have been simulated. A histogram of the mean counts per pattern is plotted in Fig. 3.14d.

The standard deviation[5] of the equal-weighted $\langle\beta_V\rangle$ is plotted in Fig. 3.14e as a function of I_{split} for the low-intensity (solid blue line) and high-intensity (dashed blue line) dataset subdivisions. Calculations were also made on this dataset using the $\beta_{1,2}$ method. The plots of the standard deviation of $\langle\beta_{1,2}\rangle$ (orange solid and orange dashed lines) show a critical behavior around $I_{split} = 1$, which is due to the definition gap of $\beta_{1,2}$ at $\mu = 1$.

The accuracy of the equal-weighted $\langle\beta_V\rangle$ decreases when we take the low $\langle I\rangle$ into account (as apparent from the blue dashed line in Fig. 3.14b and 3.14e), similar to the case of the equal-weighted $\langle\beta_{1,2}\rangle$, as discussed before. The standard deviation of the inverse variance-weighted $\bar{\beta}_V$ and $\bar{\beta}_{1,2}$ (plotted in Fig. 3.14c and 3.14f), are both showing a significant improvement as compared with the unweighted averages. While for low photon count data, the accuracy of $1/\sigma_\beta^2$-weighted $\bar{\beta}$ is almost the same for $\beta_{1,2}$ and β_V, the latter is significantly better for high photon counts.

We can state, as an intermediate conclusion, that the $1/\sigma_\beta^2$-weighted β_V approach is preferable when retrieving speckle contrast from data consisting of patterns with different mean photon counts.

3.3.2 Speckle contrast determination of K_α X-ray fluorescence

We can now apply our proposed $1/\sigma_\beta^2$-weighting of speckle contrast estimates on the experimental fluorescence data described in Section 3.2. Utilizing Eqn. (3.131) we obtain

$$\begin{aligned}
\bar{\beta}_V(3\,\text{fs}) &= -0.048 \pm 0.004\,, \\
\bar{\beta}_V(15\,\text{fs}) &= -0.073 \pm 0.003\,, \\
\bar{\beta}_{1,2}(3\,\text{fs}) &= -0.052 \pm 0.006\,, \\
\bar{\beta}_{1,2}(15\,\text{fs}) &= -0.074 \pm 0.003\,.
\end{aligned} \tag{3.135}$$

In contrast to the unweighted values in Eqn. (3.130), the values of $\bar{\beta}_V$ and $\bar{\beta}_{1,2}$ are in much better agreement. However, the estimated speckle contrast is negative now, which would imply a sub-Poissonian photon distribution which is not expected. This result can be explained by systematic errors in the photonization method used to extract photon counts from the measured detector frame, as described in Appendix B.1. In particular, the discrimination of one-photon and two-photon hits is crucial. In our case, the photonization algorithm underestimates the two-photon hits in favor of the one-photon hits, which leads to a systematic underestimation of the retrieved speckle contrast. Due to this bias, it is therefore not possible to obtain the speckle contrast absolutely. Yanwen Sun et al. [115] recently discussed such systematic errors in the estimates of speckle contrast induced by the photonization algorithms. They demonstrated that the error behaves linearly for measurements with small photon counts $\langle I\rangle \ll 1$, implying that the difference of the retrieved speckle contrast difference could be trusted. In order to estimate how well the linear behavior can be assumed, see the discussion about the β_H approximation in Appendix A.3.3, which assumes such a linear dependence of the β estimation on P_2.

[5] There is a typo in [122] calling $\sigma_{\langle\beta_V\rangle}$ 'variance' but is should read 'standard deviation' instead.

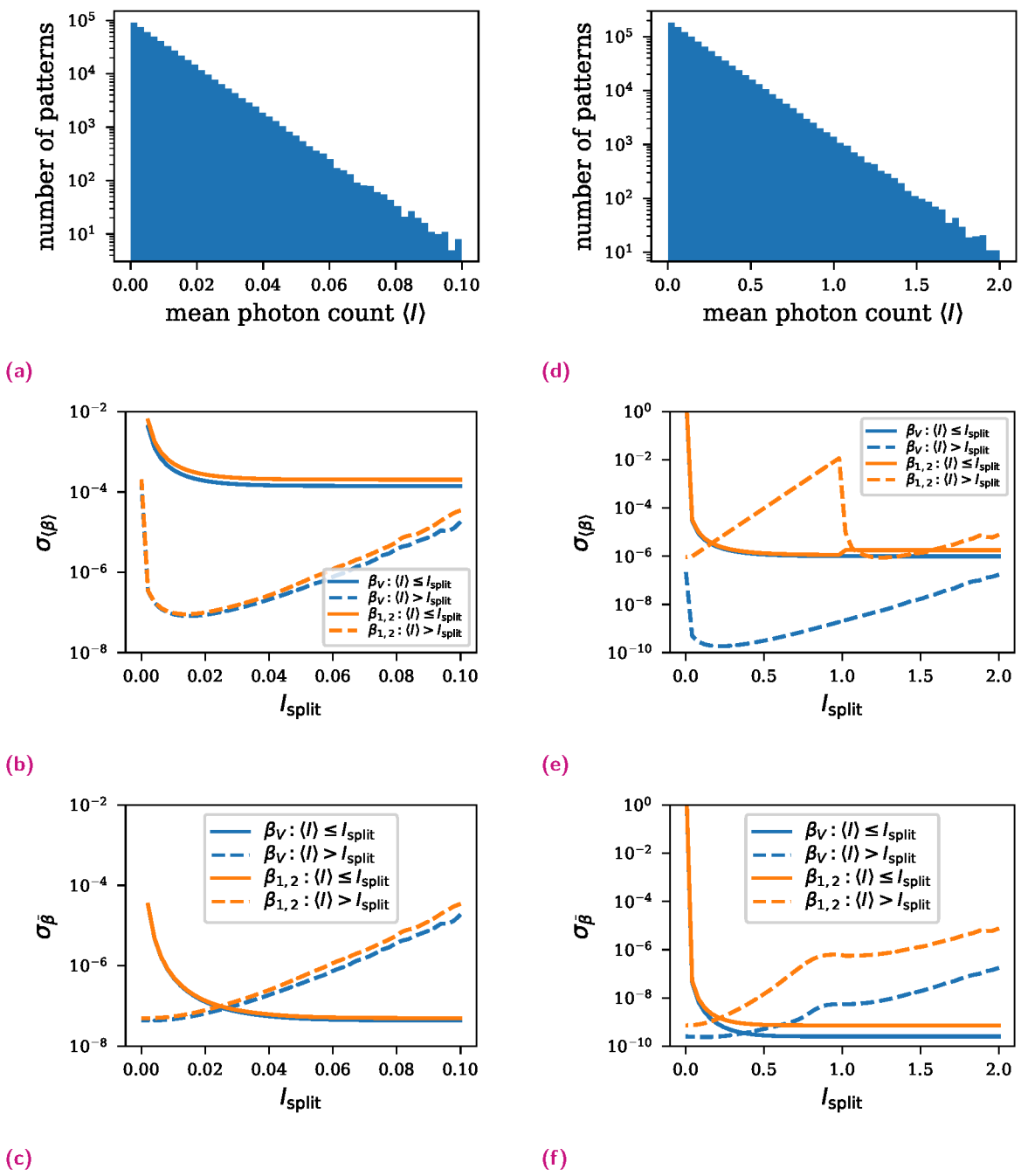

Fig. 3.14.: Effects of $1/\sigma_\beta^2$-weighting demonstrated on simulated data in which the mean counts per pattern follows negative exponential distributions with **(a)** mean $\mathbb{E}(\langle I \rangle) = 0.01$ and **(d)** $\mathbb{E}(\langle I \rangle) = 0.2$. The data were divided into two parts: one at high intensity with $\langle I \rangle > I_{\text{split}}$, and its complement with $\langle I \rangle \leq I_{\text{split}}$. **(b)** and **(e)** shows the standard deviation $\sigma_{\langle\beta\rangle}$ of the retrieved $\langle\beta\rangle$ of the two parts, using equal weighting, as a function of I_{split}. The standard deviation decreases when neglecting the patterns with very low counts, as evident in the low-intensity regime of (b). The plot of $\sigma_{\langle\beta_{1,2}\rangle}$ in (e) exhibits a sharp discontinuity at $I_{\text{split}} = 1$, which is absent for $\sigma_{\langle\beta_V\rangle}$. **(c)** and **(f)** shows the standard deviation of the retrieved $\bar{\beta}$ of the two parts, using $1/\sigma_\beta^2$-weighting. In this case the lowest standard deviation is achieved by using all patterns to estimate β. Please note, that β_V always performs better than $\beta_{1,2}$, especially in the high intensity regime, see (f). These figures were already published in [122].

Our measured data satisfies this requirement of very small mean photon counts, and thus we can report the retrieved speckle contrast difference $\Delta\bar{\beta} = \bar{\beta}(3\,\mathrm{fs}) - \bar{\beta}(15\,\mathrm{fs})$ instead of the absolute values as meaningful results,

$$\begin{aligned} \Delta\bar{\beta}_{\mathrm{V}} &= 0.025 \pm 0.005\,, \\ \Delta\bar{\beta}_{1,2} &= 0.022 \pm 0.005\,. \end{aligned} \tag{3.136}$$

The maximum expected speckle contrast difference due to the change in incident X-ray pulse duration using Eqn. (3.127) is $\Delta\beta_0 = 0.039$ ($\Delta\beta_0 = 0.034$, when considering $\beta_{\mathrm{SPS}} = 0.88$). However, as discussed in Section 3.2.1, these were the theoretical maximum limit speckle contrast calculations, and as detailed discussed in Section 3.1, there are many experimental factors that will further reduce the speckle contrast, and so too will reduce the contrast difference. Our estimated $\Delta\bar{\beta}$ is, therefore, reasonably consistent with the changes in pulse duration. More important, however, is that this measured change in speckle contrast is consistent (and implies) the interference of fluorescence photons.

4 Statistics and signal-to-noise ratio for IDI

Imaging via photon-photon correlation, also known as incoherent diffractive imaging, differs in one major aspect from coherent diffractive imaging (CDI): The 'usable signal' $|g^{(1)}(\vec{q})|^2$ is on top of an offset $g^{(2)}(\vec{q}) = 1 + \beta|g^{(1)}(\vec{q})|^2$ (recall Eqn. (2.79)). In this chapter, we will point out how this affects the signal-to-noise ratio (SNR) and discuss the implications for experiments. It should be emphasized that the implications are not limited to IDI using X-ray fluorescence but apply to all fields where intensity interferometry is used (e.g., astronomy). Most of the content in this chapter was already published in [121].

4.1 Statistics of photon-photon correlation

As discussed in Section 2.3.4, the expected photon statistics can be approximated as a negative binomial distribution

$$P_{\mathrm{NB}}(x|\mu,\beta) = \frac{(\mu\beta)^x\,\Gamma(x+\beta^{-1})}{(1+\mu\beta)^{\frac{1}{\beta}+x}x!\,\Gamma(\beta^{-1})}\,, \tag{4.137}$$

where x denotes the number of photons, μ the expectation value of x, $\beta = M^{-1}$ is the visibility factor (inverse of modes), and $\Gamma(a)$ denotes the gamma function. As a reminder, the variance of this distribution reads

$$\mathrm{Var}_{\mathrm{NB}} = \mu + \beta\mu^2\,. \tag{4.138}$$

The first summand μ is equal to the variance for a Poisson distribution (obtained when $\beta \to 0$), and therefore, we call it *Poisson noise*, while the second one $\beta\mu^2$ is equivalent to the variance of the Gamma distribution and so can be considered due to *phase noise* (recall that the random phases are leading to the exponential distribution, see Section 2.3.3) and the visibility factor.

IDI requires the correlation of measured photon counts (recall Eqn. (2.79)). The simplest way to perform this correlation is to multiply the counts of two single-pixel detectors. Initially, for the sake of simplicity, we assume that the counts of both detectors are uncorrelated. This assumption seems like a weird approximation since the correlation is our desired signal, but it allows us to get some general statements about the expected SNR. However, we need to keep this approximation in mind, and we will see some cases where this will reduce the validity of the general statements in the following discussions.
Under this assumption, the correlation follows the distribution of the product of two negative-binomial distributed random variables.

In general, the expectation value of two independent random variables X and Y is $\mathbb{E}(XY) = \mathbb{E}(X)\,\mathbb{E}(Y)$, and its variance reads [42]

$$\mathrm{Var}(XY) = \mathrm{Var}(X)\mathrm{Var}(Y) + \mathrm{Var}(X)\mathbb{E}(Y)^2 + \mathrm{Var}(Y)\mathbb{E}(X)^2\,. \tag{4.139}$$

Thus, the expectation value of the product distribution of two negative binomial distributed values (photon counts) is $\mu_{\text{NB·NB}} = \mu^2$, where μ remains the expectation value of the detected counts. The variance of this product distribution is given by

$$\mathrm{Var}_{\text{NB·NB}} = \left(\beta^2 + 2\beta\right)\mu^4 + 2\,(1+\beta)\,\mu^3 + \mu^2\,. \tag{4.140}$$

This relation describes the variance of the correlation of signals measured with two independent single-pixel detectors (for instance, the two telescopes Hanbury Brown and Twiss used to determine the diameter of stars [46, 45]) or for coincidence measurements made between two detectors out of a multiple detector array (as proposed for the *Cherenkov telescope array* [20]). On the other hand, when measurements are made using a pixelated detector, where the counts in many detector pairs are acquired simultaneously, the discrete auto-correlation $\mathrm{AC}(\vec{q})$ is given by a sum of such products. Thus, a single pixel can contribute twice to the value of $\mathrm{AC}(\vec{q})$, namely with the counts measured at $I(\vec{k})$ correlated with $I(\vec{k}+\vec{q})$ and $I(\vec{k}-\vec{q})$. These two correlations are naturally correlated, which we must consider in our analysis.

In order to investigate this effect quantitatively, we assume a set of J negative binomial distributed values $I(j)$, representing the photon counts at the pixels j. Further, for the sake of simplicity, we assume that the angular positions of these pixels are evenly spaced along a line of $\vec{k}$ positions (that corresponds to a one-dimensional array). We keep our assumption that $I(j)$ values are uncorrelated. We further assume periodic boundary conditions: $I(j+J) = I_j$, which would be precisely valid for a spherical 4π detector but is also a reasonable approach for small q values at a large detector. The auto-correlation then becomes

$$\mathrm{AC}(q) = \frac{1}{J}\sum_{j=1}^{J} I(j)I(j-q)\,. \tag{4.141}$$

Each term within this sum follows the product distribution with a variance given by Eqn. (4.140). Note that even if there is no correlation between the single multiplicands $I(j)$ (per our assumption), there may still be a covariance between the summands of Eqn. (4.141). $I(j)I(j+q)$ and $I(l)I(l+q)$ are uncorrelated if $|j-l| \neq q$; however, there will be a non-vanishing covariance for $j - l = q$. As an example, consider $q = 1$:

	I_1	I_2	I_3	$\dots$	I_J
	I_J	I_1	I_2	$\dots$	I_{J-1}
$\frac{1}{J}\sum$	$I_1 \cdot I_L$	$I_2 \cdot I_1$	$I_3 \cdot I_2$	$\dots$	$I_J \cdot I_{J-1}$

Obviously, there is a correlation between the summands $I_2 \cdot I_1$ and $I_3 \cdot I_2$, which must be considered when calculating the variance of the auto-correlation (Eqn. (4.141)).

Given that the variance of a sum of random variables is the sum of the covariances of all combinations of pairs of those variables, we obtain

$$\mathrm{Var}_{\mathrm{AC}} = \frac{1}{J}\sum_{j,l=1}^{J} \mathrm{Cov}(I(j)I(j-q), I(l)I(l-q))\,. \tag{4.142}$$

Since $\mathrm{Cov}(X,X) = \mathrm{Var}(X)$, we can write Eqn. (4.142) as

$$\mathrm{Var}_{\mathrm{AC}} = \frac{1}{J}\sum_{j=1}^{J} \mathrm{Var}(I(j)I(j-q)) + \frac{2}{J}\sum_{j=1}^{J} \mathrm{Cov}(I(j)I(j-q), I(j-q)I(j-2q))\,, \tag{4.143}$$

since the condition $j-l=q$ appears J times within the auto-correlation sum. The covariance for the random variables X and Y is given by

$$\mathrm{Cov}(X,Y) = \mathbb{E}(XY) - \mathbb{E}(X)\mathbb{E}(Y)\,, \tag{4.144}$$

and therefore, the second term of Eqn. (4.143) can be written as

$$\mathbb{E}(I(j))\mathbb{E}(I^2(j-q))\mathbb{E}(I(j-2q)) - \mathbb{E}((I(j)I(j-q))\mathbb{E}(I(j-q)I(j-2q))\,. \tag{4.145}$$

With $\mathbb{E}(I(j)) = \mathbb{E}(I(j-2q)) = \mu$ and $\mathbb{E}((I(j)I(j-q)) = \mathbb{E}(I(j-q)I(j-2q)) = \mu^2$, we still need to calculate $\mathbb{E}(I^2(j-q))\mathbb{E}(I(j-2q))$. That is the expectation value of a squared negative-binomial distributed variable[1] given by

$$\mathbb{E}(X_{\mathrm{NB}}^2) = \sum_{x=0}^{\infty} x^2 P_{\mathrm{NB}}(x|,\mu,\beta) = \mu + \mu^2 + \beta\mu^2\,. \tag{4.146}$$

Therefore the last sum in Eqn. (4.143) equals

$$\frac{2}{J}\sum_{j=1}^{J} \mathrm{Cov}(I(j)I(j-q), I(j-q)I(j-2q)) = \frac{1}{J}2(\beta\mu^4 + \mu^3)\,. \tag{4.147}$$

For now, we ignore the factor $1/J$ since we want to have our term without dependence on the number of detectors (pixels) involved so that Eqn. (4.143) evaluates to

$$\mathrm{Var}_{\mathrm{AC}} = (\beta^2 + 4\beta)\mu^4 + (4+2\beta)\mu^3 + \mu^2\,. \tag{4.148}$$

Be aware that this equation can only be considered as an approximation due to the following points. First, as already mentioned, the assumption that the measured photon counts are uncorrelated contradicts the fact that we want to measure a signal by exploiting the photon-photon correlations. However, it will turn out that this approximation is quite good for 'sparse' $|g^{(1)}|$ signals. Second, the assumption of periodic boundary conditions in the derivation of Eqn. (4.147) is a good approximation for detectors with many pixels when looking at values with many $\vec{q}$ realizations but is getting worse for auto-correlations with only a few contributions. That introduces a $\vec{q}$ dependency of the SNR, illustrated in Appendix A.4.3.

[1] Please note: At this point, the fact that the photons are only approximately expected to be negative-binomial distributed might introduce an extra inaccuracy; see discussion in Appendix A.2.1.

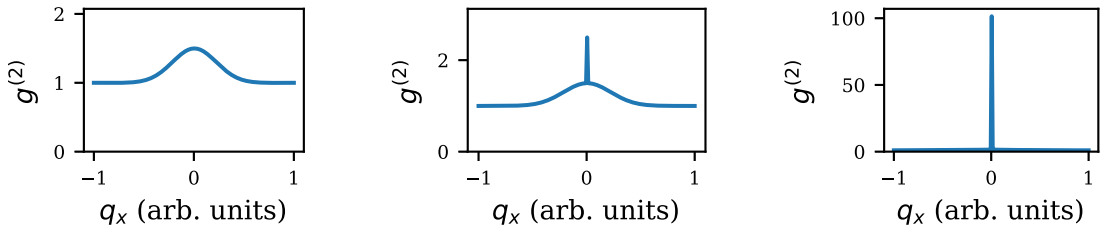

Fig. 4.1.: Demonstration of the $g^{(2)}(0)$ peak with finite expected photon counts. Cut through the $g^{(2)}(q_x, q_y = 0)$ of a simulated 2D Gaussian emitter distribution, with the visibility factor $\beta = 0.5$ (for details about the simulation see Appendix A.4.2). **(a)** Classical limit $\mu \to \infty$, here $g^{(2)}(0) = 1 + \beta$. **(b)** $\mu = 1$ with $g^{(2)}(0) = 2 + \beta$. **(c)** $\mu = 0.01$ with $g^{(2)}(0) = 101 + \beta$.

Also, the offset term, where, besides the effect of Eqn. (4.147), no covariance is expected can not be assumed as totally uncorrelated, which is also demonstrated in Appendix A.4.3. This leads to the effect that increasing the number of pixels within one frame is not equivalent to collecting more frames.

4.1.1 Annotation: statistics of $g^{(2)}(0)$

The previous analysis is only valid for the correlation between different pixels and can not be applied to the zero-frequency component $g^{(2)}(0)$. The statistic of $g^{(2)}(0)$ differs from the other values since the assumption of two independent photon counts is not even remotely correct here. For example, the expectation value is given as

$$\mathbb{E}\left(g^{(2)}(0)\right) = \frac{1}{\mu^2}\sum_{x=0}^{\infty} P_{\mathrm{NB}}(x|\mu,\beta)x^2 = \frac{1}{\mu} + 1 + \beta\,. \tag{4.149}$$

In the limit of large photon counts, we obtain the expected value $\lim_{\mu\to\infty} g^{(2)}(0) = 1 + \beta$. However, for low photon counts, the $1/\mu$ term becomes dominant, and thus we obtain pretty high values for $g^{(2)}(0)$. The peak at $q = 0$ for finite μ is illustrated in Fig. 4.1, where the cut through the $g^{(2)}$ signal of a simulated 2D Gaussian emitter distribution is plotted for different expected photon counts. The dependence of the $g^{(2)}(0)$ value on the photon count expectation value renders this a cumbersome quantity for experiments, where the mean photon count fluctuates from measurement to measurement. Because of this, we will ignore the $\vec{q} = 0$ pixels in our simulations and evaluations of experimental data. When speaking of experiments with pixelated array detectors, charge sharing causes adjacent pixels to be also affected by this effect. For the sake of completeness, the variance is given as

$$\mathrm{Var}\left(g^{(2)}(0)\right) = \left(6\beta^3 + 10\beta^2 + 4\beta\right)\mu^4 + \left(12\beta^2 + 16\beta + 4\right)\mu^3 + (7\beta + 6)\,\mu^2 + \mu\,, \tag{4.150}$$

which is significantly larger than for the $\vec{q} \neq 0$ values (recall Eqn. (4.148)), especially for small μ.

4.1.2 Excursus: statistics for intensity fluctuation correlation imaging

The variance can be lowered, and therefore the SNR improved if the mean photon count $\langle I \rangle$ can be considered constant. That is certainly not the case when investigating X-ray fluorescence at XFELs, as discussed earlier (recall the histograms shown in Fig. 3.10); however, this can be assumed when observing most astronomical objects (e.g., stars) as it was the case for Hanbury Brown and Twiss [124]. The idea is that the mean photon count is known to be sufficiently precise that we can state $\langle I \rangle \to \mathbb{E}(I) = \mu$. We now alter Eqn. (2.76) to

$$\begin{aligned} \mathrm{AC}_{\mathrm{IFCI}}(\vec{q}) &= \left\langle \Big(I(\vec{k}) - \mu\Big)\Big(I(\vec{k}+\vec{q}) - \mu\Big) \right\rangle_{\vec{k}} \\ &= \left\langle \Delta I(\vec{k}) \Delta I(\vec{k}+\vec{q}) \right\rangle_{\vec{k}} \\ &= \langle I(\vec{k}) I(\vec{k}+\vec{q}) \rangle_{\vec{k}} - \mu^2 = \left| g^{(1)}(\vec{q}) \right|^2 , \end{aligned} \tag{4.151}$$

and obtain the *usable signal* without offset. The expectation value becomes $\mathbb{E}(\Delta I) = 0$, and the variance stays the same as in Eqn. (4.138) $\mathrm{Var}(\Delta I) = \mu + \beta\mu^2$. However, the variance of the product $\Delta I(\vec{k}) \Delta I(\vec{k}+\vec{q})$ (recall Eqn. (4.139)) now becomes

$$\mathrm{Var}_{\Delta I \Delta I} = \beta^2 \mu^4 + 2\beta\mu^3 + \mu^2 , \tag{4.152}$$

which is less than the variance given in Eqn. (4.140), and thus, we can expect a better SNR for *intensity fluctuation correlation imaging (IFCI)* than for IDI. We can explain this effect with the reduction in uncertainty since we now assume that we have exact knowledge of μ. However note, that the effects we will discuss in the following still qualitatively apply to IFCI since they originate from the μ^4, μ^3, and μ^2 contributions to the variance, which are still present in IFCI, only differently weighted.

4.2 Signal-to-noise ratio

The signal-to-noise ratio (SNR) can be defined as the desired signal divided by the standard deviation of the measured signal. For IDI, this signal (the 'useable signal', as defined in Section 2.5.1) is

$$\mathrm{Sig} = \left| G^{(1)}(\vec{q}) \right|^2 = \mu^2 \left| \frac{\mathfrak{F}\left[\rho(\vec{r})\right](\vec{q})}{\mathfrak{F}\left[\rho(\vec{r})\right](0)} \right|^2 . \tag{4.153}$$

This is different from CDI, where the signal scales linearly with μ. We use the variance from Eqn. (4.148) and obtain the SNR as

$$\mathrm{SNR} = \frac{\mathrm{Sig}(\vec{q},\mu)\beta\sqrt{N_{\mathrm{P}}}\sqrt{C(\vec{q})}}{\sqrt{(\beta^2+4\beta)\mu^4 + (4+2\beta)\mu^3 + \mu^2}} , \tag{4.154}$$

where N_{P} denotes the number of averaged patterns, and $C(\vec{q})$ is the multiplicity equal to the number of pixel pairs with the same wave-vector difference $\vec{q}$.

For the discussions within this chapter, it is favorable to use the (equivalent) notation of modes $M = \beta^{-1}$ instead of the visibility factor, which turns Eqn. (4.154) into

$$\mathrm{SNR} = \frac{\mathrm{Sig}(\vec{q},\mu)\sqrt{N_\mathrm{P}}\sqrt{C(\vec{q})}}{M\sqrt{\frac{1+4M}{M^2}\mu^4 + 2\frac{1+2M}{M}\mu^3 + \mu^2}}\,. \tag{4.155}$$

One should note that increasing $C(\vec{q})$ does not have the same effect on the SNR as increasing N_P, and this term saturates at some point. Even if we consider a detector covering 4π with infinite sampling, a single pattern will still suffer from 'phase noise' since the assumption of independent photon counts forming the background can not be maintained. A simple analytic example is discussed in Appendix A.4.3.

In the following, we examine different kinds of emitting (fluorescing) samples requiring different simulation methods. See Appendix A.4.1 and A.4.2 for details. The detector arrangement also differs, according to sampling requirements, placing the different cases on quite different scales and making direct comparisons somewhat artificial (for example, imaging a crystal versus a single non-periodic object). Therefore, we concentrate on separately studying the dependence of the SNR on the mean photon count in Section 4.2.1, the number of modes (inverse visibility factor) in Section 4.2.2, and object shape in Section 4.2.3 to gain an understanding of how to best design experiments.

Simple cubic 3D crystal

The specimen we will discuss in this chapter in the most detail is a three-dimensional crystal with $n \times n \times n = N_\mathrm{uc}$ simple cubic unit-cells. Hereby, we assume that each unit-cell consists of one cluster of single photon emitters that are so close to each other that they are indistinguishable and can be treated as one (thermal light) emitter[2]. The crystal then consists of $N_\mathrm{E} = N_\mathrm{uc} = n^3$ emitters, each isotropically emitting on average N_γ photons per mode and pattern. The expected mean photon count per pixel is therefore given by

$$\mu = \Omega N_\mathrm{E} N_\gamma M\,, \tag{4.156}$$

where $4\pi\Omega$ is the solid angle of a pixel. For the sake of simplicity, we assume, within this chapter, that the solid angle is constant for each pixel. The (non-normalized) auto-correlation signal

$$G^{(2)}(\vec{q}) = \langle\langle I_P(\vec{k})\, I_P(\vec{k}+\vec{q})\rangle_{\vec{k}}\rangle_P\,, \tag{4.157}$$

obtained from the measured photon counts of the crystal consists of a uniform background with strong peaks at the reciprocal lattice points (Bragg peaks), as shown in Fig. 4.2.

[2] As discussed in Section 2.5.2, assuming there are a sufficient number of emitters, the nature of the emission can be approximated as thermal light sources.

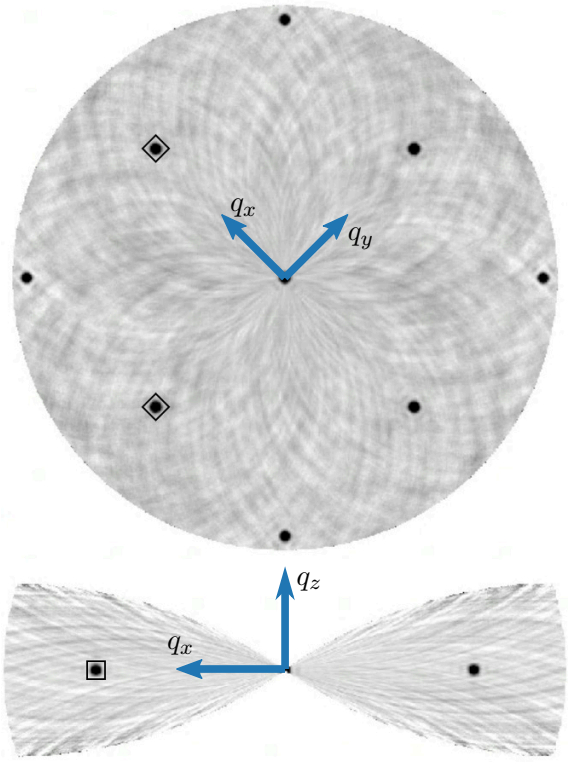

Fig. 4.2.: Slices through the $G^{(2)}$-space from IDI simulation of a simple cubic crystal with $21 \times 21 \times 21$ unit-cells. Integration boundaries for the signal are indicated as squares around the peaks. This figure was already published in [121].

The $|G^{(1)}|^2$-map that is extracted from the autocorrelation can be written as

$$\left|G^{(1)}(\vec{q}, N_\mathrm{E})\right|^2 \propto \left| \prod_{j=x,y,z} \left(\frac{1}{\sqrt{2}} \frac{e^{i\sqrt[3]{N_\mathrm{E}} a q_j} - 1}{e^{i a q_j} - 1} \right) \right|^2 , \tag{4.158}$$

where a is the lattice constant. We then define the signal that is extracted from such a map as the values integrated over Bragg peaks, which in the limit of large cubic crystals is proportional to the number of emitters

$$\lim_{N_\mathrm{E}\to\infty} \int_{-\frac{\pi}{a}}^{\frac{\pi}{a}} \left|G^{(1)}(\vec{q}, N_\mathrm{E})\right|^2 \, dq_x \, dq_y \, dq_z \propto N_\mathrm{E} \, . \tag{4.159}$$

This yields a signal as described by

$$\mathrm{Sig}_\mathrm{Crystal} = N_\mathrm{E} N_\gamma^2 \Omega^2 M^2 = \frac{\mu}{N_\mathrm{E}} \, . \tag{4.160}$$

And thus, the SNR is

$$\mathrm{SNR}_\mathrm{Crystal} = \frac{\mu^2 \sqrt{C(\vec{q})} \sqrt{N_\mathrm{P}}}{N_\mathrm{E} M \sqrt{\frac{1+4M}{M^2}\mu^4 + 2\frac{1+2M}{M}\mu^3 + \mu^2}} \, . \tag{4.161}$$

A word of caution about Eqn. (4.160) is warranted since it indicates that pixels of larger solid angles should result in higher SNR. However, a bigger Ω most likely implies a lower number of total pixels and, thus, a smaller $C(\vec{q})$. Additionally, as previously discussed in Section 3.1.5, an increased pixel size will lead to a loss of visibility due to insufficient speckle sampling.

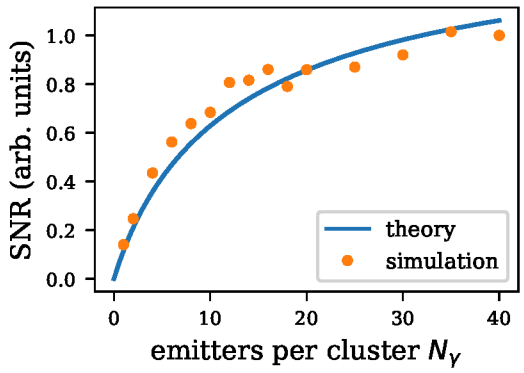

Fig. 4.3.: SNR for a simple cubic $21 \times 21 \times 21$ crystal as function of emitter per cluster within unit-cell. The emitters within each cluster are are not spatially resolved, since they were placed at a common location. This figure was already published in [121].

4.2.1 SNR as a function of the mean photon count

To test the SNR expression in Eqn. (4.161), we first investigate the dependence of the SNR of simulated data on μ, or more precisely, on N_γ (the number of photons emitted by a cluster of non-distinguishable emitters per mode). Simulations with three-dimensional crystals have been performed from which two slices through $G^{(2)}(\vec{q})$ are shown in Fig. 4.2. In Fig. 4.3, the SNR of the two Bragg peaks highlighted in Fig. 4.2 is plotted as a function of N_γ, which was changed by adding more emitters to the cluster in each unit-cell, keeping the size of the crystal constant. It is important to note that the individual emitters within each cluster are not resolvable, which is ensured by adding the extra emitters to exactly the same location within the unit-cell. This is effectively the same as increasing the intensity (emitted number of photons) of each emitter. We observe that the SNR increases with increasing intensity but appears to asymptote to a certain value. This is because, for a small number of photons, Poisson noise is dominant yielding SNR $\propto N_\gamma$, whereas, for a sufficiently large number of photons per pixel, phase noise becomes important, which yields a constant SNR for a fixed number of patterns and modes. This can also be seen in Eqn. (4.161) where the low and high-intensity levels are

$$\begin{aligned} \lim_{N_\gamma \to 0} \mathrm{Sig}_{\mathrm{Crystal}} &= \frac{\mu \sqrt{N_\mathrm{P} C(\vec{q})}}{N_\mathrm{E} M}\,, \text{ and} \\ \lim_{N_\gamma \to \infty} \mathrm{Sig}_{\mathrm{Crystal}} &= \frac{\sqrt{N_\mathrm{P} C(\vec{q})}}{N_\mathrm{E} \sqrt{1+4M}}\,. \end{aligned} \tag{4.162}$$

To further investigate the SNR as a function of μ simulations were performed, where the detected counts are obtained from emitters arranged as two-dimensional (non-crystalline) objects. The used objects have a less distinguishable signal than the Bragg peaks of crystals, which makes it more difficult to separate the (usable) signal from the offset. Therefore the $G^{(2)}(\vec{q})$ was fitted to the ground truth $|g^{(1)}(\vec{q})|^2$ via

$$G^{(2)}(\vec{q}) = O + S \left| g^{(1)}(\vec{q}) \right|^2 + \epsilon(\vec{q})\,, \tag{4.163}$$

where the fit parameter S can be interpreted as the signal, O as the offset, and $\epsilon(\vec{q})$ as the noise. A more detailed description of the simulations can be found in Appendix A.4.2. In Fig. 4.4a, the SNR is plotted for four different objects: two very sparse ones, one crystal-like object, and one *dense* object with spatial frequencies giving a continuously filled Fourier-space.

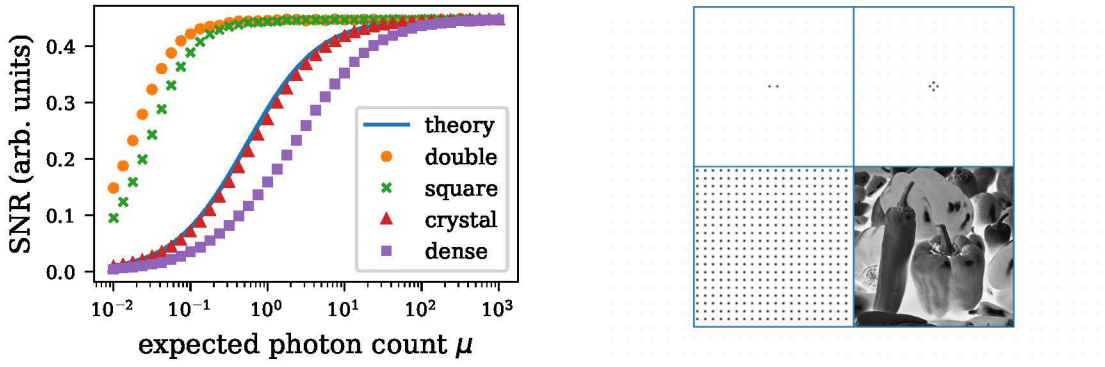

(a) (b)

Fig. 4.4.: SNR dependence on shape of the object. **(a)** SNR as function of photon counts per pixel normalized such that they all saturate at the same level. **(b)** Emitter densities: top left: *double*; top right: *square*; bottom left: *crystal*; bottom right: *dense*. These figures were already published in [121].

The plots of these SNRs were scaled to asymptote to unity for comparison. This also demonstrates the limits of the here presented theory with its assumption of uncorrelated values following a negative binomial distribution, applied to the case of correlated values with structural information. As can be seen in the figure, the presented theory fits quite well for objects with sparsely populated $|g^{(1)}(\vec{q})|^2$ signals (e.g., for the *crystal* object in Fig. 4.4a) since most of the detected counts are indeed uncorrelated in such objects. It is possible to fit the single mode variance for the limit of dense and unstructured objects as

$$\mathrm{Var}_{\mathrm{DenseObj},M=1} = \mu^4 + 6\mu^3 + \mu^2 \,. \tag{4.164}$$

Because of the apparent strong dependency of the variance of $G^{(2)}$ on the characteristics of the object, as seen by the discrepancies of Eqn. (4.155) to the simulations in Fig. 4.4a, we keep the expression of the variance of Eqn. (4.148) for further discussions, but we need to keep these limits in mind when fitting this model to the simulated data.

4.2.2 SNR as a function of modes (visibility)

Here we discuss the dependence of Eqn. (4.155) on the visibility factor. For this purpose, we use the notation of modes $M = \beta^{-1}$. Therefore, simulations of 3D and 2D emitter distributions are utilized again. For this discussion, we make the assumption that the expected photon counts per pixel are proportional to the number of modes, or in other words, that each mode has the same expected number of counts μ_0 so that the total expected counts per pattern is $\mu = M\mu_0$. Studying the SNR behavior under this assumption makes sense since intensity (photon counts) can often be traded for visibility.

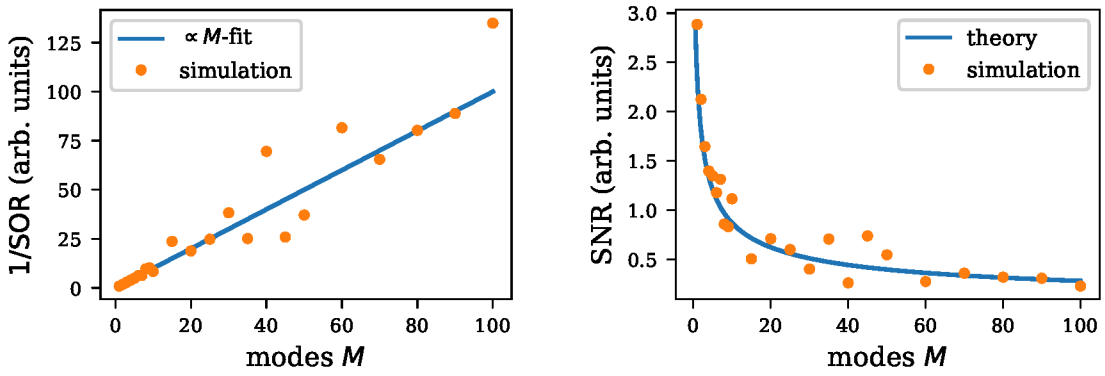

(a) (b)

Fig. 4.5.: Simulation of a $15 \times 15 \times 15$ unit-cell crystal under variation of modes. Since $\mu_0 = 1.35$ is was to be constant, the mean counts per pixel and pattern is proportional to the number of modes $\mu \propto M$. **(a)** Inverse of the SOR with $\propto M$-fit, to illustrate the $\beta = 1/M$ behavior. **(b)** SNR as a function of modes. These figures were already published in [121].

For example, as discussed in Section 3.1.1, doubling the excitation time can double the total number of photons per pixel at the cost of twice the number of modes. Under this assumption, the SNR then follows the form

$$\mathrm{SNR} = \frac{\left|g^{(1)}(\vec{q})\right|^2 \mu_0^2 \sqrt{C(\vec{q})}\sqrt{N_\mathrm{P}}}{\sqrt{(1+4M)\mu_0^4 + (2+4M)\mu_0^3 + \mu_0^2}}\,. \tag{4.165}$$

As a first example, we consider a simulation of a 3D crystal with $N_\mathrm{E} = 15 \times 15 \times 15$ unit-cells, each with one emitter. The simulation was performed in a similar way as described in the previous section, with a mean count per mode and pixel of $\mu_0 = 1.35$. The reduction of the visibility $\beta = M^{-1}$ with increased modes, according to Eqn. (2.79) can be seen in the plot of the inverted *signal-to-offset ratio (SOR)* in Fig. 4.5a. The SNR obtained in the simulation is plotted in Fig. 4.5b and found to scale with the number of modes in accordance with the expression in Eqn. (4.165).

The influence of μ_0 on the mode-dependent SNR was investigated using simulations of the 2D 'dense' object from Fig. 4.4b. The variance is plotted in Fig. 4.6a and 4.6c as a function of the number of modes, M, for $\mu_0 = 0.01$ and $\mu_0 = 1$. The corresponding plots of the SNR as a function of M are shown in Fig. 4.6b and 4.6d, together with the analytic prediction from Eqn. (4.165).

We can see from Fig. 4.6 that the SNR declines much slower with respect to M for $\mu_0 = 0.01$ than for $\mu_0 = 1$. In the limit of very low μ_0, the dependence of the SNR on M becomes negligible:

$$\lim_{\mu_0 \to 0} \frac{\partial}{\partial M} \mathrm{SNR}_{\mu_0}(M) = 0\,. \tag{4.166}$$

A negligible dependence of the SNR on the number of modes in the limit of very low μ_0 (where the contribution of Poisson-noise greatly exceeds the phase-noise) was already described by Hanbury Brown and Twiss when they stated '[...] the SNR is independent of changes in the optical bandwidth, [...]' [45]. Similar statements can be found in [19, 20].

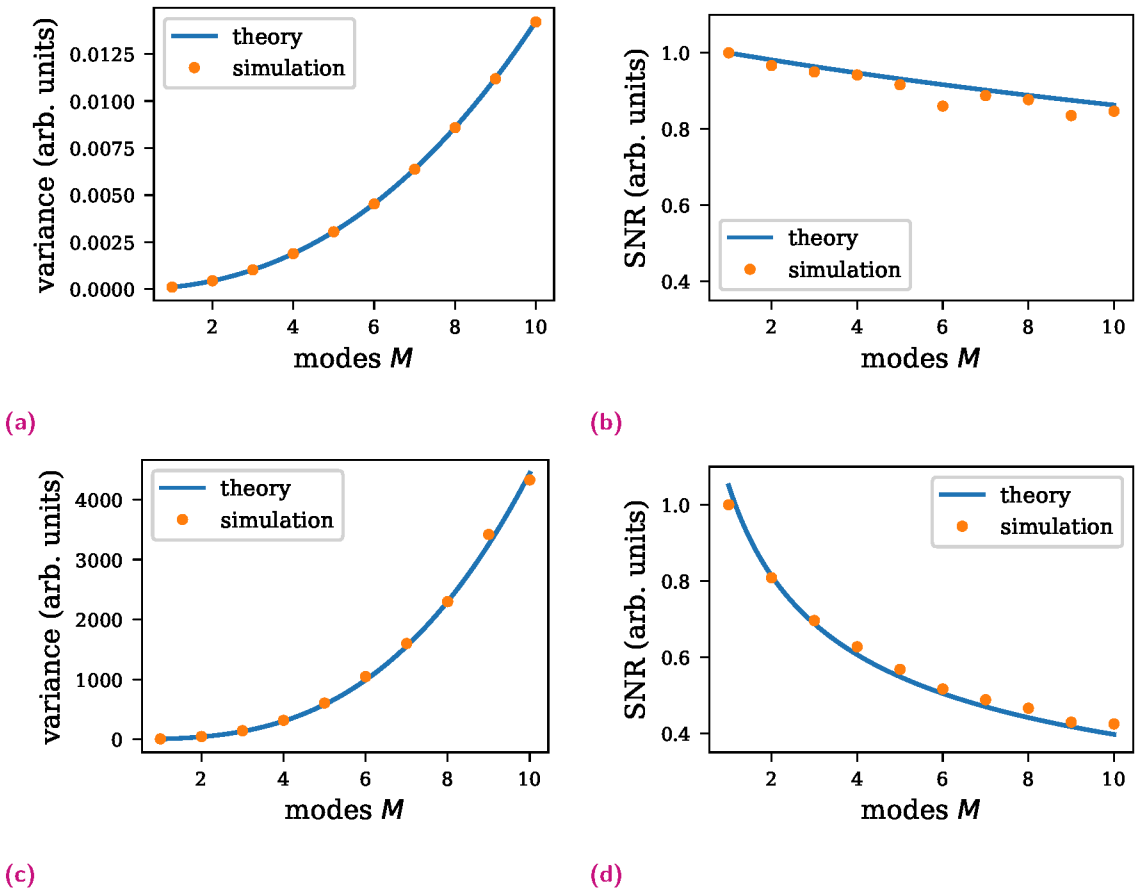

Fig. 4.6.: $G^{(2)}$-variance and SNR of the *dense* object (see Fig. 4.4b) as a function of modes. **(a)** and **(b)** Variance and SNR for $\mu_0 = 0.01$. **(c)** and **(d)** Variance and SNR for $\mu_0 = 1$. These figures were already published in [121].

Roughly speaking, a slight increase of μ (by increasing M) leads to less Poisson noise, while phase noise is still negligible, and therefore the higher μ compensates for the weaker visibility caused by the larger number of modes. In the limit of high intensity per mode, on the other hand, we obtain

$$\lim_{\mu_0 \to \infty} \mathrm{SNR}_{\mu_0}(M) \propto \frac{1}{\sqrt{1+4M}}\,, \tag{4.167}$$

and therefore, it is expected that under such circumstances, an increase in the number of modes will be significantly detrimental to the SNR. We can conclude that trading higher photon counts proportionally to a higher number of modes can never be beneficial for the SNR.

4.2.3 Dependence of the SNR on the size and complexity of the emitter distribution

In Section 4.2.1, we saw that the shape of the emitting object has a significant influence on the SNR of $G^{(2)}(\vec{q})$. Here we return to the 3D crystal with $n \times n \times n$ unit-cells with one emitter each, which yields a number of $N_{\text{uc}} = n^3$ emitters. Here, we examine how the SNR scales with the overall size of the crystal. Therefore we define the proportionality constant $\alpha = \Omega N_\gamma M$, in an analogous fashion to μ_0 in the previous section so that $\mu = \alpha N_{\text{uc}}$. α can be interpreted as the expected number of counts generated per emitter. With this, we can rewrite the SNR of Eqn. (4.161) as

$$\text{SNR}_{\text{Crystal}}(N_{\text{uc}}, \alpha) = \frac{\alpha\sqrt{C(\vec{q})N_{\text{P}}}}{M\sqrt{\frac{1+4M}{M^2}\alpha^2 N_{\text{uc}}^2 + \frac{2+4M}{M}\alpha N_{\text{uc}} + 1}}\,. \tag{4.168}$$

In Fig. 4.7, the SNR is plotted as a function of the crystal size (number of unit-cells) N_{uc} for three different 'emitter efficiencies' α, all for the case of a single mode $M = 1$. On a first view somewhat unintuitively, bigger crystals give a lower SNR. In the limit of large α the SNR behaves as $1/N_{\text{uc}}$, as indicated in Fig. 4.7b, where the reciprocal of the SNR is plotted against N_{uc}. However, the SNR becomes less dependent on N_{uc}, resulting in a flatter SNR curve for smaller α. This might seem to be an improvement over larger α at first glance; however, lower α also gives fewer expected counts μ, which ultimately results in a lower SNR. As discussed in Section 4.2.1, a greater α generally leads to a better SNR. However, as mentioned earlier, increasing α by increasing Ω alone would result in a reduction of contrast; thus, this is not a reasonable option.

In conventional crystallography, which makes use of coherent scattering from the crystal, larger crystals clearly produce higher SNR than small ones. In that case, the SNR is (in the ideal case) proportional to the square root of the number of photons diffracted per Bragg-peak, which by an equivalent analysis to Eqn. (4.158) is proportional to $\sqrt{N_{\text{uc}}}$ (assuming scattering by the emitting atom/cluster). Eqn. (4.168) and the simulations of Fig. 4.7 show the opposite behavior in IDI. Even though we have assumed perfect conditions (i.e., $M = 1$) in the simulations, there are at least two other factors in favor of choosing smaller crystals in a real experiment. First, the speckle sampling, as detailed discussed in Section 3.1.5, and second the effects of the finite speed of light, as discussed in Section 3.1.2. The implication of this crystal discussion is that signal amplification in IDI by using crystals is not beneficial, and therefore single-molecule imaging gives the best possible SNR.

The reason for the diminishing ability to image larger objects by IDI is due to the fact that as the object gets larger and more complex, the number of intensity-intensity products that do not arise in a correlated signal grows at a greater rate. This is apparent since as

$$\left|\frac{\mathfrak{F}\left[\rho(\vec{r})\right](\vec{q})}{\mathfrak{F}\left[\rho(\vec{r})\right](0)}\right|^2 = \left|g^{(1)}(\vec{q})\right|^2 \leq 1 \,\Big|\, \forall \vec{q} \neq 0\,, \tag{4.169}$$

the offset always exceeds or is at least as large as the usable signal for any $\vec{q} \neq 0$.

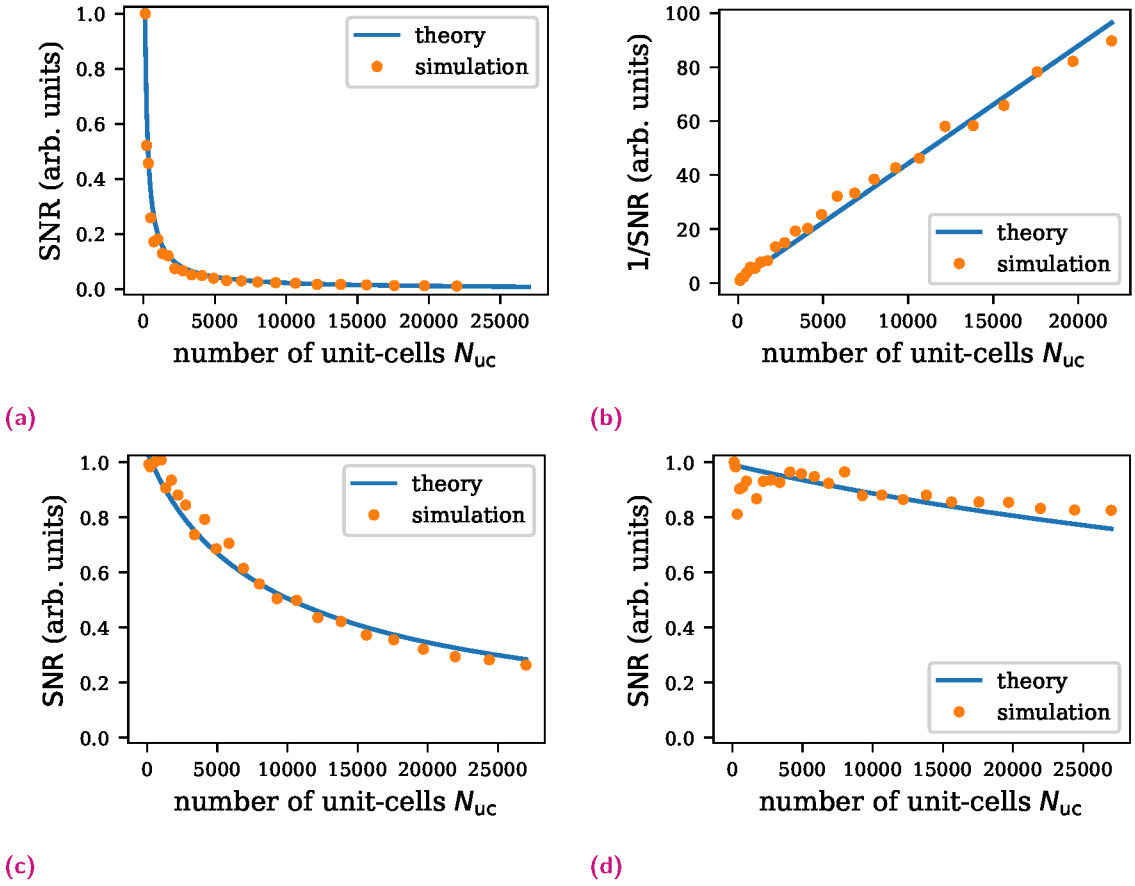

Fig. 4.7.: SNR as a function of crystal size (number of unit-cells with one emitter per unit-cell). **(a)** $\alpha = 4 \times 10^{-3}$. **(b)** Inverse of (a) to demonstrate SNR $\propto 1/N_{uc}$ behavior. **(c)** $\alpha = 4 \times 10^{-5}$. **(d)** $\alpha = 4 \times 10^{-6}$. These figures were already published in [121].

Since the distribution of emitters $\rho(\vec{r})$ is always real and positive, as the object becomes larger $|g^{(1)}|$ generally becomes smaller at any given $\vec{q}$ as the spectral power is distributed into more 'channels'. This is the case if the additional emitters added to a structure are resolvable. Those emitters added close to others (such as considered in the single clusters of emitters in the crystal, discussed in Section 4.2.1) will tend to not reduce $|g^{(1)}|$ at $\vec{q} \neq 0$.

To investigate the proposition that more 'complicated' objects have lower SNR, IDI simulations were carried out of patterns of non-periodic objects constructed in such way to give a Fourier spectrum $g^{(1)}(\vec{q})$ consisting of discrete narrow Gaussian-shaped peaks equally spaced in a ring at a particular reciprocal distance q_1, as shown in Fig. 4.8.

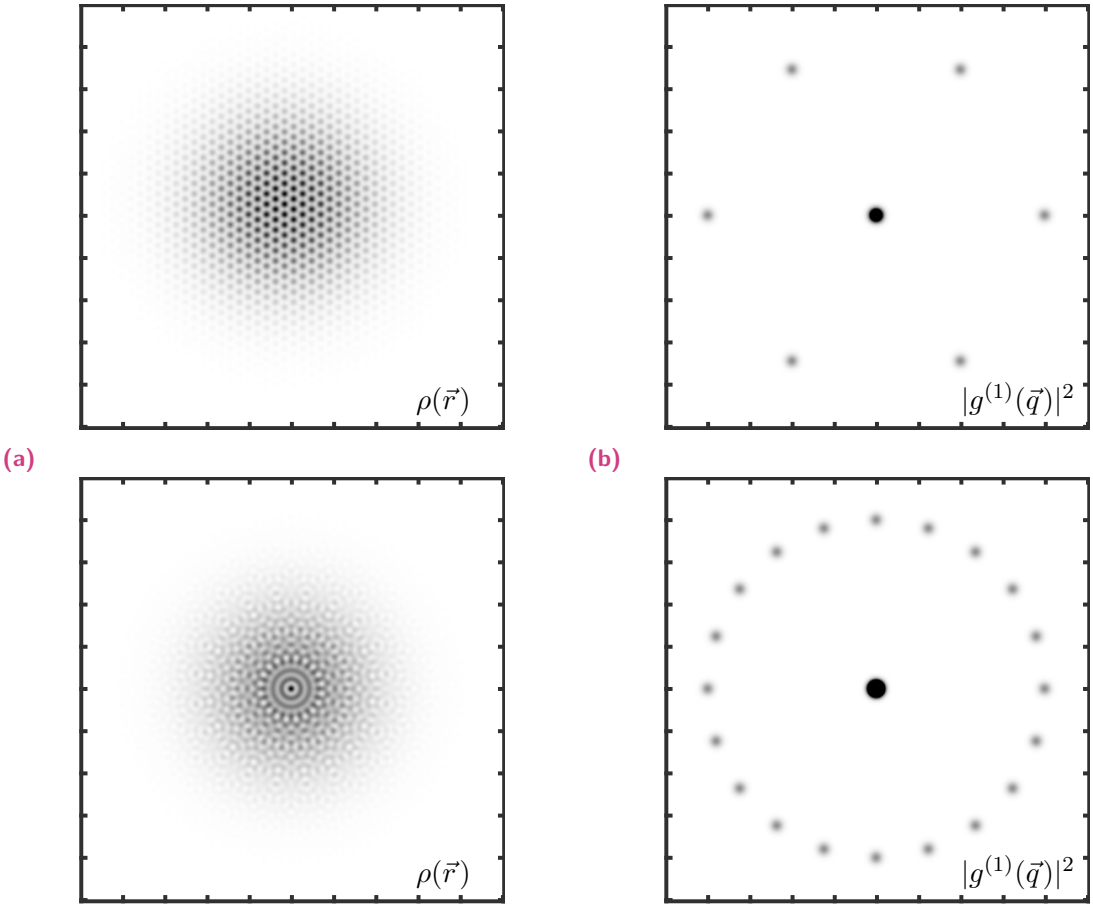

Fig. 4.8.: Object with parameterized complexity c. **(a)** Emitter density ($\rho(\vec{r})$) for $c = 3$. **(b)** Corresponding $|g^{(1)}(\vec{q})|^2$ signal for (a). **(c)** Emitter density for $c = 10$. **(d)** Corresponding $|g^{(1)}(\vec{q})|^2$ signal for (c). As signal for the discussions the integrated value of one of the outer Gaussians in $|g^{(2)}|(\vec{q})$-space was used. These figures were already published in [121].

The complexity of the object is set by the number of Fourier frequencies that follows from the number of Gaussian peaks (see Fig. 4.8b and 4.8d), without changing the resolution or overall or overall shape of the object in real space (see Fig. 4.8a and 4.8c). The object is parameterized by the number of frequency components in the ring at q_1, given by $2c$, ensuring a centrosymmetric transform to maintain a real and positive realspace emitter density. The number of photons per *complexity* and per pixel is specified as $\alpha_c = \Omega N_\gamma M$, such that when α_c is constant, the expected count per pixel is proportional to c. We compute the SNR based upon obtaining the signal of the integrated value of $g^{(2)}(\vec{q}) - 1 = |g^{(1)}(\vec{q})|^2$ of any of the (non-central) peaks. Since the strength of the peaks does not change with c, we assume the signal to be Sig $\propto \alpha_c^2$. With the mean counts per pixel $\mu = \alpha_c c$, we expect the SNR scales as

$$\mathrm{SNR}(c, \alpha_c) \propto \frac{\alpha_c \sqrt{C(\vec{q}) N_\mathrm{P}}}{M \sqrt{\frac{1+4M}{M^2}\alpha_c^2 c^4 + \frac{2+4M}{M}\alpha_c c^3 + c^2}}\,. \tag{4.170}$$

The SNR obtained from the simulations based on the parameterized object is plotted as a function of the complexity parameter c in Fig. 4.9.

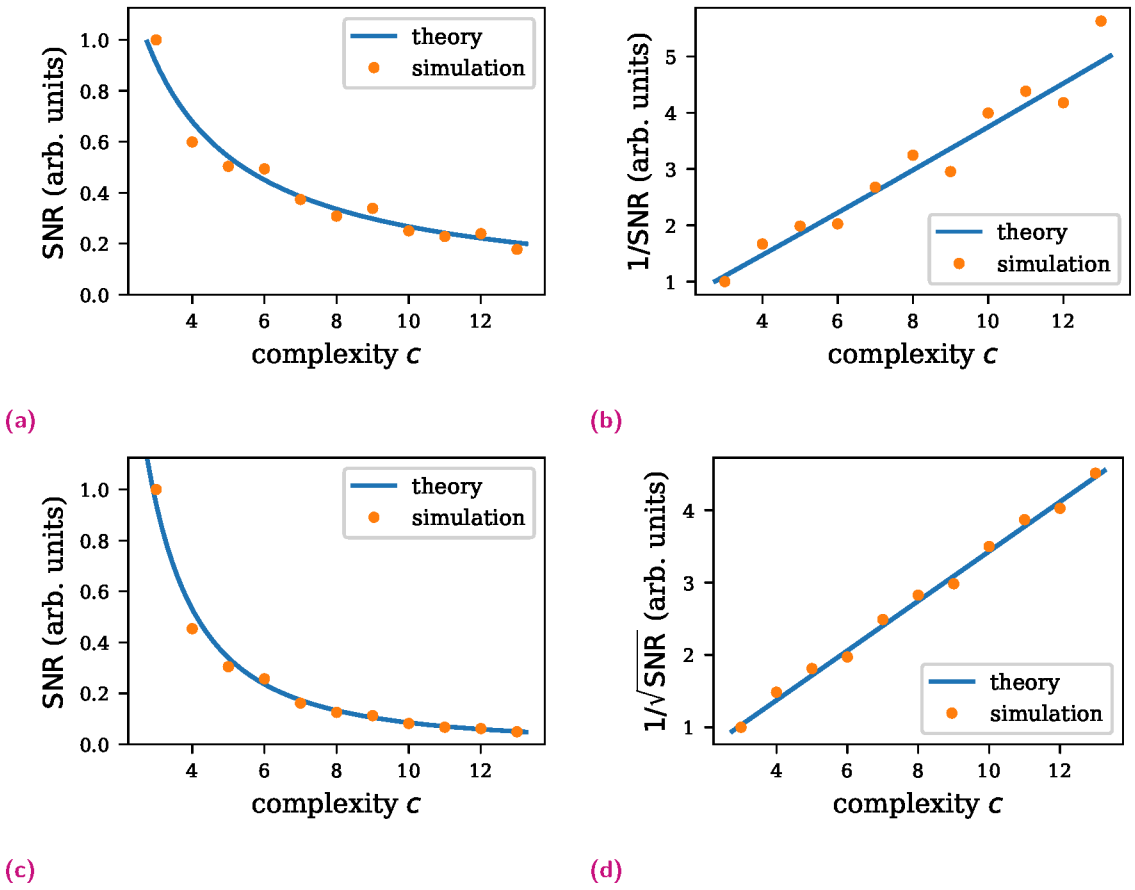

Fig. 4.9.: SNR as function of *complexity* parameterized by c. **(a)** Low intensity $\alpha_c = 0.001$. **(b)** Inverted SNR ($\alpha_c = 0.001$) to demonstrate the $1/c$ behavior in the low intensity limit. **(c)** High intensity $\alpha_c = 100$. **(d)** Inverted square root of the SNR ($\alpha_c = 100$) to demonstrate the $1/c^2$ behavior in the high intensity limit. These figures were already published in [121].

The case of low intensity, with $\alpha_c = 0.001$, is shown in Fig. 4.8a and scales as $\propto 1/c$, as expected from Eqn. (4.170) and emphasized by the $1/\mathrm{SNR}$ plot in Fig. 4.8b. SNR obtained from simulations with high photon counts, setting $\alpha_c = 100$, is given in Fig. 4.8c, which shows that the SNR scales even more strongly in this case as $1/c^2$, again in agreement with Eqn. (4.170). The simulations support the assertion that the SNR never improves as the object becomes more complex, but instead, it most probably becomes worse.

4.3 Interim summary

We saw that noise depends not only on Poisson statistics but also on the structure of the background term. Poisson statistics are, of course, familiar to coherent diffraction, such as crystallography, where the SNR usually rises in proportion to the square root of the measured counts. The random phases of the emitted waves give rise to a standard deviation in the correlation signal that is proportional to the mean (rather than the square root of the mean). This phase noise was discussed in the context of 'interferometry of intensity fluctuations in light' by Hanbury Brown and Twiss [48, 49] (there called 'wave interaction noise') but not considered by them in their further analysis. We find that phase noise leads to a saturation of the SNR at high intensities, as discussed in Section 4.2.1, indicating that higher emission from a given object does not give a proportionally higher SNR.

Furthermore, we discussed how the visibility factor affects the SNR in the case that higher intensity (photon counts) are traded at the cost of more modes. When modes are proportional to the intensity $M \propto \mu$, the influence of modes vanishes for low intensities due to the dominance of Poisson noise. In the limit of high detected counts per mode, however, the SNR is proportional to $1/\sqrt{1+4M}$ for M modes.

The most significant insight gained from the model and simulations of the IDI measurement is that the optimization of an IDI experiment, and in particular the requirement of the total number of single-shot patterns to recover the Fourier form factors of the structure of emitters in an object, depends strongly on the size and complexity of the object. This is apparent from the fact that the background term in the correlation always exceeds the magnitude of all other spatial frequencies of the Fourier spectrum of the object, and as the object becomes more complex the ratio of frequencies to the zero frequency diminishes. **Every (resolvable) emitter in the object adds to the background (and therefore to the noise) more than it adds to the signal.** In the case of crystals, it was shown in Section 4.2.3 that an increase in the number of unit-cells always decreases the SNR of a particular signal (here, the integrated strength of a Bragg peak). As a consequence, single particle imaging (SPI) renders the best possible case for IDI.

5 Experimental proof of concept

In Section 2.5, we introduced the concept of incoherent diffraction imaging (IDI) and explored its potential applications. In Chapter 3, we demonstrated the existence of multi-photon interference between X-ray fluorescence photons, and in Chapter 4, we discussed the challenges of achieving a high signal-to-noise ratio.
Based on the insights of these previous chapters, an experiment was designed and performed to showcase the imaging capabilities of IDI for a non-trivial emitter distribution. This first demonstration was designed to achieve the best possible SNR by selecting a very simple emitter structure. Specifically, we focused on two distinguishable emitter clusters, each consisting of numerous single photon emitters that form reasonably bright thermal light sources. To ensure obtaining a clear usable signal from the $g^{(2)}$-signal even at low visibility β, the experiment was designed in such a way as to collect a sufficiently large amount of data.
Note that most of the content in this chapter was already published in [123].

5.1 Experiment

The experiment was carried out at the *Materials Imaging & Dynamics instrument (MID)* of the *European XFEL* [77]. X-ray free-electron laser pulses were generated with a nominal duration of $10\,\mathrm{fs}$ and a photon energy of $9\,\mathrm{keV}$, just above the Cu K absorption edge of $8.979\,\mathrm{keV}$ [109]. These were focused on a $20\,\mu\mathrm{m}$-thick Cu foil to generate fluorescence photons. The focusing was done using two sets of compound refractive lenses (CRLs) in series with an effective diameter of $300\,\mu\mathrm{m}$ and a combined focal length of $300\,\mathrm{mm}$. The geometry of the experiment is illustrated in Fig. 5.1 (from the second CRL to the detector).

When placed into focus, the Cu foil is damaged by a single pulse, which creates a crater, see Fig. 5.2. Repeated exposures will quickly produce a hole of around $15\,\mu\mathrm{m}$ in diameter, which is bigger than the focused beam. Therefore the foil must be moved after each exposure. The FEL pulses were produced in trains with 10 trains per second. Within each pulse train, the pulses were separated by $444\,\mathrm{ns}$ ($2.25\,\mathrm{MHz}$ repetition). Therefore, the foil's speed must exceed $30\,\mathrm{m\,s^{-1}}$, which was achieved by spinning the disk-shaped foil. This foil-disk, of $150\,\mathrm{mm}$ diameter, was mounted on a spoked aluminum frame and spun at rates up to $4500\,\mathrm{rpm}$. This precise speed was chosen such that the location of the first pulse in a train would impact the foil just beyond the angular position of the last pulse of the previous train. By slowly translating the spinning foil in the $\hat{e}_y$-direction (transverse to the beam), a single foil could serve for many hours. With 10 pulse trains per second and 352 pulses per train (352 matches the frame capacity of the AGIPD detector [1]). This capability to record 3520 frames per second allowed us to obtain a dataset with 58 million patterns collected in less than 5 hours.

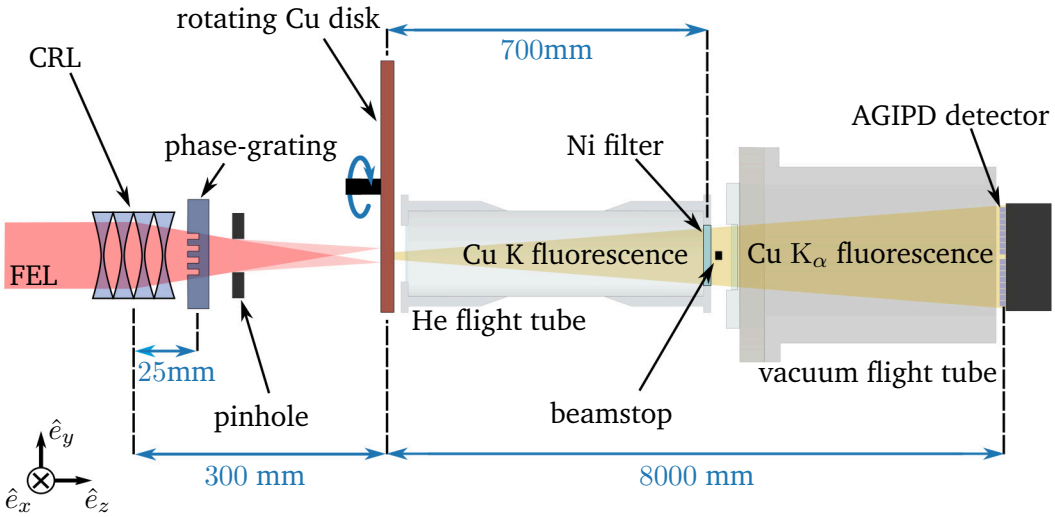

Fig. 5.1.: Simplified sketch of the experimental setup. This figure was already published in [123].

However, some craters exceeded the previous mentioned size, resulting in some unwanted signals in the subsequent pulse; these frames were selected, as described in Appendix B.2.1, and rejected for further analysis.

The foil is thicker than the $3\,\mu\mathrm{m}$ length of a $10\,\mathrm{fs}$ incident pulse. Fluorescence is therefore generated in time as this pulse propagates through the thickness of the foil, with a travel time of $67\,\mathrm{fs}$ front to rear. Nevertheless, in the forward scattering direction, all generated fluorescence arrives nearly simultaneously at the detector. Thus, no reduction of the visibility factor by the finite speed of light is expected ($\beta_c = 1$, recall the discussion in Section 3.1.2).

The angularly-resolved fluorescence was detected in the forward direction using an adaptive gain integrating pixel detector (AGIPD) with one million pixels [1] placed $8\,\mathrm{m}$ downstream of the Cu foil to ensure sufficient speckle sampling (recall Section 3.1.5). For all measurements, the detector was operated in its high-gain state, with an energy resolution of about $1\,\mathrm{keV}$, able to detect single photons but neither to reliably distinguish $8.04\,\mathrm{keV}$ Cu Kα fluorescence from $8.91\,\mathrm{keV}$ Cu Kβ fluorescence, nor from $9.00\,\mathrm{keV}$ elastically scattered photons. A $20\,\mu\mathrm{m}$ thick Ni filter was placed $700\,\mathrm{mm}$ downstream of the Cu foil, to suppress the unwanted photons. This filter transmitted $0.8\,\%$ of the elastic photons, $0.4\,\%$ of the Cu Kβ, and $43\,\%$ of the Cu Kα. A helium-filled flight tube placed between the Cu and Ni foils reduced air absorption of the fluorescence, and a beamstop was located just downstream of the Ni foil to block the remaining direct beam.

To demonstrate the ability to recover a two-dimensional real-space image of a fluorescing structure, an emitter distribution consisting predominately of two $300\,\mathrm{nm}$ diameter spots separated by $860\,\mathrm{nm}$ was created by placing a diamond phase grating in the beam path. More details on the creation of the structured emitter distribution are given later in Section 5.1.2.

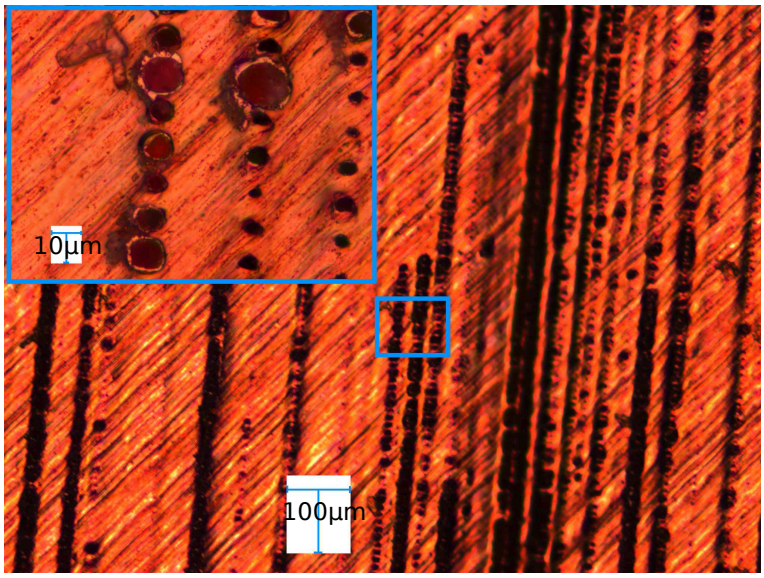

Fig. 5.2.: Microscope image of craters in a copper foil, created by XFEL pulses.

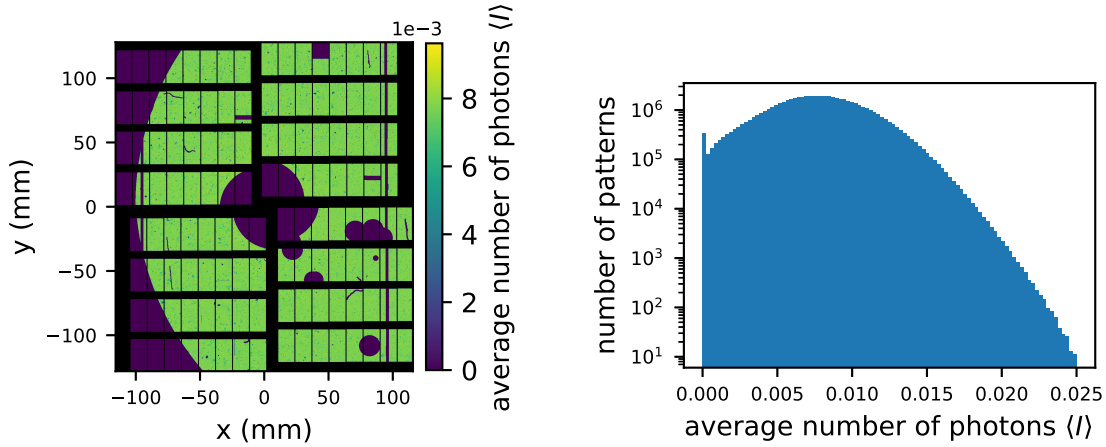

(a) (b)

Fig. 5.3.: **(a)**Photon counts at the AGIPD, measured with the phase-grating, averaged over 58 million patterns. This shows a flat distribution without any apparent structural information. The mean photon count per pixel and frame was $\langle I \rangle = 0.0077$. This figure was already published in [123]. **(b)** Frame-wise mean photon counts per pixel at the AGIPD.

5.1.1 Focus finding and determination of the visibility factor

The short-duration X-ray FEL pulses were generated with a pulse energy of 150 µJ to 350 µJ. After transmission through the beamline and the focusing optics, the energy of the pulses impinging on the Cu foil ranged from 3 µJ to 9 µJ, or 2×10^9 to 5×10^9 photons. An average of 58 300 000 recorded AGIPD frames is shown in Fig. 5.3a. Excluding shadows of the beamstop and entrance window, and masked regions of artifacts and bad pixels, the distribution of photon counts is relatively flat. For details about the detector artifacts and pixel masking, see Appendix B.2.2. The measured mean value of 0.0077 photons per pixel per pulse is comparable to 0.0063 photons per pixel estimated from the instrument detection efficiency and the production of fluorescence calculated from cold Cu cross sections. Some shadows of dust and debris can be discerned, likely on the Kapton entrance window downstream of the Cu disk. These artifacts were excluded from the analysis.

The number of pixels used in each detector frame to compute the correlations was approximately $774\,000$.

To determine the visibility factor β of fluorescence photon correlations and to locate the focal plane, a single emission spot of approximately $300\,\mathrm{nm}$ diameter was created by removing the grating from the incident FEL beam. Since $g^{(2)}$ is linearly dependent on the Fourier transform of the fluorescence emission, the best focus is found where the width of the correlation map is maximal, because the smallest transverse emitter distribution causes the largest fluorescence speckle size. A map of $g^{(2)}(q_x, q_y)$ obtained from $2\,870\,000$ frames is shown in Fig. 5.4a and 5.4b, at the longitudinal position z of the Cu foil that gave the largest correlation width.

Correlation maps ($g^{(2)}$) at different displacements z were obtained by recording frames at each position in two separate scans. The number of recorded frames per position was $3\,000\,000$ (20 minutes of data acquisition per position) for scan 1 and $1\,500\,000$ for scan 2. Please note that due to detector failures, some positions in scan 2 were recorded with about $75\,000$ frames only. The first scan (scan 1) was made prior to the insertion of $42\,\mu\mathrm{m}$ thickness of diamond in the converging beam (the substrate of the phase grating), and the second scan was made with the diamond. Even though the diamond should have little effect, a slight focus shift was observed.

As discussed in Section 4.1.1, the value of $q^{(2)}(q_x = 0, q_y = 0)$ is not usable, and due to charge sharing between neighboring pixels, this also confounds measurements at $(q_x, q_y) = (\pm 1, \pm 1)$. We approximate the CRL focus as being Gaussian, leading to a Gaussian emitter distribution $\rho(r_1, r_2) \propto e^{-r_1^2/(2\sigma_1^2) - r_2^2/(2\sigma_2^2)}$, where (r_1, r_2) form a basis rotated to (x, y) to match the axis of a 2D Gaussian representing a focus with astigmatism. The expected $g^{(2)}$ signal then, given that $|g^{(1)}|$ is the Fourier transform of the fluorescence emission, reads[1]

$$g^{(2)}(q_1, q_2) = 1 + \beta e^{-(q_1^2\sigma_1^2 + q_2^2\sigma_2^2)}\,. \tag{5.171}$$

This fit gives a focus size of

$$\begin{aligned} \mathrm{FWHM}_1 &= (640 \pm 40)\,\mathrm{nm}\,, \\ \mathrm{FWHM}_2 &= (480 \pm 30)\,\mathrm{nm}\,, \end{aligned} \tag{5.172}$$

for the smallest measured focus and a visibility $\beta = 0.018 \pm 0.002$. A plot of the inverse of the focal RMS $1/(\sigma_1\sigma_2)$, determined this way, is shown in Fig. 5.4c as a function of displacements z of the foil along the beam axis.

The focus (at $z = 0$) can be clearly discerned. The fitted visibility factor at each position, displayed in Fig. 5.4d, is approximately uniform over the defocus range. It can thus be used to estimate the FEL pulse duration, T, relative to the coherence time. The estimation of β is discussed in detail in Section 3.1, and here, we expect:

$$\beta = \beta_\mathrm{p}\beta_\mathrm{pol}\beta_\mathrm{lines} \approx 0.185\frac{\tau_c}{T}\,. \tag{5.173}$$

Therefore, a Gaussian beam shape is assumed (recall Section 3.1.1) $\beta_\mathrm{p} \approx 1/1.5$, and the fluorescence to be unpolarized $\beta_\mathrm{pol} = 0.5$. Since we were not able to discriminate K_{α_1} and K_{α_2} emissions, they contribute as incoherent modes. The branching ratio for the K_α-fluorescence are

[1] Please note that in [123] the 'spectroscopic wavenumber' notation $k = 1/\lambda$ is used, while in this work, we utilize the 'angular wavenumber' notation $k = 2\pi/\lambda$.

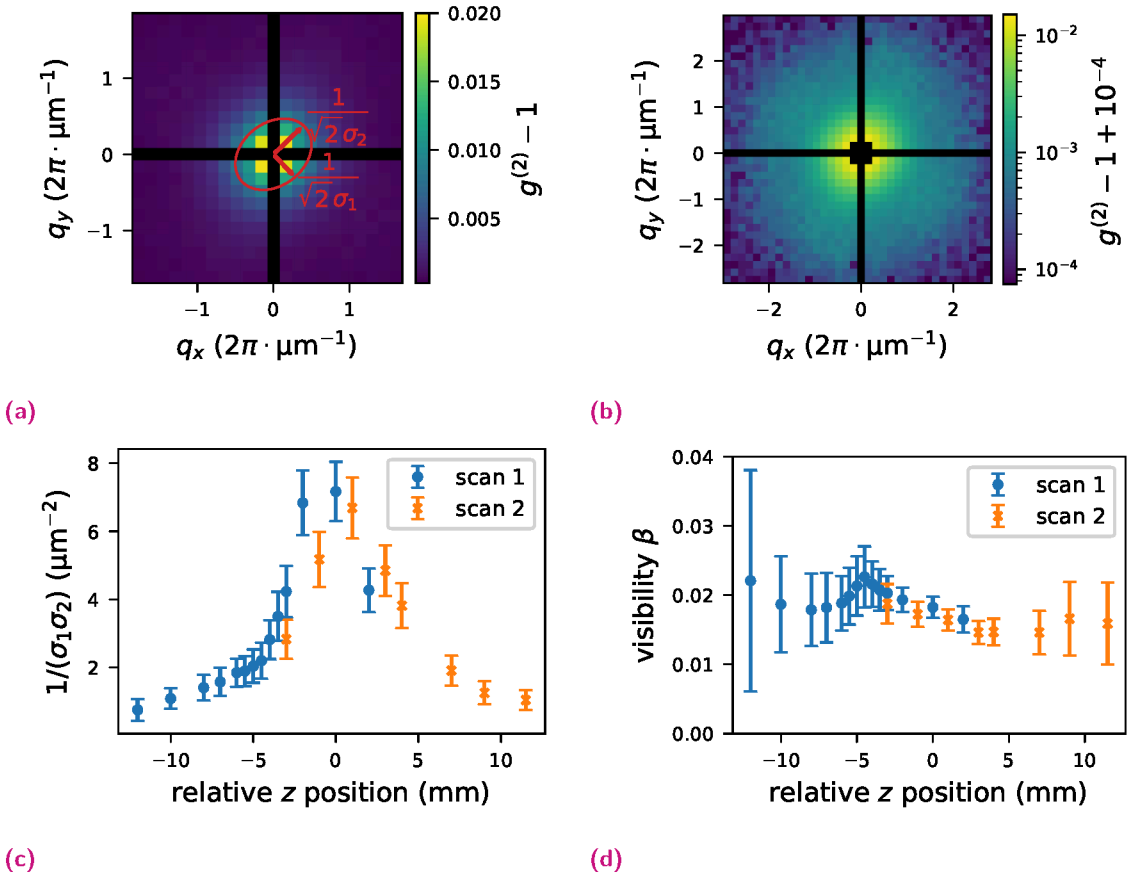

Fig. 5.4.: **(a)** $g^{(2)}$-signal of Cu Kα fluorescence with the Cu foil located in the focal plane ($z = 0$), without the phase grating. The RMS width of a fitted Gaussian is marked, with $\sigma_1 = (272 \pm 17)\,\mathrm{nm}$ and $\sigma_2 = (204 \pm 13)\,\mathrm{nm}$. **(b)** Same as (a) but in logarithmic representation, wherefore an offset of 1×10^{-4} was added. **(c)** Inverse of the focal area $1/(\sigma_1\sigma_2)$, versus defocus z. **(d)** Visibility factor β as a function of z. These figures were already published in [123].

$R_{\mathrm{K}_{\alpha,1}} = 0.581$, and $R_{\mathrm{K}_{\alpha,2}} = 0.297$, respectively [8]. This yields a factor $\beta_{\mathrm{lines}} = (R_{\mathrm{K}_{\alpha,1}}/(R_{\mathrm{K}_{\alpha,1}} + R_{\mathrm{K}_{\alpha,2}}))^2 + (R_{\mathrm{K}_{\alpha,2}}/(R_{\mathrm{K}_{\alpha,1}} + R_{\mathrm{K}_{\alpha,2}}))^2 \approx 5/9$.

The coherence time of copper K_α is $\tau_c = 0.6\,\mathrm{fs}$, given by twice the radiative lifetime $\hbar/\Gamma$ for a spectral linewidth of $\Gamma = 2.17\,\mathrm{eV}$ [66]. Thus, the measured visibility factor corresponds to an effective pulse duration of

$$T = (6.2 \pm 0.8)\,\mathrm{fs}\,. \tag{5.174}$$

5.1.2 Structured emitter distribution

In order to obtain a non-trivial emitter distribution, the diamond phase grating was placed in the beam $25\,\mathrm{mm}$ downstream of the CRL's principal plane. The grating period was $80\,\mu\mathrm{m}$ and consisted of equal width bars of alternating heights, differing by $8.4\,\mu\mathrm{m}$ to induce a π phase shift at a photon energy of $9\,\mathrm{keV}$. A transmission electron microscope image of the diamond phase grating is shown in Fig. 5.5. The complex transmissions of the bars were thus 1 and -1, producing dominant ± 1 orders without any zero order, separated by $860\,\mathrm{nm}$ in the focal plane.

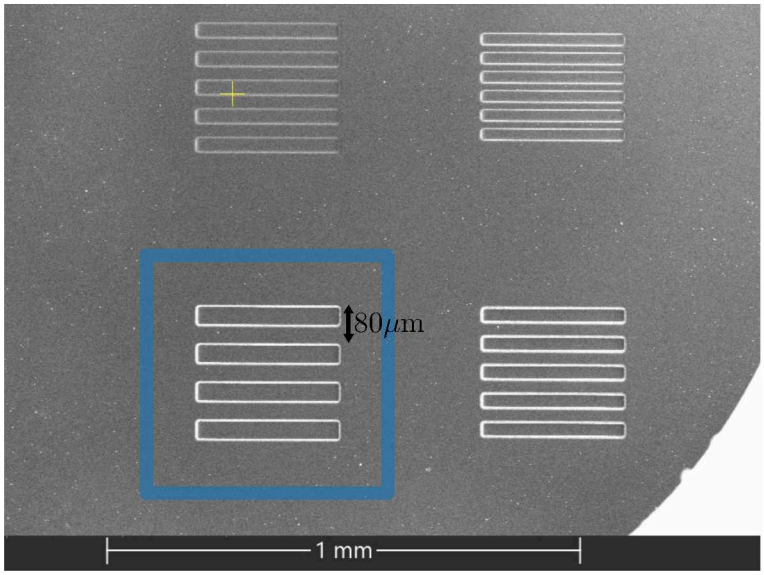

Fig. 5.5.: Transmission electron microscope image of the diamond phase grating. The used grating in the here presented experiment is marked.

To calculate the expected emitter density, an incident FEL beam with a Gaussian shape with $175\ \mu\mathrm{m}$ FWHM and wavelength $\lambda = 1.38\,\text{Å}$ was assumed:

$$\psi_-(x, y, z = -30\,\mathrm{mm}) \propto e^{-(x^2+y^2)/(2(75\,\mu\mathrm{m})^2)}\,. \tag{5.175}$$

A radial symmetric phase-shift was applied to simulate a perfect lens with the focal length $f = 30\,\mathrm{mm}$:

$$\psi_+(x, y, z = -30\,\mathrm{mm}) = \psi_-(x, y, z = -30)e^{i(2\pi/\lambda)\sqrt{f^2-x^2-y^2}}\,. \tag{5.176}$$

The wave field was propagated via Fresnel propagation (recall Eqn. (2.18)) for $25\,\mathrm{mm}$, and then the phase shifts induced by the phase grating were applied. The phase grating was rotated by $17°$ counterclockwise around the z-axis to ensure that the expected features of the resulting $g^{(2)}$-map are not parallel to the detector rows or columns, in order to avoid any confusion with possible detector artifacts (e.g., common readout modes). The resulting wave field was then Fresnel propagated another $275\,\mathrm{mm}$ up to the position of the Cu foil, resulting in the intensity distribution displayed in Fig. 5.6a.

The intensity distribution equates to the fluorescence emitter distribution, and the expected $g^{(2)}$-map at a detector placed another $8\,\mathrm{m}$ downstream is displayed in Fig. 5.6b. The actual measured results are discussed in the following section.

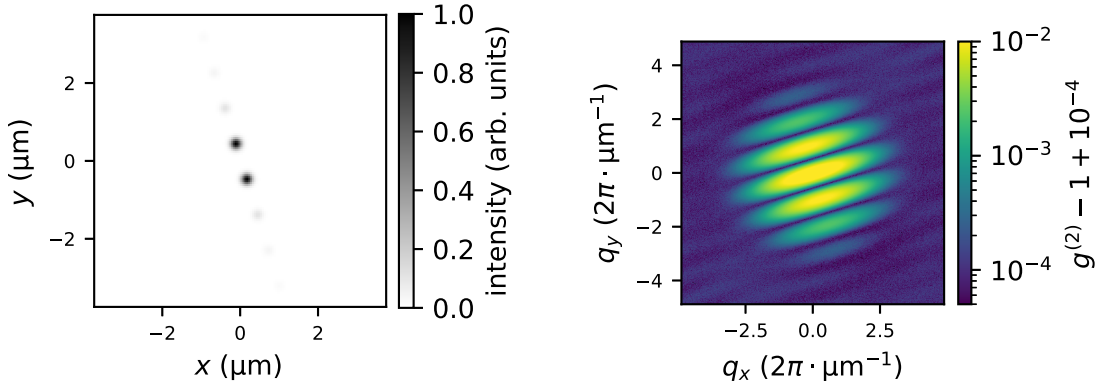

(a) (b)

Fig. 5.6.: **(a)** Simulated intensity distribution in the focal plane with the phase grating. **(b)** Simulated $g^{(2)} - 1$ signal for the intensity distribution displayed in (a), with an assumed visibility of $\beta = 0.018$. These figures were already published in [123].

5.2 Demonstration of imaging via photon-photon correlation of X-ray fluorescence

Detector frames were obtained with the phase grating inserted in the incident XFEL beam, recording fluorescence emission from predominately two spots, as discussed in Section 5.1.2 and displayed in Fig. 5.6a. A total of 58 million frames were recorded, and the resulting $g^{(2)}$ signal is displayed in Fig. 5.7a (the offset was subtracted except for a value of 1×10^{-4} to allow a logarithmic scale). It shows a fringe pattern that is compatible with the predicted pattern of Fig. 5.6b. Fringes to the third order can be discerned, showing that the signal extends to $|q|/(2\pi) \approx 4\,\mu\mathrm{m}^{-1}$. The RMS of the background is measured at $\sigma_{\mathrm{Bgr}} = 3.52 \times 10^{-5}$, which can be considered the noise floor. A projection of the $g^{(2)} - 1$ signal is shown in Fig. 5.7b along the direction of the grating modulation by summing pixels between the red dashed lines in Fig. 5.7a. Here, fringes up to the third order can be discerned.

An image of the fluorescing structure cannot be obtained solely from the Fourier magnitudes of the structure, additionally requiring knowledge of the Fourier transform phase map. The $g^{(2)}$ measurement does not provide the phase map, resulting in the well-known 'phase problem' [28]. The phases were obtained via iterative phase retrieval [111] by constraining the image to be the most compact structure consistent with the Fourier magnitudes $|F(\vec{q})| = \sqrt{g^{(2)}(\vec{q}) - 1}$, determined from the map given in Fig. 5.7a. The phasing was carried out using the 'Shrinkwrap' algorithm [81]. The phase retrieval is described in detail in Appendix B.2.3. The reconstructed image of the fluorescing emitter distribution, obtained by averaging 1000 phase retrieval trials, is shown in Fig. 5.7c. It shows two well-resolved diffraction spots of the grating. Note that the upper one of the spots is approximately $15\,\%$ brighter than the other[2]. Each spot has an FWHM of about $400\,\mathrm{nm}$. **The results depicted in Fig. 5.7 indicates the general feasibility of imaging via the correlation of hard X-ray fluorescence photons.**

[2]This observation was consistent over many different phasing attempts and therefore it is unlikely that this observation is due to some phasing error.

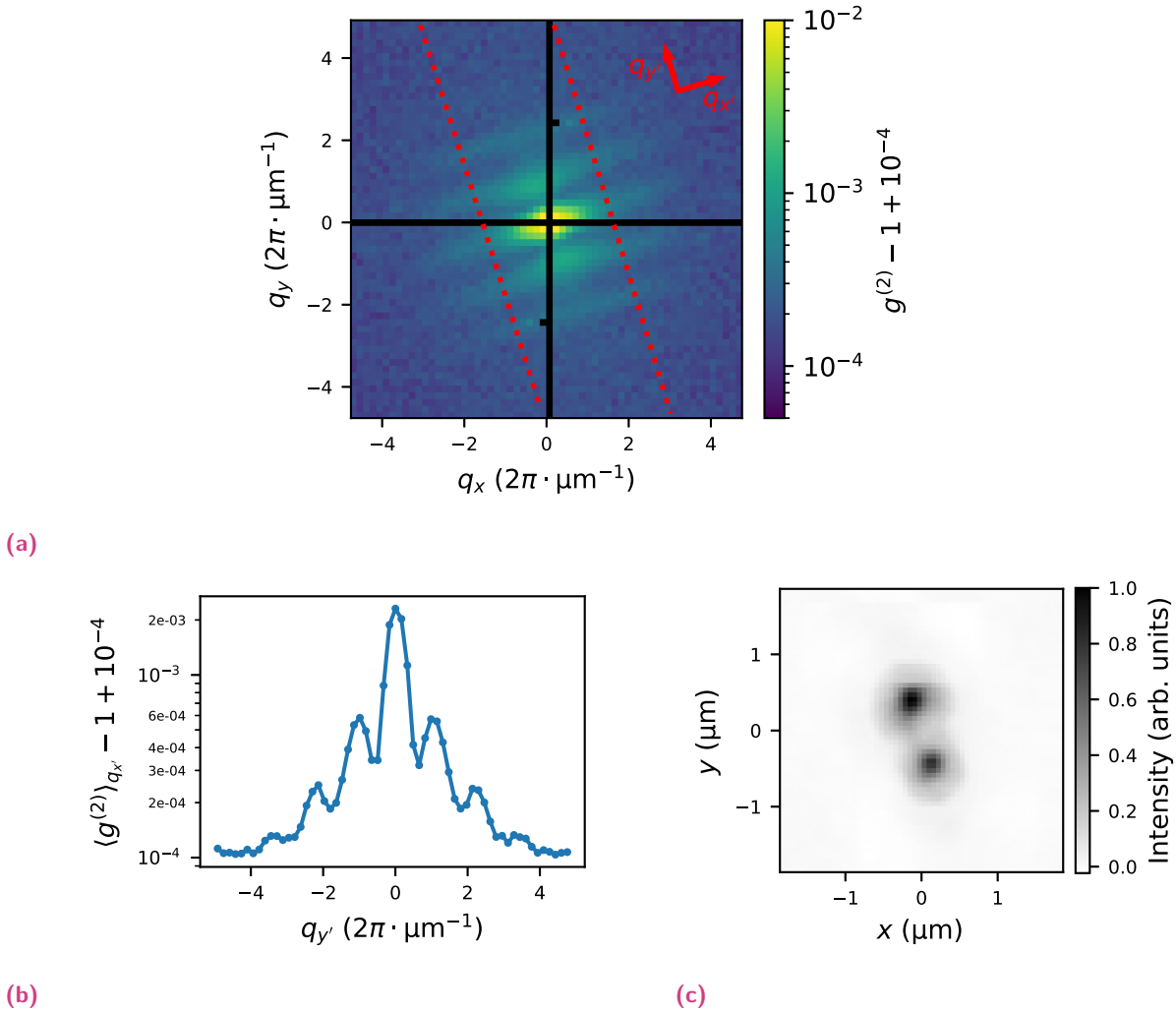

Fig. 5.7.: **(a)** Measured $g^{(2)} - 1$ signal in logarithmic representation. **(b)** Cut through the $g^{(2)} - 1$ signal along $q_{y'}$ and integrated along $q_{x'}$ within the boundaries indicated in (a). **(c)** Reconstructed intensity distribution and thus the fluorescence emitter distribution at the Cu disk. To be compared to the simulation in Fig. 5.6a. These figures were already published in [123].

We can roughly compare the results of the structured emitter distribution with the results of the measurements without the phase grating in terms of signal-to-offset ratio. Therefore, we define the integrated, 'usable signal' as the sum over sufficiently many pixels in q-space (here 100×100) to cover the whole signal, as

$$\Sigma_{\text{Sig}} = \sum_{q_x=-50}^{50} \sum_{q_y=-50}^{50} \left(g^{(2)}(q_x, q_y) - 1 \right) . \tag{5.177}$$

In the present case, q_x and q_y represent the q-space coordinates in pixels. We obtain

$$\begin{aligned} \Sigma_{\text{Sig, Focus}} &\approx 1.02 \,, \\ \Sigma_{\text{Sig, Grating}} &\approx 0.34 \,, \end{aligned} \tag{5.178}$$

with $\Sigma_{\text{Sig, Focus}}$, and $\Sigma_{\text{Sig, Grating}}$ for the focus only (without phase grating), as displayed in Fig. 5.4a, and for the structured case, as displayed in Fig. 5.7a, respectively. Although we expected a similar visibility factor for both cases, we observe a significantly lower integrated, usable signal for the grating case. That indicates a lower signal-to-offset ratio, which was expected due to the emitter distribution's higher complexity, as discussed earlier in Section 4.2.3.

6 Summary and Outlook

In this thesis, a theoretical overview of *incoherent diffraction imaging via X-ray fluorescence*, as well as the experimental proof of concept, was presented. After recapitulating the basic concepts of coherence, *coherent diffraction imaging (CDI)*, and photon statistics in Chapter 2, we have introduced the concept of *incoherent diffraction imaging (IDI)*. This was done in the classical approximation and in terms of quantum optics. As a result, we realized that the classical approximation is sufficient in the case of thermal light sources or in the limit of many single photon emitters. The latter could safely be assumed for the experiments presented in the scope of this work and for most further interesting applications of IDI.

Unlike in CDI, the 'usable signal' in IDI is retrieved on top of an offset and modulated (reduced) by the so-called 'visibility factor'. A comprehensive discussion about this visibility factor was presented in Chapter 3. The visibility factor is not only a crucial parameter to be optimized for IDI experiments, but it can also be used to obtain parameters about the excitation XFEL pulse, such as the pulse duration. The visibility factor in IDI is also equivalent to the speckle contrast, which can be directly obtained from the measured frames without the need to perform intensity-intensity correlations. An experiment was presented where the speckle contrast of X-ray fluorescence, excited by XFEL pulses with two different pulse durations, was measured. We observed a higher speckle contrast for the fluorescence, excited by the shorter pulses. This increase in speckle contrast is a clear indication of interference of X-ray fluorescence – a vital requirement for the feasibility of IDI.

However, the estimation of the speckle contrast was complicated by the very sparse photon count combined with a highly fluctuating total number of photons per measured frame. Therefore, the method 'weighted speckle contrast estimation' was introduced. That method was also evaluated on simulated data and turned out to be significantly more reliable than the conventional 'unweighted speckle contrast estimation' in the described circumstances. This presented method of weighted speckle contrast estimation might also be useful for X-ray speckle visibility spectroscopy (XSVS) (e.g., to study diffusion or vibrational modes in liquids and glasses at atomic scale [70, 102]). Especially at XFELs, due to the fluctuating intensity of different X-ray pulses or when a serial deployment of the specimens is utilized, this method should be helpful.

A comprehensive discussion about the expected signal-to-noise ratio for IDI experiments was given in Chapter 4. The presented model is based on a classical description of wave interference combined with Poisson photon statistics. The model was further confirmed with simulations of IDI measurement, which are also based on the classical approximation. The most essential – yet also most contra-intuitive insight is that more complex emitter distributions suffer from a lower SNR than less complex ones. Higher complexity in this context means more resolvable emitter clusters.

This is apparent from the fact that the offset term in the intensity-intensity correlation always exceeds the magnitude of all other spatial frequencies of the object's Fourier spectrum. When the object becomes more complex, the ratio of spatial frequencies ($\vec{q} \neq 0$) to the zero-frequency ($\vec{q} = 0$) diminishes. Every (resolvable) emitter in the object adds to the offset (and therefore the noise) more than it adds to the usable signal. The consequence of this insight is significant. For example, in the CDI context repeating patterns, particularly crystals, are used to amplify the measured signal. However, this is impossible for IDI, meaning *single particle imaging* (SPI) gives the best possible SNR. SPI is an emerging method for CDI [90, 2, 3], which, however, is yet to be demonstrated on small and complex molecules such as proteins.

Chapter 5 presented an experiment that first demonstrated IDI via X-ray fluorescence on a simple yet non-trivial emitter distribution. Non-trivial, in this context, means more than one connectedly emitter clusters – in our case, two clusters. The observed fringes in the $g^{(2)}$-signal (Fig. 5.7a) clearly indicate the feasibility of imaging via the correlation of hard X-ray fluorescence photons. Also, phasing on the usable signal was successfully performed, and the emitter distribution was reconstructed.

In the presented experiment, IDI was also used to find the XFEL's focus and to determine its pulse duration. The obtained pulse duration of $6.2\,\mathrm{fs}$ was around ten times longer than the $0.6\,\mathrm{fs}$ coherence time of Cu K_α fluorescence, resulting in the incoherent addition of around 55 coherent modes in each measurement (this includes the non-polarization and indistinguishable emission lines). The number of detected photons per pixel per mode was thus $\mu_0 \approx \langle I \rangle / 55 \approx 1.4 \times 10^{-4}$, generated by about 1.2×10^8 incident X-ray photons per mode ($200\,\mathrm{nJ}$). These numbers can be used to estimate the required statistics for further IDI experiments.

Outlook

The here presented first imaging demonstration was possible due to a massive amount of recorded frames. From the SNR discussion, we know that (for reasonably low intensities) the SNR is proportional to the number of detected photons per mode. Therefore, significant reductions in the required number of frames, which scales $1/\mathrm{SNR}^2$, could be obtained with modest improvements in source properties. High-brightness attosecond-duration photon sources [97] could achieve parity of the coherence and detection time ($\beta \approx 0.28$ to $\beta \approx 0.14$ or 3.6 to 7 modes). Assuming the same incident power (1.2×10^8 incident photons) we had in the experiment presented in Chapter 5, crunched into 5.5 modes instead of 55, the amount of frames reduces by a factor of 0.01 to accomplish an equivalent SNR. That would correspond to a power of approximately $1\,\mathrm{GW}$. The then required $580\,000$ frames could be collected within three minutes, assuming the same repetition rate. Additional gains could be achieved by increasing power. For example, a $1\,\mathrm{TW}$ incident pulse ($0.6\,\mathrm{mJ}$ in $0.6\,\mathrm{fs}$) would provide 0.18 photons per pixel per mode, dramatically increasing the SNR. The presented experiment's SNR would even be close to the saturation discussed in Chapter 4. Additionally, multiple detectors could be placed to record the isotropic X-ray fluorescence to increase the number of detected photons per shot and, thus, the number of potential photon-photon correlations. This would provide a corresponding increase of the

SNR as well as the potential to increase the resolution to a limit of $\lambda/2$ with detectors arranged in opposite directions. Together, all these factors would allow similar results as achieved in the presented experiment with only tens to hundreds of pulses.

Based on that result, and the in this work discussed SNR scalings, incoherent diffraction imaging via X-ray fluorescence should be feasible to obtain high-resolution three-dimensional images of fluorescing structures. For example, for the real-time analysis of the formation and evolution of dense plasmas (potentially interesting for plasma physics [33]). The presented results are also consistent with predictions to image clusters and single molecules at atomic resolution [13, 53, 112]. The small dimension of such objects substantially relaxes the detector's angular resolution requirements, making it practical to record fluorescence over large solid angles with current pixel-array detectors. Unlike elastic scattering, where atomic scattering factors fall precipitously with the scattering angle and require even greater exposure to increase the spatial resolution, fluorescence is emitted uniformly in all directions. Therefore, the imaging of atomic structures does not necessarily require higher intensities than discussed here. Diffraction measurements of single particles or macromolecules [90, 108, 3] could be readily combined with simultaneous fluorescence measurements, which themselves could be extended to discriminate fluorescence photons over a wide spectral range. For example, imaging substructures with IDI could be used to track charge transfer or progression of oxidation states in the bio-complexes [114] of photosynthesis or other catalytic systems.

Presupposed a sufficiently good SNR, also higher-order correlations $g^{(n)}(\vec{k}_1, \ldots, \vec{k}_n)$, with $n > 2$ could be performed. Such correlations could enable higher resolutions [93, 36] and could also be used to solve the phase problem [35, 124, 98]. However, it should be mentioned that the complexity component of the SNR becomes more devastating for higher correlation orders. In the worst case and in the high-intensity limit, the SNR could scale with SNR $\propto 1/c^n$, with c denoting the complexity parameter.

A Theory

A.1 Notation of probability distributions

In the scope of this work, we often use probability distributions to describe statistical processes. Therefore, the following notation for the *probability density* was chosen:

$$P(x|a_1, \dots a_n)\,, \tag{A.179}$$

which represents the probability that a distributed variable X has the value x, given the parameter $a_1, \dots a_n$. In general, $P(x|a_1, \dots a_n)$ is normalized

$$\begin{aligned} \int_{-\infty}^{\infty} P(x|a_1, \dots a_n)\, dx = 1 \,|\, \forall x \in \mathbb{R}\,, \\ \sum_{x=-\infty}^{\infty} P(x|a_1, \dots a_n) = 1 \,|\, \forall x \in \mathbb{Z}\,, \end{aligned} \tag{A.180}$$

for float and integer values of x, respectively. The expectation value $\mathbb{E}(X)$ is calculated by

$$\begin{aligned} \int_{-\infty}^{\infty} P(x|a_1, \dots a_n) x\, dx = \mathbb{E}(X) \,|\, \forall x \in \mathbb{R}\,, \\ \sum_{x=-\infty}^{\infty} P(x|a_1, \dots a_n) x = \mathbb{E}(X) \,|\, \forall x \in \mathbb{Z}\,. \end{aligned} \tag{A.181}$$

It should be emphasized that the expectation value must not be confused with the mean value $\langle X \rangle$. The mean value is calculated from an ensemble of N, $P(x|a_1, \dots a_n)$-distributed yet uncorrelated, random variables X_j

$$\langle X \rangle = \frac{1}{N} \sum_{j=1}^{N} X_j\,. \tag{A.182}$$

Only in the limit of $N \to \infty \Rightarrow \langle X \rangle \to \mathbb{E}(X)$ the mean becomes the expectation value.
The variance $\mathrm{Var}(X)$ is calculated as follows:

$$\begin{aligned} \int_{-\infty}^{\infty} P(x|a_1, \dots a_n)\, (x - \mathbb{E}(X))^2\, dx = \mathrm{Var}(X) \,|\, \forall x \in \mathbb{R}\,, \\ \sum_{x=-\infty}^{\infty} P(x|a_1, \dots a_n)\, (x - \mathbb{E}(X))^2 = \mathrm{Var}(X) \,|\, \forall x \in \mathbb{Z}\,. \end{aligned} \tag{A.183}$$

A.2 Negative binomial distribution as a combination of Bose-Einstein distributions

We use mathematical induction to prove that the sum of M Bose-Einstein distributed values (Eqn. (2.63)) is indeed a negative binomial distributed value (Eqn. (2.63)). The relationship we want to prove is given as

$$P_{\mathrm{NB}}(x|\mu,M) \stackrel{!}{=} \sum_{a_1=0}^{\infty}\sum_{a_2=0}^{\infty}\cdots\sum_{a_M=0}^{\infty}\delta_{x,\sum_{j=1}^{M}a_j}\prod_{j=1}^{M}P_{\mathrm{BE}}\left(a_j\middle|\frac{\mu}{M}\right), \tag{A.184}$$

which states that the integer variable x with the expectation value $\mathbb{E}(x)=\mu$ is the sum of M Bose-Einstein distributed values a_j, with the expectation value $\mathbb{E}(a_j)=\mu/M$, each. We state that the negative-binomial distribution returns the probability of x given μ and M.

Base case:

$$P_{\mathrm{NB}}(x|\mu,M=1)=P_{\mathrm{BE}}(x,\mu)\,, \tag{A.185}$$

that this is true can simply be demonstrated by substitution.

Induction step:

Since the base case is true, we need to prove that

$$P_{\mathrm{NB}}\left(x\middle|\mu+\frac{\mu}{M},M+1\right) \stackrel{!}{=} \sum_{a_1=0}^{\infty}\sum_{a_2=0}^{\infty}\delta_{x,a_1+a_2}P_{\mathrm{NB}}(a_1|\mu,M)P_{\mathrm{BE}}\left(a_2\middle|\frac{\mu}{M}\right) \tag{A.186}$$

is the combination of a negative binomial distribution and a Bose-Einstein distribution. Since $\delta_{x,a_1+a_2}=1$ only if $a_1+b_1=x$ and else 0, we can substitute $a_2=x-a_1$ (and $a_1=a$) and drop the second sum. Eqn. (A.186) then reduces to

$$\sum_{a_1=0}^{\infty}\sum_{a_2=0}^{\infty}\delta_{x,a_1+a_2}P_{\mathrm{NB}}(a_1|\mu,M)P_{\mathrm{BE}}\left(a_2\middle|\frac{\mu}{M}\right)=\sum_{a=0}^{x}\frac{M^{1+M}\mu^x(\mu+M)^{-(M+x+1)}(M+a-1)!}{a!(M-1)!}\,. \tag{A.187}$$

With the relation $\sum_{a=0}^{x}(a+M+1)!/a!=((1+x)(M+x)!)/(M(1+x)!)$, Eqn. (A.187) evaluates to

$$\sum_{a=0}^{x}\frac{M^{1+M}\mu^x(\mu+M)^{-(M+x+1)}(M+a-1)!}{a!(M-1)!}=\frac{M^{M+1}\mu^x(M+\mu)^{-(M+x+1)}(M+x)!}{M!x!}\,, \tag{A.188}$$

which equates exactly $P_{\mathrm{NB}}\left(x|\mu+\frac{\mu}{M},M+1\right)$ ■.

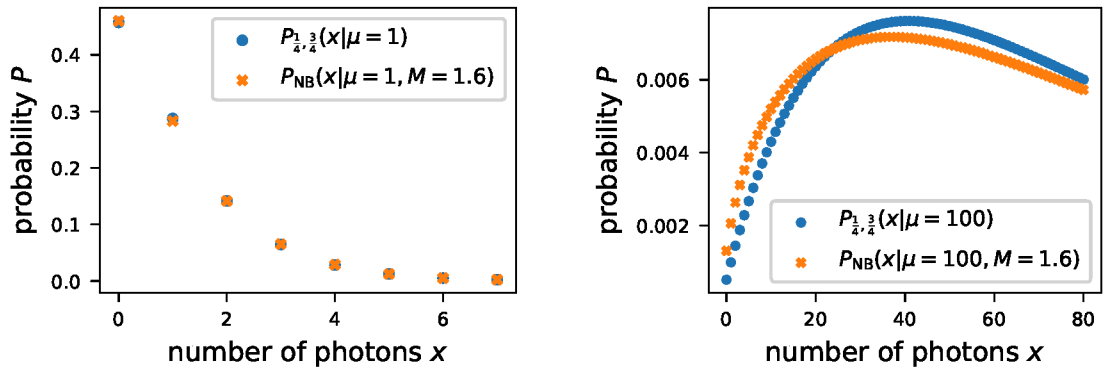

(a) (b)

Fig. A.1.: Two combined Bose-Einstein distributions with $\mu_1 = \mu/4$ and $\mu_2 = 3\mu/4$ (see Eqn. (A.190)), along side the negative binomial distribution with $M = 1.6$ for **(a)** $\mu = 1$ and **(b)** $\mu = 100$. Note the significant deviation for (b).

A.2.1 Real non-integer M by combining Bose-Einstein distributions with different μ – approximated by negative binomial distributions

The previous derivation is only valid for an integer number of modes M which is also a consequence of the assumption of orthogonal states. However, we can combine modes with different photon count expectation values.

As a first example, we combine two Bose-Einstein distributions, the first with $\mu_1 = (1/4)\mu$ and the second with $\mu_2 = (3/4)\mu$. The expected visibility is obtained by the probability that two photons can interfere. Since the photons must belong to the same mode, the visibility, and thus the expected (non-integer) number of modes, is given by

$$\beta_{\frac{1}{4},\frac{3}{4}} = \left(\frac{1}{4}\right)^2 + \left(\frac{3}{4}\right)^2 = \frac{1}{M_{\frac{1}{4},\frac{3}{4}}} = \frac{1}{1.6}\,. \tag{A.189}$$

The combined probability reads

$$P_{\frac{1}{4},\frac{3}{4}}(x|\mu) = \sum_{x'=0}^{x} P_{\mathrm{BE}}(x'|\mu/4) P_{\mathrm{BE}}(x-x'|3\mu/4) = \frac{2}{(4+\mu)^x}\left(3^{x+1}\frac{(4\mu+\mu^2)^x}{(4+3\mu)^{x+1}} - \frac{\mu^x}{4+\mu}\right)\,. \tag{A.190}$$

The expectation value is $\mathbb{E}(x) = \mu$, and the variance $\mathrm{Var}(x) = \mu + (1/1.6)\mu^2$, as expected. However, this is not a negative binomial distribution $P_{\frac{1}{4},\frac{3}{4}}(x|\mu) \neq P_{\mathrm{NB}}(x|\mu, M = 1.6)$, which is illustrated in Fig. A.1, where $P_{\frac{1}{4},\frac{3}{4}}(x|\mu)$ is plotted together with $P_{\mathrm{NB}}(x|\mu, 1.6)$. For small expectation values (here $\mu = 1$), they seem to be in good agreement (see Fig. A.1a). However, that is definitely not the case for larger μ (see Fig. A.1b, with $\mu = 100$).

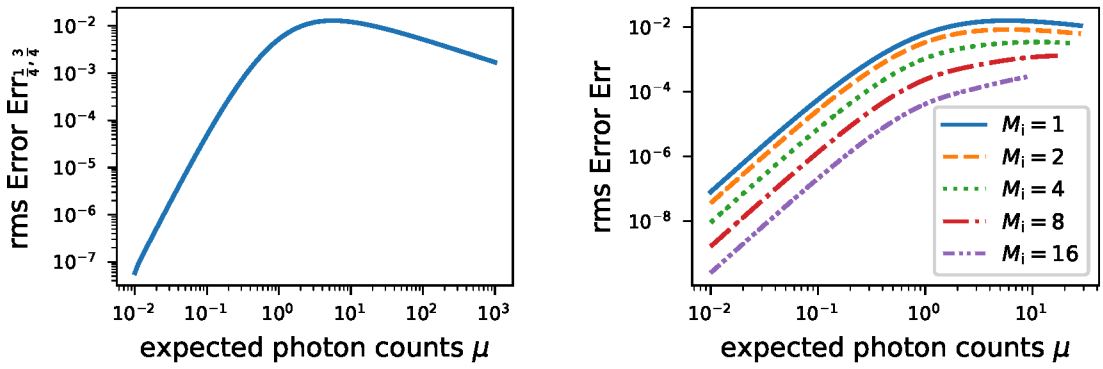

(a) (b)

Fig. A.2.: **(a)** Root mean square deviation between $P_{\mathrm{NB}}(x|\mu, M = 1.6)$ and $P_{\frac{1}{4},\frac{3}{4}}(x|\mu)$ as a function of μ. **(b)** Root mean square deviation between $P_{\mathrm{NB}}(x|\mu, M_\mathrm{i} + 0.5)$ and $P_{\mathrm{combined}}(x|\mu, M_\mathrm{i} + 0.5)$ as a function of μ for various M_i.

To quantify the deviation, we define the RMS error as

$$\mathrm{Err}_{\frac{1}{4},\frac{3}{4}}(\mu) = \sum_{x=0}^{\infty} \left(P_{\frac{1}{4},\frac{3}{4}}(x|\mu) - P_{\mathrm{NB}}(x|\mu, M = 1.6) \right)^2 , \tag{A.191}$$

which is plotted in Fig. A.2a. We can see that the combined Bose-Einstein distributions with different expectation values approximated as negative binomial distribution seems well justified for small μ but needs to be seen with caution for larger μ.

To combine Bose-Einstein distributions to obtain a distribution with an arbitrary floating point number of modes M, we split $M = M_\mathrm{i} + M_\mathrm{f}$ into an integer-valued M_i and the remaining part $0 \leq M_\mathrm{f} < 1$. The distribution is then calculated by

$$P_{\mathrm{combined}}(x|\mu, M) = \sum_{a_1=0}^{\infty} \sum_{a_2=0}^{\infty} \cdots \sum_{a_{M_\mathrm{i}}=0}^{\infty} \sum_{a_{M_\mathrm{i}+1}=0}^{\infty} \delta_{x,\sum_{j=1}^{M_\mathrm{i}+1} a_j} \left(\prod_{j=1}^{M_\mathrm{i}} P_{\mathrm{BE}}\left(a_j \middle| \frac{\mu}{c_1} \right) \right) P_{\mathrm{BE}}\left(a_{M_\mathrm{i}+1} \middle| \frac{\mu}{c_2} \right) , \tag{A.192}$$

with the divisors

$$\begin{aligned} c_1 &= \frac{M_\mathrm{i} + \sqrt{(1 - M_\mathrm{f}) M_\mathrm{i} M}}{M - 1} \text{, and} \\ c_2 &= \frac{M + \sqrt{(1 - M_\mathrm{f}) M_\mathrm{i} M}}{M_\mathrm{f}} . \end{aligned} \tag{A.193}$$

The RMS error was calculated analogously to Eqn. (A.191), is plotted in Fig. A.2b for $M_\mathrm{f} = 0.5$ and various M_i. We can see that the deviation decreases for larger M_i.
In general, n modes with arbitrary expected counts μ_j can be combined into a distribution

$$P_{\mathrm{combined}}(x|\mu_1, \mu_2, \ldots \mu_n) = \sum_{a_1=0}^{\infty} \cdots \sum_{a_n=0}^{\infty} \delta_{x,\sum_{j=1}^{n} a_j} \prod_{j=1}^{n} P_{\mathrm{NB}}(x|\mu_j) , \tag{A.194}$$

and the expectation value will be $\mathbb{E}(x) = \sum_{j=1}^{n} \mu_j = \mu$ and the variance Var $= \mu + \mu^2 \sum_{n}^{j=1} \mu_j^2/\mu^2$, regardless of the exact shape of this distribution. Then, the number of modes is given by

$$M = \left(\sum_{j=1}^{n} \frac{\mu_j^2}{\mu^2} \right)^2 . \tag{A.195}$$

Considering the exemplary evaluations presented in this section, we can state that for small photon counts $\mu \ll 1$, the approximation of a negative binomial distribution is well justified. These small photon counts are the case for the measured data discussed in this work. Also, note that the derivation of Eqn. (4.148) in Chapter 4 is only based on the variances (see Eqn. (4.139) and Eqn. (4.140)) and thus is not affected by the approximation discussed here.

A.3 Visibility

A.3.1 Gating by pulse duration: how to consider the pulse shape

There are two contradicting models on how to consider the excitation pulse shape. In Section 3.1.1, the method proposed by Lohse et al. [74] was used. However, Inoue et al. [58] proposed to use the 'intensity envelope function' instead of the normalized pulse shape:

$$\tilde{P}(t) = C e^{-\frac{t}{\tau_l} + \frac{\sigma_t^2}{2\tau_l^2}} \operatorname{erfc}\left(\frac{\sigma_t}{\sqrt{2}\tau} - \frac{t}{\sqrt{2}\sigma_t} \right) . \tag{A.196}$$

For our purposes, we have changed the notation $P(t) \to \tilde{P}(t)$ to distinguish it from $P(t)$ as defined in Eqn. (3.93). We identify Eqn. (A.196) as the convolution of a Gaussian-shaped pulse

$$P(t) = \frac{1}{\sqrt{2\pi}\sigma_t} e^{-\frac{t^2}{2\sigma_t^2}} , \tag{A.197}$$

with the fluorescence intensity, excited by a delta-like pulse:

$$I_{\mathrm{fl}}(t) = \tau_l^{-1} e^{-\frac{t}{\tau_l}} \Theta(t) . \tag{A.198}$$

Here $\tau_l = 1/(2\tau_c)$ denotes the lifetime and $\Theta(t)$ the Heaviside step function. Now, the intensity envelope function can be calculated by

$$\tilde{P}(t) = P * I_{\mathrm{fl}} , \tag{A.199}$$

and we obtain Eqn. (A.196), as published by Inoue et al.. Since normalization is required for $\tilde{P}(t)$, the constant C in Eqn. (A.196) reads $C = 1/(2\tau_l)$. We can write the auto-correlation of the 'intensity envelope function' as

$$\tilde{\Pi} = (P * I_{\mathrm{fl}}) \star (P * I_{\mathrm{fl}}) . \tag{A.200}$$

Using the Fourier convolution theorem[1], the Fourier cross-correlation theorem[2], and the real nature of $P(t) \in \mathbb{R}$, combined with its symmetric shape $P(t) = P(-t) \Leftrightarrow (\mathfrak{F}[P])^* = \mathfrak{F}[P]$, we can bring Eqn. (A.200) into the following form:

$$\tilde{\Pi} = (I_{\text{fl}} \star I_{\text{fl}}) * (P * P) \,. \tag{A.201}$$

With that, we can evaluate Eqn. (A.201) in two steps:

$$(I_{\text{fl}} \star I_{\text{fl}})(t) = \frac{1}{2\tau_l} e^{-\frac{|t|}{\tau_l}} \,, \tag{A.202}$$

and

$$(P * P)(t) = \frac{1}{2\tau_l} \frac{1}{2\sqrt{\pi}\sigma_t} e^{-\frac{t^2}{4\sigma_t^2}} \,. \tag{A.203}$$

Then, convolution yields

$$\tilde{\Pi}(\tau) = \frac{1}{4\tau_l} e^{\frac{\sigma_t^2 - \tau_l \tau}{\tau_l^2}} \left(1 + \operatorname{erf}\left(\frac{\tau}{2\sigma_t} - \frac{\sigma_t}{\tau_l}\right) + e^{\frac{2\tau}{\tau_l}} \operatorname{erfc}\left(\frac{\tau}{2\sigma_t} + \frac{\sigma_t}{\tau_l}\right)\right) \,. \tag{A.204}$$

For the next step, we obtain the degree of coherence for a single emission line as $|\gamma(\tau)| = e^{-\tau/(2\tau_l)}$. Therefore, we consider only the natural line width (FWHM) Γ_l (no collision broadening), and thus the lifetime is given as $\tau_l = \frac{\hbar}{\Gamma_l}$ (which is half the coherence time $\tau_c = \frac{2\hbar}{\Gamma_l}$).
Next, we calculate the partial visibility factor using Eqn. (3.98):

$$\beta_{\tilde{\text{P}},\text{Gauss}} = \int_{-\infty}^{\infty} \Pi(\tau) |\gamma(\tau)|^2 \, d\tau = \frac{1}{2\tau_l^2} \left(\frac{2\sigma_t \tau_l}{\sqrt{\pi}} + e^{\frac{\sigma_t^2}{\tau_l^2}} \left(\tau_l^2 - 2\sigma_t^2\right) \operatorname{erfc}\left(\frac{\sigma_t}{\tau_l}\right) \right) \,. \tag{A.205}$$

In contrast to the limits of $\beta_{\text{p,Gauss}}(\tau_c = 2\tau_l, T = 2\sqrt{\log(4)}\sigma_t)$ presented in Section 3.1.1, we obtain the following limits:

$$\begin{aligned}
&\lim_{\sigma_t \to 0} \beta_{\tilde{\text{P}},\text{Gauss}} = \lim_{\tau_l \to \infty} \beta_{\tilde{\text{P}},\text{Gauss}} = \frac{1}{2} \,, \\
&\lim_{\sigma_t \gg \tau_l} \beta_{\tilde{\text{P}},\text{Gauss}} = \frac{1}{\sqrt{\pi}} \frac{\tau_l}{\sigma_t} = \frac{2\sqrt{\log(4)}}{2\sqrt{\pi}} \frac{\tau_c}{T} \approx 0.66 \frac{\tau_c}{T} \,, \\
&\text{for comparison the results from Section 3.1.1:} \\
&\lim_{\sigma_t \to 0} \beta_{\text{p,Gauss}} = \lim_{\tau_l \to \infty} \beta_{\text{p,Gauss}} = 1 \,, \\
&\lim_{T \gg \tau_c} \beta_{\text{p,Gauss}} = \frac{1}{\sqrt{\pi}} \frac{\tau_l}{\sigma_t} = \frac{2\sqrt{\log(4)}}{2\sqrt{\pi}} \frac{\tau_c}{T} \approx 0.66 \frac{\tau_c}{T} \,.
\end{aligned} \tag{A.206}$$

Apparently, we have two contradicting models, where the one by Lohse et al. [74] (used in this work) assumes that only the time point of the (instantaneous) excitation matters, with the consequence that in the limit of infinite coherence time or a delta-like pulse shape the partial visibility factor β_{p} is always one. However, Inoue et al. [58] use a different model, where the different intensities (equally corresponding to the probability of decay) of the fluorescence over

[1] Fourier convolution theorem: $\mathfrak{F}[f * g] = \mathfrak{F}[f] \; \mathfrak{F}[g]$.
[2] Fourier cross-correlation theorem: $\mathfrak{F}[f \star g] = (\mathfrak{F}[f])^* \, \mathfrak{F}[g]$.

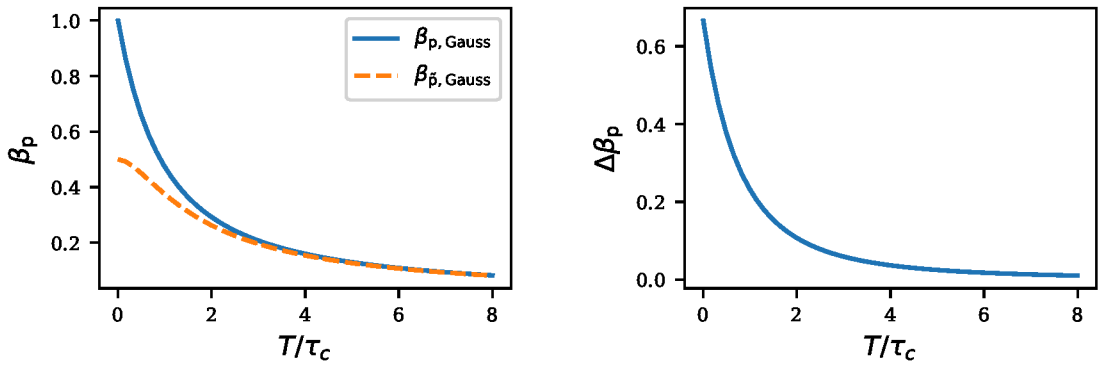

(a) (b)

Fig. A.3.: **(a)** Comparison between the model from Lohse et al. [74] $\beta_{\mathrm{p,Gauss}}$ and the model from Inoue et al. [58] $\beta_{\tilde{\mathrm{P}},\mathrm{Gauss}}$. **(b)** Relative difference $\Delta\beta_{\mathrm{p}}$, as defined in Eqn. (A.208).

time are considered. However, I would like to point out that in this case, that information is considered twice. That is because the degree of coherence $|\gamma(\tau)| = (\psi \star \psi)(\tau) / \int_{-\infty}^{\infty} \psi^*(t)\psi(t)\,dt$ does already encode the decaying envelope of the fluorescence wave function. This circumstance gets clear when we write the calculation of $\beta_{\tilde{\mathrm{p}}}$ in a more general way by substituting the degree of coherence with its definition:

$$\beta_{\tilde{\mathrm{p}}} = \int_{-\infty}^{\infty} \Big((P * |\psi|^2) \star (P * |\psi|^2) \Big)(\tau) \left| \frac{(\psi \star \psi)(\tau)}{\int_{-\infty}^{\infty} \psi^*(t)\psi(t)\,dt} \right|^2 d\tau\,. \tag{A.207}$$

However, the reader should note that both approaches return the same partial visibility factor in the long pulse limit ($T \gg \tau_c$). In fact, this convergence happens quite fast, as demonstrated in Fig. A.3a. To emphasize this, the normalized difference defined by

$$\Delta\beta_{\mathrm{p}} := \frac{\beta_{\mathrm{p,Gauss}} - \beta_{\tilde{\mathrm{P}},\mathrm{Gauss}}}{(1/2)(\beta_{\mathrm{p,Gauss}} + \beta_{\tilde{\mathrm{P}},\mathrm{Gauss}})}\,, \tag{A.208}$$

is plotted in Fig. A.3b. In the scope of this work, we stick to $\beta_{\mathrm{p,Gauss}}$, and since we are dealing with excitation pulses around an order of magnitude larger than the coherence time, this distinction is of no importance to the here presented results. However, this topic should be addressed in further research, as it might become more relevant with the advent of XFELs featuring attosecond pulses.

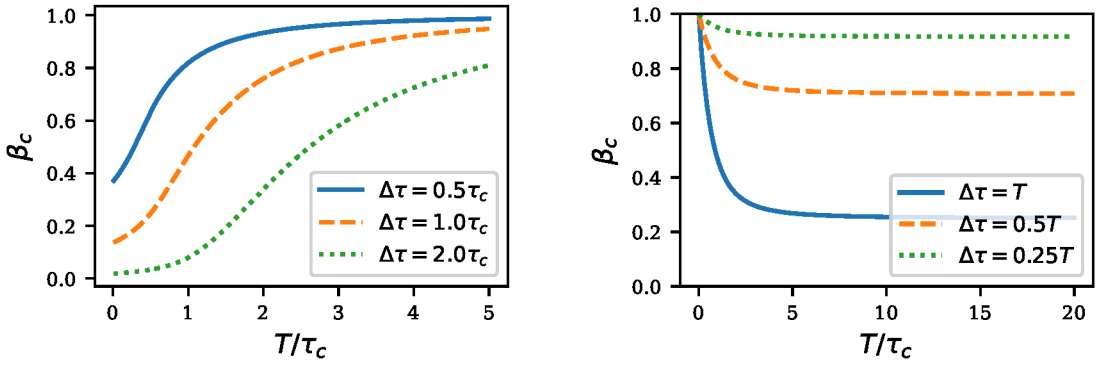

(a) (b)

Fig. A.4.: **(a)** β_c as a function of T/τ_c for different time delays $\Delta\tau$. **(b)** β_c as a function of T/τ_c, with the time delay proportional to T: $\Delta\tau = \eta T$

A.3.2 β_c – worst case estimation derivation

To derive the minimal partial visibility factor $\beta_c(\Delta\tau, T)$ as given in Eqn. (3.112), we start with Eqn. (3.111), where the assumption $\tau_1 \approx \tau_2$ is used. We further assume a Gaussian-shaped excitation pulse with an FWHM T to calculate $\Pi(\tau)$. With the calculated auto-correlation of the normalized excitation pulse $\Pi(\tau)$ (recall Eqn. (3.97)), we can evaluate the integrals in Eqn. (3.111) and obtain

$$\beta_c(\Delta\tau, \tau_c, T) = \frac{e^{-\frac{2\Delta\tau}{\tau_c}}\left(\operatorname{erfc}\left(\frac{T^2-\Delta\tau\,\tau_c\ln(4)}{T\tau_c\sqrt{\ln(4)}}\right) + e^{4\Delta\tau}\operatorname{erfc}\left(\frac{T^2-\Delta\tau\,\tau_c\ln(4)}{T\tau_c\sqrt{\ln(4)}}\right)\right)}{2\operatorname{erfc}\left(\frac{T}{\tau_c\sqrt{\ln(4)}}\right)}. \tag{A.209}$$

This β_c is plotted as a function of T/τ_c in Fig. A.4a for three different $\Delta\tau$. It is apparent that for longer excitation pulses (implying longer $\Delta\tau$), the size of the object becomes less relevant.
In the next step, we substitute the time delay by a variable proportional to the FWHM pulse duration $\Delta\tau = \eta\, T$ and plot $\beta_c(\eta T, \tau_c, T)$ as a function of T/τ_c in Fig. A.4b. Apparently, β_c first falls and then saturates at a value that is only dependent on η. To obtain this value, we calculate the limit

$$\lim_{T\to\infty} \beta_c(\Delta\tau = \eta T, \tau_c, T) = e^{-\ln(4)\eta^2}, \tag{A.210}$$

which turns out to be independent of τ_c. One can also show that this limit represents the lowest possible value of β_c for all T and τ_c:

$$\beta_c(\Delta\tau = \eta T, \tau_c, T) \geq e^{-\ln(4)\eta^2} \,\Big|\, \forall\, T, \tau_c\,. \tag{A.211}$$

After substituting $\eta = \Delta\tau/T$, we obtain Eqn. (3.112) ■.

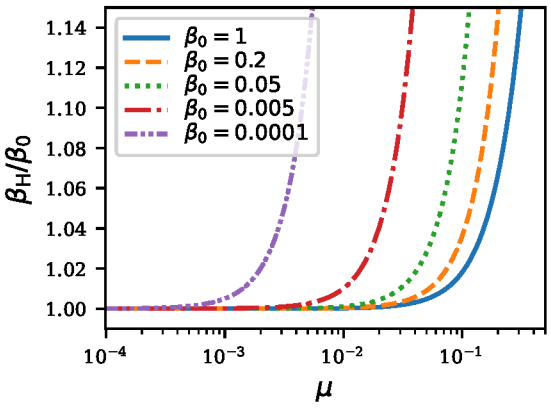

Fig. A.5.: Plot of the estimated speckle contrast β_H as a function of the mean counts. The approximation is worse, when the true speckle contrast β_0 is weaker. Note that this plot was already published in [122], but with a typo in the legend. The legend entry $\beta_0 = 0.001$ in [122] should read $\beta_0 = 0.0001$.

A.3.3 Further approximation of $\beta_{1,2}$

There are publications [54, 88, 115] that use a simplified shape of the $\beta_{1,2}$ speckle contrast estimation. Here[3], we shortly discuss their approximation and why we are not using it. The $\beta_{1,2}$ is approximated by neglecting values of three or more photons when estimating the mean photon count ($P_{\geq 3} = 0 \Rightarrow \langle I \rangle = P_1 + 2P_2$). Furthermore, a Taylor series expansion around $P_2 = 0$ yields

$$\beta_{1,2} \approx \frac{2(1-P_1)P_2}{P_1^2} - 1 + \mathcal{O}(P_2^2)\,. \tag{A.212}$$

For example, Hruszkewycz et al. [54] truncated that expansion to define an estimate,

$$\beta_H = \frac{2(1-P_1)P_2}{P_1^2} - 1\,. \tag{A.213}$$

We can calculate P_1 and P_2 directly from the negative binomial distribution (recall Eqn. (2.69))

$$\begin{aligned} P_1(\mu,\beta_0) &= \frac{\beta_0\mu(1+\beta_0\mu)^{-\frac{\beta_0\mu+1}{\beta_0}}\Gamma(1+\beta_0^{-1})}{\Gamma(\beta_0^{-1})}\,, \\ P_2(\mu,\beta_0) &= \frac{\beta_0^2\mu^2(1+\beta_0\mu)^{-\frac{\beta_0\mu+1}{\beta_0}}\Gamma(2+\beta_0^{-1})}{2\Gamma(\beta_0^{-1})}\,. \end{aligned} \tag{A.214}$$

Substituting this into Eqn. (A.213) yields

$$\beta_H(\mu,\beta_0) = (1+\beta_0)\left((1+\beta_0\mu)^{\mu+1/\beta_0} - \mu\right) - 1\,. \tag{A.215}$$

Plots of β_H Eqn. (A.215) normalized by the true visibility β_0 are shown in Fig. A.5. Although this estimate does not diverge at $\mu = 1$, as does $\beta_{1,2}$, it nevertheless becomes more inaccurate as μ increases to or over 1, for all values of β_0. The plot also reveals an undesired dependence of β_H on the true visibility β_0. Summing up, to me, it is not apparent what the advantage of this approach (β_H instead of $\beta_{1,2}$ or β_V) is, and therefore it is not used in the scope of this work.

[3]The content of this section was already published in [122].

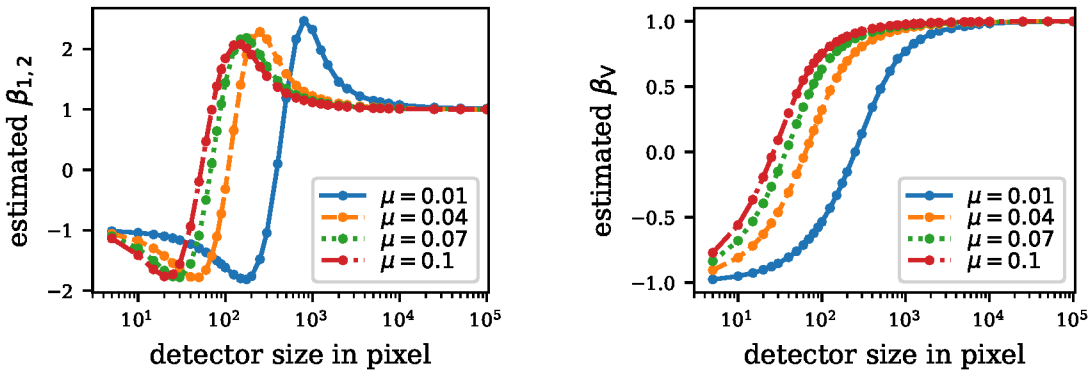

(a) (b)

Fig. A.6.: Influence of the detector size on the estimated speckle contrast using **(a)** $\beta_{1,2}$ and **(b)** β_V. For each μ a set of 5×10^8 randum numbers was generated that follow the Bose-Einstein distribution (of Eqn. (2.63)) and thus the true speckle contrast $\beta_0 = 1$. These plots have already been published in [122].

A.3.4 Influence of the detector size on speckle contrast estimation

Here[4] we discuss the influence of the number of detector pixels on the accuracy of speckle contrast estimation using the approaches introduced in Section 3.3 (recall Eqn. (3.128) and Eqn. (3.129)). The estimate $\beta_{1,2}$ requires that the probabilities for detecting one (P_1) or two photons (P_2), as well as the value of $\langle I \rangle$, can be estimated sufficiently independently. To illustrate the need for many pixels, consider the case of a two-pixel detector. Recall Eqn. (3.129): $\beta_{1,2} = (2P_2/\langle I \rangle - P_1)/(P_1 - P_2)$, it is impossible to obtain $\beta_{1,2} > 0$ because this would require either $(2P_2 > P_1\langle I \rangle) \wedge (P_1 > P_2)$ or $(P_1\langle I \rangle > 2P_2) \wedge (2P_2 > P_1)$; that can not work with only two pixels.

To further analyze the influence of the pixel count, we performed numerical simulations by generating sets of random numbers that follows the Bose-Einstein distribution (recall Eqn. (2.63)), which corresponds to $\beta_0 = 1$ with different expectation values μ for each set. Each set consisted of 5×10^8 numbers. The values in each set were then distributed into groups of equal sizes, corresponding to the number of detector pixels. The speckle contrast was individually evaluated for each of these 'detector frames' and averaged afterward to obtain an estimate of β_V or $\beta_{1,2}$. These estimates, plotted in Fig. A.6 as a function of the number of pixels (detector size), were obtained using the same total number of pixel readings since a smaller detector size gives more detector frames to average.

It is seen from Fig. A.6a that in the limit of detectors with few pixels, the contrast estimate approaches $\beta_{1,2} = -1$. The correct value is only obtained for pixel counts above about 10^4. We note two properties: First, for lower μ, more pixels are required in order to obtain an accurate estimate, and second, an insufficient pixel count can lead to an overestimation of the contrast ($\beta_{1,2} > \beta_0$). The same evaluation for β_V yields the result illustrated in Fig. A.6b. Also here, the limit of detectors with few pixels leads to an underestimation of β_V, but in contrast to the $\beta_{1,2}$ estimation, it converges monotonically to the true value as the pixel count increases.

[4]The content of this section was already published in [122].

A.3.5 Derivation of Var($\beta_{1,2}$)

In[5] order to calculate the variance of the $\beta_{1,2}$ speckle contrast estimate $\sigma^2_{\beta_{1,2}} := \mathrm{Var}(\beta_{1,2})$, we make use of the linear error propagation approximation [64], as given by

$$\mathrm{Var}[f(x_1,\ldots,x_n)] \approx \sum_{j=1}^{n} \left|\frac{\partial f}{\partial x_j}\right|^2 \sigma^2_{x_j}\,, \tag{A.216}$$

neglecting possible correlations between x_j and x_k for $j \neq k$. To obtain $\sigma^2_{\beta_{1,2}}$ we need $\sigma^2_{P_1}$, $\sigma^2_{P_2}$ and $\sigma^2_{\langle I\rangle}$. Therefore, we assume a sufficiently large detector, where sufficiently large means that P_1 and P_2 can be obtained acceptably independent from each other. A trivial negative example would be a one-pixel detector, where we have no chance of obtaining a one-photon and a two-photon hit within a single measurement. That might sound very obvious, but please note that our treatment requires that all P_j are independently measurable observables. Thus P_j is found simply by counting j-photon events and then dividing the count by the number of pixels $P_j = n_j/N_{\mathrm{Pix}}$. This is a counting process that satisfies the Poisson statistics [44], with $\sigma^2_{P_j} = P_j$ ($P_j(\mu,\beta) = P_{\mathrm{NB}}(j|\mu,\beta)$, recall Eqn. (2.69)), and therefore we obtain

$$\begin{aligned}\sigma^2_{P_1} &= \frac{\mu}{(1+\beta_0\mu)^{(1+\beta)/\beta}}\,,\\ \sigma^2_{P_2} &= \frac{1}{2}\frac{(1+\beta)\mu^2}{(1+\beta\mu)^{2+1/\beta}}\,.\end{aligned} \tag{A.217}$$

We have ignored the factor $1/N_{\mathrm{Pix}}$ since it is constant and applies equally to all terms. The expectation value μ is approximated by the mean photon count $\mu = \langle I\rangle$ and thus its variance is given by the variance of the negative binomial distribution (recall Eqn. (2.68))

$$\sigma^2_{\langle I\rangle} \approx \langle I\rangle + \beta\langle I\rangle^2\,. \tag{A.218}$$

Now Eqn. (A.216) can be applied to Eqn. (3.129), and we obtain

$$\sigma^2_{\beta_{1,2}} \approx \frac{(1+\beta)(1+\beta\langle I\rangle)}{(\langle I\rangle-1)^2\langle I\rangle^2}\left((1+\beta)\langle I\rangle + (2+\langle I\rangle+3\beta\langle I\rangle)(1+\beta\langle I\rangle)^{2+\beta^{-1}}\right)\,. \tag{A.219}$$

[5] The content of this section was already published in [122].

A.3.6 Derivation of Var(β_V)

Here[6] we derive σ_V^2 in an analogous way to Appendix A.3.5. Therefore, we express the mean number of counts as a function of the photon probability, which reads

$$\langle I \rangle = \sum_{j=0}^{\infty} j P_j \,, \tag{A.220}$$

and its variance

$$\mathrm{Var}(I) = \sum_{j=0}^{\infty} (j - \langle I \rangle)^2 P_j \,. \tag{A.221}$$

With this, we can write β_V (recall Eqn. (3.128)) as a function of $\{P_j\}$ as

$$\beta_V = \frac{\sum_{j=0}^{\infty} P_j \left(j - \left(\sum_{n=0}^{\infty} n P_n\right)\right)^2 - \sum_{j=0}^{\infty} j P_j}{\left(\sum_{j=0}^{\infty} j P_j\right)^2} \,. \tag{A.222}$$

As in Appendix A.3.5, we assume that all P_j follow Poisson statistics since they originate from countable observables, and thus the variance of β_V, in the linear error propagation approximation, is given by

$$\sigma_{\beta_V}^2 \approx \sum_{j=0}^{\infty} P_j \left| \frac{\partial \beta_V}{\partial P_j} \right|^2 \,. \tag{A.223}$$

To evaluate this equation, we need to differentiate Eqn. (A.222) with respect to all P_j. This can be done, and the result simplifies nicely to

$$\frac{\partial \beta_V}{\partial P_j} = \frac{(j-1)j - 2j(1+\beta\mu) + \mu^2}{\mu^3} \,. \tag{A.224}$$

Now we can express Eqn. (A.223) as a function of $\langle I \rangle \approx \mu$ and β,

$$\sigma_{\beta_V}^2 \approx \frac{2 + 2\beta^3 \langle I \rangle^2 + \beta^2 \langle I \rangle (4 + 3\langle I \rangle) + \beta(2 + 4\langle I \rangle)}{\langle I \rangle^2} \,. \tag{A.225}$$

[6] The content of this section was already published in [122].

A.4 SNR analysis

A.4.1 IDI simulation of 3D crystals

For the IDI simulations of three-dimensional crystals, we assume a 500×500-pixel detector with a pixel size of $100\mu\text{m} \times 100\mu\text{m}$, placed at a distance of $50\,\text{mm}$ from the sample. We consider a cubic crystal sample consisting of simple cubic unit-cells with a lattice constant of $a = 5\text{Å}$ and with one emitter per cell. Each snapshot pattern is simulated by generating a random phase $\phi = [0, 2\pi)$ for each emitter and mode. The combined scalar wave function arising from the emission of all emitters is calculated for each pixel, using the far field approximation and considering a wavelength of $\lambda = 2\text{Å}$. Furthermore, we neglect the quadratic decay of intensity with distance, equivalent to the assumption that each pixel covers an equal solid angle. This is done to keep μ constant on the detector so we can focus on investigating the effects of interest without unnecessary complexity. The wave function was evaluated on a grid of nine points that sub-divides each pixel to ensure an accurate representation of the recorded signal. The continuously-valued intensity for a pixel centered at $\vec{r}_{\text{pix}}$ therefore reads

$$I_{\text{c}}(\vec{r}_{\text{pix}}) = \frac{1}{9M} \sum_{m=1}^{M} \sum_{s=1}^{9} \left| \sum_{j=1}^{N_{\text{E}}} e^{i \frac{2\pi \vec{r}_{\text{pix},s} \cdot \vec{r}_j}{\lambda |\vec{r}_{\text{pix},s}|}} \right|^2 , \tag{A.226}$$

where $\vec{r}_{\text{pix},s}$ are the sampling positions within the pixel at $\vec{r}_{\text{pix}}$, and $M = \beta^{-1}$ is the number of mutually incoherent modes (this type of simulation only allows for an integer number of modes). The continuously-valued intensity I_{c} is then rescaled (according to the fraction of the pixels solid angle Ω, here assumed to be equal for all pixels, and the number of photons per emitter N_γ, to achieve a certain μ). After this scaling, a Poisson discretization is applied $I(\vec{r}_{\text{pix}}) = \text{PoissSampl}\left(\frac{\mu}{\langle I_{\text{c}} \rangle} I_{\text{c}}(\vec{r}_{\text{pix}})\right)$.
The auto correlation is calculated as follows

$$\text{AC}(\vec{q}) = \frac{1}{C(\vec{q})} \sum_{j=1}^{N_{\text{pix}}} \sum_{l=1}^{N_{\text{pix}}} I(\vec{r}_{\text{pix}),j} I(\vec{r}_{\text{pix}),l} \, \Upsilon \left(\frac{2\pi}{\lambda} (\vec{r}_{\text{pix},j} - \vec{r}_{\text{pix},l}), \vec{q} \right) , \tag{A.227}$$

where $\Upsilon(\vec{a}, \vec{b})$ is defined as a modified top hat function

$$\Upsilon(\vec{a}, \vec{b}) := \begin{cases} 1 \text{ for } |a_j - b_j| < \Delta\text{Vox}/2 \,|\, j = \{x, y, z\} \,, \\ 0 \text{ else} \,. \end{cases} \tag{A.228}$$

ΔVox represents the voxel edge size in a discretized $G^{(2)}$-space. The usage of Υ, therefore, represented a nearest-neighbor interpolation of $\vec{q}$. If we do not have a spherical 4π-detector, the number of possible realizations of $\vec{q}$ generally varies.

Therefore, we define the function $C(\vec{q})$ as the density of realizations, which reads

$$C(\vec{q}) = \frac{1}{C(\vec{q})} \sum_{j=1}^{N_{\text{pix}}} \sum_{l=1}^{N_{\text{pix}}} \Upsilon \left(\frac{2\pi}{\lambda} (\vec{r}_{\text{pix},j} - \vec{r}_{\text{pix},l}), \vec{q} \right) , \tag{A.229}$$

The $G^{(2)}$ is then obtained by averaging N_{P} patterns (independent auto correlations)

$$G^{(2)}(\vec{q}) = \langle \text{AC}(\vec{q}) \rangle_{N_{\text{P}}} = \frac{1}{N_{\text{P}}} \sum_{p=1}^{N_{\text{P}}} \text{AC}_p(\vec{q}) \, . \tag{A.230}$$

To obtain the variance of $G^{(2)}$, we perform the whole simulation twice, with exactly the same parameters (but with different realizations of the random phases), to obtain $G_1^{(2)}$ and $G_2^{(2)}$. The variance is then estimated by the $C(\vec{q})$-weighted, squared difference of these two auto-correlations:

$$\text{Var}_{\text{Sim3D}} = \frac{\sum_{j=1}^{N_{\text{Vox}}} \left(G_1^{(2)}(\vec{q}_j) - G_2^{(2)}(\vec{q}_j) \right)^2 C(\vec{q}_j)}{2 \sum_{j=1}^{N_{\text{Vox}}} C(\vec{q}_j)} \, . \tag{A.231}$$

It should be noted that we have used quite small crystals (starting from $5 \times 5 \times 5$ unit-cells) in our simulations. Therefore the Bragg peaks that arise in $G^{(2)}$ have non-negligible side maxima that are not easily distinguished from fluctuations in the offset. Fixed integration boundaries would therefore lead to the situation that the amount of side maxima contributions within the integration could vary. To avoid this, we chose to set the integration limits to the positions of the first-order minima $q_{\text{1st min}} = \pm 2\pi / (\sqrt[3]{N_{\text{E}}} a)$. Even so, the signal within this integration boundary is only proportional to N_{E} in the limit of large crystals. Therefore, we calculated peak weighting factors as[7]

$$\text{PWF}(N_{\text{E}}) = N_{\text{E}} \left(\int_{-\frac{2\pi}{\sqrt[3]{N_{\text{E}}} a}}^{\frac{2\pi}{\sqrt[3]{N_{\text{E}}} a}} \left| G_{\text{theo}}^{(1)}(\vec{q}, N_{\text{E}}) \right|^2 \, dq_x \, dq_y \, dq_z \right)^{-1} , \tag{A.232}$$

where $G_{\text{theo}}^{(1)}$ are the theoretically calculated Bragg peaks as given by Eqn. (4.158).

One remark on the auto-correlation: if one wants to evaluate data from a real experiment, the $C(\vec{q})$ should be calculated with an altered Eqn. (A.227)

$$C(\vec{q}) = \frac{1}{C(\vec{q})} \sum_{j=1}^{N_{\text{pix}}} \sum_{l=1}^{N_{\text{pix}}} \langle I(\vec{r}_{\text{pix}),j} \rangle_{N_{\text{P}}} \langle I(\vec{r}_{\text{pix}),l} \rangle_{N_{\text{P}}} \Upsilon \left(\frac{2\pi}{\lambda} (\vec{r}_{\text{pix},j} - \vec{r}_{\text{pix},l}), \vec{q} \right) , \tag{A.233}$$

where the photon count at a certain pixel $I(\vec{r}_{\text{pix}})$ is substituted by the over all pattern averaged photon count at that pixel $\langle I(\vec{r}_{\text{pix}),j} \rangle_{N_{\text{P}}}$. This takes care of systematic inhomogeneous intensity distributions among the pixels (detectors), as, for example, different solid angle overages per pixel, or constant biases.

[7] Please note, that there is a typo in [121], where it should read '$\left| G^{(1)}(\vec{q}, N_{\text{E}}) \right|^2$' instead of '$\left| G^{(1)}(\vec{q}, N_{\text{E}}) \right|$'.

A.4.2 IDI simulation of 2D objects

IDI simulations of two-dimensional objects were used for the analysis of non-crystalline, arbitrary samples. As with the simulations of crystals described in Appendix A.4.1, we assume a detector in the far field, but now the object's emission density is represented by a two-dimensional array of emission values, $\rho(x, y)$, instead of discrete emitters located at arbitrary coordinates. Each emission value of the object is assigned a random phase $\phi_m(x, y) = [0, 2\pi)$ per mode m. The continuously-valued scalar wavefield intensity, considering $M = \beta^{-1}$ mutually incoherent modes, is then proportional to

$$I_\mathrm{c}(k_x, k_y) = \sum_{m=1}^{M} \left| \mathrm{DFT}^{(2)}[\rho(x, y) e^{i\phi_m(x,y)}](k_x, k_y) \right|^2 , \tag{A.234}$$

making use of the 2D discrete Fourier transform $\mathrm{DFT}^{(2)}$. The continuous intensity is represented by a 2D array of the same size as $\rho(x, y)$. The intensity is then scaled to enforce a given mean pixel intensity μ, and a Poisson discretization is applied $I(k_x, k_y) = \mathrm{PoissSampl}\left(\frac{\mu}{\langle I_\mathrm{c} \rangle} I_\mathrm{c}(k_x, k_y)\right)$. The auto-correlation is performed using the Fourier-cross correlation theorem

$$\mathrm{AC}(q_x, q_y) = \mathrm{iDFT}^{(2)} \left[\left| \mathrm{DFT}^{(2)}[I(k_y, k_y)](\tilde{k}_x, \tilde{k}_y) \right|^2 \right] (q_x, q_y) , \tag{A.235}$$

where $\mathrm{iDFT}^{(2)}$ denotes the 2D inverse discrete Fourier transform. Contrary to the 3D case with a detector of limited solid angle, here, the full two-dimensional $\vec{k}$-space is covered. Therefore, $C(q_x, q_y) = N_\mathrm{pix}$ is constant. To quantify the *useable signal* and the variance of $G^{(2)}$, $|g^{(1)}|^2$, which is given by

$$\left| g^{(1)}(q_x, q_y) \right|^2 = \frac{\left| \mathrm{DFT}^{(2)}[\rho(x, y)](q_x, q_y) \right|^2}{\left| \mathrm{DFT}^{(2)}[\rho(x, y)](0, 0) \right|^2} , \tag{A.236}$$

can be used as 'ground truth'. The signal and background can now be obtained as fit parameters (S,O) with the best-fit model

$$G^{(2)}(q_x, q_y) = O + S \left| g^{(1)}(q_x, q_y) \right|^2 + \epsilon(q_x, q_y) . \tag{A.237}$$

Then, the variance is calculated by

$$\mathrm{Var}_\mathrm{Sim2D} = \frac{1}{N_\mathrm{pix}} \sum_{q_x, q_y}^{N_\mathrm{pix}} \left(O + S \left| g^{(1)}(q_x, q_y) \right|^2 - G^{(2)}(q_x, q_y) \right)^2 . \tag{A.238}$$

It should be noted that for the fitting, Eqn. (A.237) and the calculation of the variance Eqn. (A.238) the zero-frequency component $(q_x = q_y = 0)$ is ignored. This is done because this component follows a different statistic, as already discussed in Section 4.1.1.

A.4.3 Examples of the dependence of the variance of $g^{(2)}$ on the detector configuration and correlations within the offset term

In Section 4.1, the derivation of the variance of the autocorrelation, $\mathrm{Var}_{\mathrm{AC}}(\vec{q})$, depends upon the strong assumption that the counts measured at different detector pixels are uncorrelated. Since this assumption may seem quite unsatisfactory, here some problems are illustrated one has to face when dropping that assumption. Also, we demonstrate that increasing N_{P} does not have the same effect on the SNR as increasing $C(\vec{q})$ in the limit of large values.

Consider a simple one-dimensional array of emitters. The single emitters must be understood as thermal light sources which are so bright that the high-intensity limit $\mu \gg 1$ applies, and thus, we can neglect Poisson noise. This denotes the classical limit, where (X-ray) light is not treated as energy quanta (photons) but as continuous energies (integrated intensities). Please note that we discuss the limits of the theory presented in Section 4, and the inclusion of Poisson statistics would not solve the issues we are discussing here but instead certainly not make the situation less complicated in any way.

Two classical emitters – a thought experiment

As a first sample, we choose two emitters at the positions $r_1 = 0$ and $r_2 = R$. We further assume that the integrated intensity signals are measured with two independent detectors (or two detector pixels) at the positions $k_1 = 0$ and $k_2 = q$. The correlation product can then be written as[8]

$$\begin{aligned} I(k_1 = 0) \cdot I(k_2 = q) &= \sum_{j,j',l,l'=1}^{2} e^{ik_1(r_j - r_{j'})} e^{ik_2(r_l - r_{l'})} e^{i(\phi_j - \phi_{j'} + \phi_l - \phi_{l'})} \\ &= 4\left(\cos\left(\frac{qR}{2}\right) + \cos\left(\frac{qR}{2} - \phi_1 + \phi_2\right)\right)^2 . \end{aligned} \tag{A.239}$$

Next, we average over all possible realizations of the phases $\phi_j = [0, 2\pi)$, which is equivalent to an average over an infinite number of patterns $\langle I(k_1 = 0) \cdot I(k_2 = q)\rangle_{N_{\mathrm{P}}}$ to obtain $G^{(2)}(q)$ as

$$\begin{aligned} G^{(2)}(q) &= \frac{1}{(2\pi)^2} \int_0^{2\pi} \int_0^{2\pi} 4\left(\cos\left(\frac{qR}{2}\right) + \cos\left(\frac{qR}{2} - \phi_1 + \phi_2\right)\right)^2 d\phi_1\, d\phi_2 \\ &= 4 + 2\cos(qR) . \end{aligned} \tag{A.240}$$

It should be noted that the SOR of this equation neither corresponds to a TLS (see Eqn. (2.89)) nor to SPEs (see Eqn. (2.88)). However, these differences are not relevant to the SNR discussion since they vanish in the limit of a large number of emitters N_{E}, which is generally assumed in the scope of this work. However, because of the small number of emitters in this example, we are able to calculate the variance of $G^{(2)}(q)$ analytically by integrating over all possible

[8] Please note, that the equation (C1) in [121] is wrong and should be replaced by Eqn. (A.239). However equation (C2) in [121] is right and therefore, the conclusions are still valid.

combinations of the random phases. In general, for objects with N_E emitters (and therefore N_E random phases), the variance reads[9] in the two detector configuration:

$$\mathrm{Var}_{G^{(2)}}(q) = \frac{1}{(2\pi)^{N_\mathrm{E}}} \int_0^{2\pi} \dots \int_0^{2\pi} \left(G^{(2)}(q) - I(k_1 = 0, \{\phi\}) I(k_2 = q, \{\phi\}) \right)^2 d\{\phi\} \,. \tag{A.241}$$

For our two emitters object, we obtain the variance as

$$\mathrm{Var} = 18 + 16 \cos(qR) \,. \tag{A.242}$$

If we alter the situation to use more than two independent detectors – say, an infinite number of detector pixels in this thought experiment – covering the full relevant area from $q = 0$ to $q = 2\pi/R$, we can write the correlation as

$$\frac{R}{2\pi} \int_0^{\frac{2\pi}{R}} I(k, \phi_1, \phi_2) \cdot I(k+q, \phi_1, \phi_2) \, dk = 4 + 2\cos(qR) \,\Big|\, \forall \phi_1, \phi_2 \,. \tag{A.243}$$

That may not seem so surprising since, under the assumption of uncorrelated photon counts, more detector pixels (which implies a larger $C(q)$) could be seen as equivalent to more patterns, recall Eqn. (4.155). However, we will discuss in the next step, where we increase the number of emitters, that this assumption can not be maintained without loss of generality.

Three classical emitters – another thought experiment

In this step, we add an emitter to our sample so that it now contains three emitters with the positions $r_1 = 0$, $r_2 = R/2$, and $r_3 = R$. Then the $G^{(2)}(q)$ is given by

$$G^{(2)}(q) = 9 + 4\cos\left(\frac{qR}{2}\right) + 2\cos(qR) \,, \tag{A.244}$$

and plotted in Fig. A.7a. The variance, calculated using Eqn. (A.241) and assuming two detectors reads

$$\mathrm{Var}_{2\,\mathrm{detectors}}(q) = 88\cos(qR) + 176\cos\left(\frac{qR}{2}\right) + 8\cos\left(\frac{3}{2}qR\right) + 142 \,. \tag{A.245}$$

[9] Please note, there is a minor typo in equation (C3) of [121]: it should read $I(0, \{\phi\})$ instead of $I(0, \phi)$.

We can also calculate the *infinite* detector in analogy to Eqn. (A.243) and obtain[10]

$$\begin{aligned}\frac{R}{4\pi}\int_0^{\frac{4\pi}{R}} I(k,\phi_1,\phi_2,\phi_3)\cdot I(k+q,\phi_1,\phi_2,\phi_3)\,dk = 9 &+ 4\cos\left(\frac{qR}{2}\right) + 2\cos\left(qR\right)\\ &+ 2\cos\left(\frac{qR}{2} - \phi_1 + 1\phi_2 - \phi_3\right)\\ &+ 2\cos\left(\frac{qR}{2} + \phi_1 - 2\phi_2 + \phi_3\right).\end{aligned} \tag{A.246}$$

The different integration boundary to that of Eqn. (A.243) is required to sample the full diffraction information.

We see that, as opposed to the case in Eqn. (A.243), the single pattern measurement with the *infinite* detector is still dependent on the random phases. Therefore, averaging over pixels within a single pattern is not equivalent to averaging over more realizations of patterns with fewer pixels. In other words, the effect of the $C(\vec{q})$ on the SNR is limited.

After averaging over the random phases in Eqn. (A.246) we obtain the same result as in Eqn. (A.244), as expected. When calculating the variance, using Eqn. (A.241), we obtain

$$\mathrm{Var}_{\text{infinite detector}}(q) = 4 + 4\cos\left(qR\right). \tag{A.247}$$

This variance differs from that with only two independent detectors (recall Eqn. (A.242)) not only in terms of scaling but also in terms of its dependence on q, see Fig. A.7b. These differences originate from the fact that the intensity (counts) measurements within one pattern are not only correlated due to the emission structure of the object but also due to the fact that the terms that form the offset are correlated. This also leads to the situation that the maxima of the SNR, see Fig. A.7c, are not necessarily at the same q-positions as the maxima of $G^{(2)}(q)$.

[10] Please note, that in equation (C7) of [121] it should read '$I(k,\phi_1,\phi_2,\phi_3)\cdot I(k+q,\phi_1,\phi_2,\phi_3)$' instead of '$I(k,\phi_1,\phi_2)\cdot I(k+q,\phi_1,\phi_2)$'.

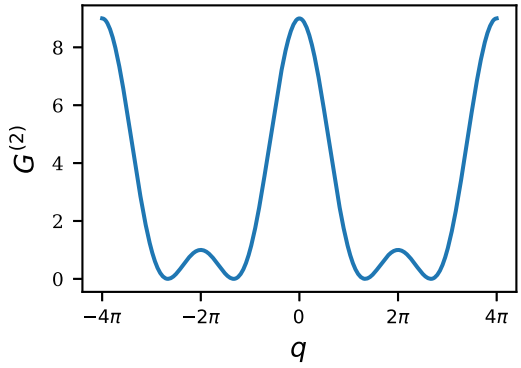

(a)

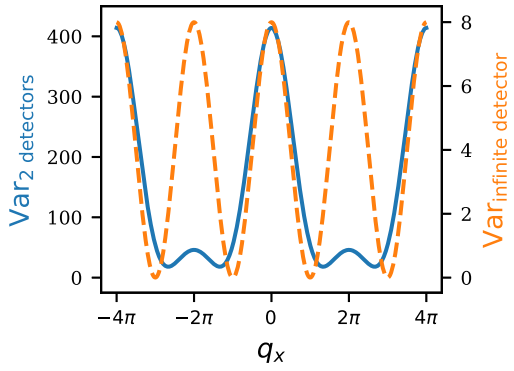

(b)

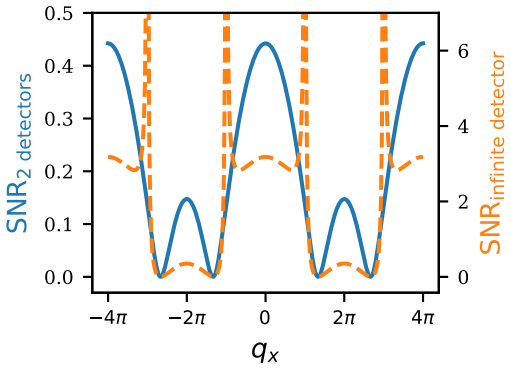

(c)

Fig. A.7.: One dimensional object consisting of three incoherent emitters, with a distance of 0.5. **(a)** $G^{(2)}(q)$ signal. **(b)** Variance of $G^{(2)}$ as a function of q for two detectors seperated by q (solid blue line) and for a 1D-detector of infinite sampling (dashed orange line), covering the full q-space. Note that there is not only a difference in scaling but also in the form of the variance. **(c)** SNR as a function of q for the same object and detector configurations as in (b). Note that for the 'infinite' detector the SNR maxima are not at the points of the maximal signal, see(a). These figures were already published in [121].

B Data Processing

B.1 Photonization of detector values (Jungfrau)

This process was already described in [122]. The data measured with a Jungfrau detector (in the scope of the experiment presented in Section 3.2) were calibrated as follows. We started with the pre-calibrated data provided by *psana* [15].

Dark calibration:
Instead of using dark runs, the noise peak of the histogram of data values was fitted for each pixel separately and used to generate maps of the dark noise (the so-called dark fields) for each run individually. This approach was possible since all recorded images were sparse (with photon counts $\ll 1$ per pixel). This dark calibration process is slightly better than measuring dark runs since the dark current drifts over time and thus may differ at the time of measurement of the dark run and the actual data.

Gain calibration:
Since we were only interested in the iron K_α-fluorescence at $6.4\,\mathrm{keV}$, the detection of different energies was minimized by using a manganese foil filter and a scattering angle where elastic scattering is minimal due to suppression by the polarization of the direct beam. We fitted the $6.4\,\mathrm{keV}$ peak for each pixel (using all available data) and calibrated each pixel (with the assumption that the Jungfrau detector behaves sufficiently linear) such that an ADU (arbitrary detector unit) value for one $6.4\,\mathrm{keV}$ photon was re-scaled to 1.0.

Largest adjacent pixel (LAP) photonization:
To take care of charge sharing and to assign an integer photon count for each pixel, we made use of a method we call *largest adjacent pixel* (LAP), which is equivalent to the *Psana Photon Converter* described by Sun et al. [115].

This method is presented as an example in Fig. B.1 on some arbitrary values, where Fig. B.1a represents the ground truth and Fig. B.1b the detector values (ADUs). In the first step, the value is split into whole (integer) numbers, see Fig. B.1c, and the remaining fractional values Fig. B.1d. Using the assumption that charge sharing only occurs between two adjacent pixels (sharing an edge), we select pixels above a certain value (here $x_{\text{seed}} = 0.5$) and combine each with their larges adjacent pixel, see Fig. B.1e. If the combined value exceeds a certain threshold (here $x_{\text{trh}} = 0.8$), the pixel is assigned a photon.

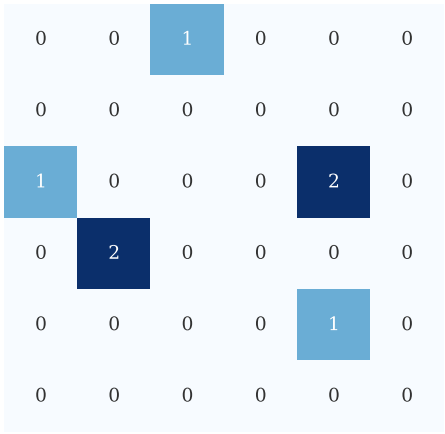

(a) ground truth

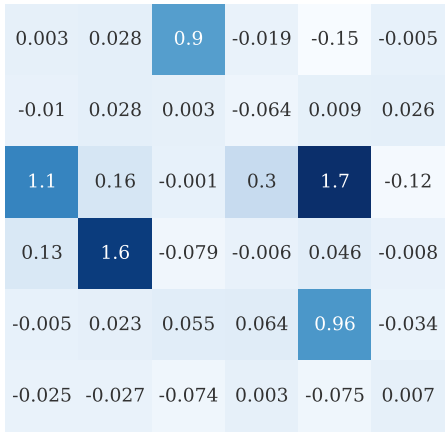

(b) calibrated ADUs

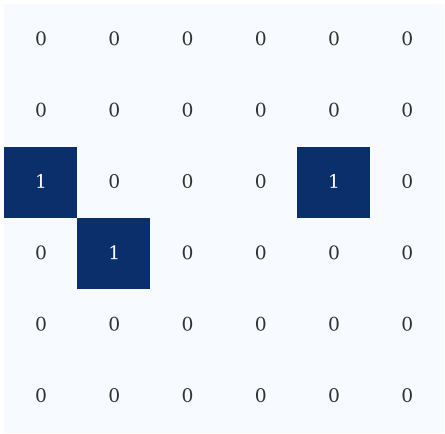

(c) full photons

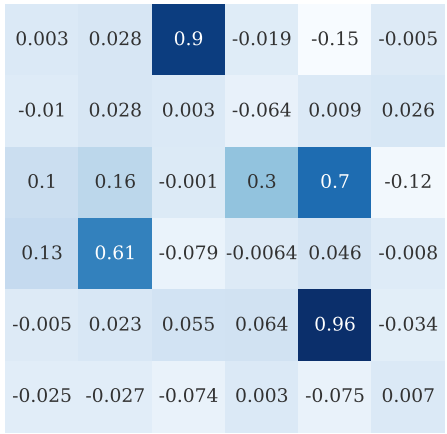

(d) fractional ADUs

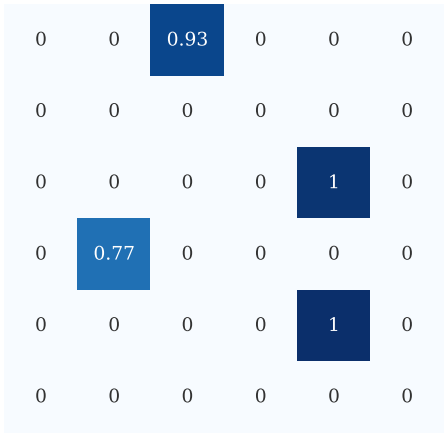

(e) combined ADUs

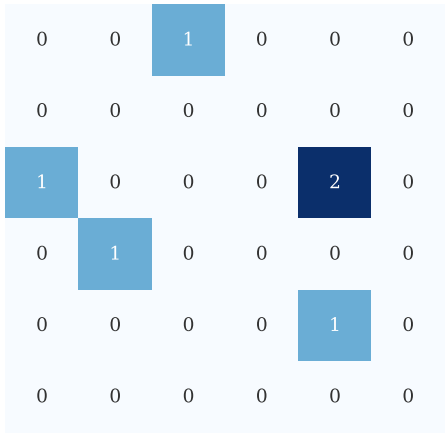

(f) reconstructed photons

Fig. B.1.: Illustration of the LAP algorithm, for details see text. This figure was already published in [122].

The advantages of this method are that it is fast (maximum linear run-time dependence on the photon count) and requires only two free parameters (x_{seed} and x_{trh}), and thus features great robustness. The disadvantage is that higher photon counts are underestimated in comparison with lower counts (as visible in the example).

B.2 Imaging demonstration experiment

B.2.1 Selection of 'good' frames

Due to the design of the experiment with the Cu foil and the detector in the forward direction, it was unavoidable that some amount of the direct beam passed through the foil. Recall the craters in the foil, shown in Fig. 5.2, and it gets clear that it also can happen that a crater is so big that the next XFEL pulse can partially pass through it. In those cases, a higher mean photon count in the center of the AGIPD detector is expected. Those frames, with an increased number of coherently scattered photons, needed to be rejected.

To identify these frames, the average photon count per pixel in the central part of the detector, see Fig. B.2a, $\langle I_{\text{central}} \rangle$, and the outer part, see Fig. B.2b, $\langle I_{\text{outer}} \rangle$ are computed. The discrimination value is then defined as

$$\mathfrak{d} := \frac{\langle I_{\text{central}} \rangle - \langle I_{\text{outer}} \rangle}{\langle I_{\text{outer}} \rangle} \,. \tag{B.248}$$

All frames with $|\mathfrak{d}| \geq 0.2$ were rejected – approximately $25\,\%$ of all recorded frames.
A possible strategy to increase the number of 'good' frames could be to choose a faster spinning speed of the disk (which was not possible here since the hardware limited the speed to $5000\,\text{rpm}$) or to use thicker foils to absorb more of the direct beam, but on the cost of a fluorescence intensity loss.

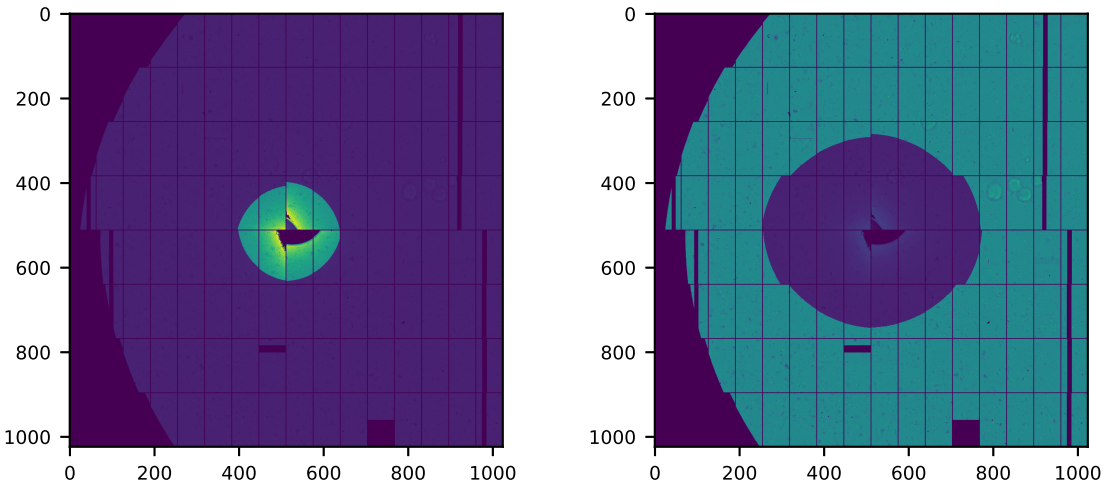

Fig. B.2.: **(a)** Central area of AGIPD detector. **(b)** Outer area of AGIPD detector. Note, that within this figure, the panels are not arranged according to the actual detector geometry.

B.2.2 Auto-correlation, Detector artifacts, and Pixel masking

The auto-correlation is normalized by the number of realizations, given for the corresponding (q_x, q_y)-position[1], by the so-called $C(q_x, q_y)$-map as introduced for the simulations in Eqn. (A.229). For experimental data, however, it is favorable to normalize by the auto-correlation of the averaged intensity since this will automatically take care of 'static' inhomogeneous features, such as static detector artifacts or shadows. The $C(q_x, q_y)$-map is obtained by

$$C(q_x, q_y) = \sum_{x,y} \langle I(x,y) \rangle_{x,y} \langle I(x+q_x, y+q_y) \rangle_{x,y} \,, \tag{B.249}$$

where $\langle I(x,y) \rangle_{x,y}$ is the average photon count of the pixel (x,y), and the sum goes over all possible pixels pairs with the position difference q_x and q_y. The auto-correlation is then given by

$$g^{(2)}(q_x, q_y) = \frac{1}{\mathcal{N}} \frac{\sum_{x,y} \langle I(x,y) I(x+q_x, y+q_y) \rangle_{x,y}}{C(q_x, q_y)} \,. \tag{B.250}$$

The scaling $\mathcal{N}$ is obtained by calculating the median of the $C(q_x, q_y)$ normalized auto-correlations in (q_x, q_y)-regions, where $g^{(2)}$ is expected to be unity (regions where no 'usable signal' is present, here $|q_{x,y}| > 30$). This is required since the individual frames (patterns) have different mean photon counts (recall Fig. 5.3b).

Even though the $C(q_x, q_y)$-normalization takes care of many intensity inhomogeneities and unwanted detector behavior, bad pixel masking is still necessary. Besides the obvious bad pixels (hot and cold pixels) and constant shadows, there were also some unwanted artifacts that randomly moved around. For example, on the entrance Kapton-window of the helium flight tube, some Cu was deposited over time, which was ablated from the Cu foil. Together with a, in terms of position, not perfectly stable beam, this caused small shadows to slowly and randomly

[1] In opposite to the main part, x, y as well as q_x, q_y are given in the unit of pixels here.

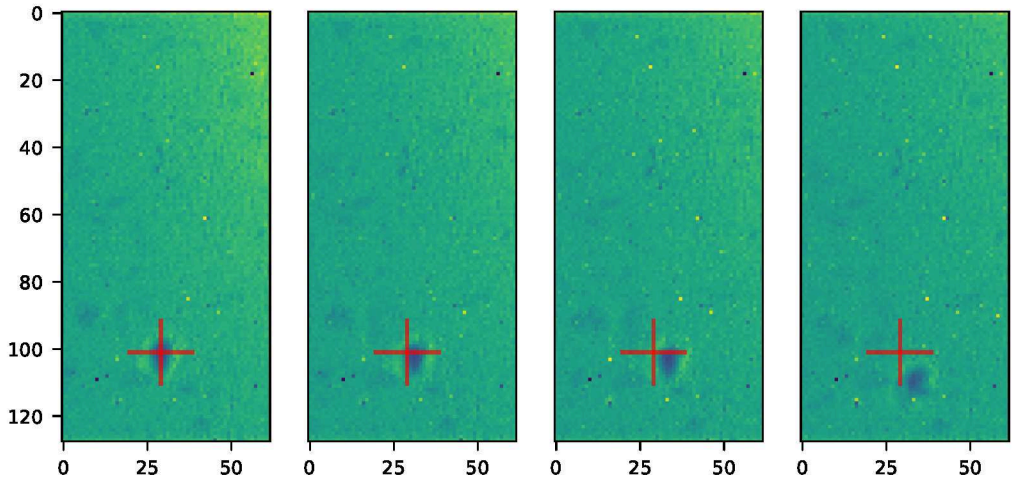

(a)

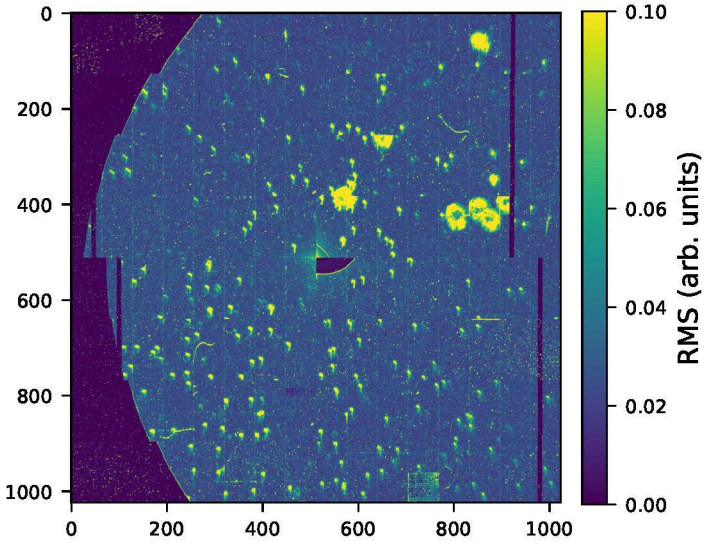

(b)

Fig. B.3.: **(a)** Moving shadows on the AGIPD (see red cross for reference). Averaged photon counts of approximately 750 000 frames at the same region. The displayed averages collected at intervals of 50 min. **(b)** RMS of averaged frames, used to improve pixel-masks.

move around; for example, see Fig. B.3a. These movements were used to improve the pixel masks by calculating the RMS of the averaged intensity. Therefore the photon count average over a certain number of frames is computed (in the presented case $N_\mathrm{P} \approx 750\,000$), and the RMS of 74 of such averaged intensities is displayed in Fig. B.3. The spots of high variance can easily be discerned and were used to improve the pixel-masks, ba applying appropriate thresholds.

B.2.3 Phase retrieval

An[2] image of the fluorescence emitter distribution was obtained by phasing the measured $|g^{(1)}(q_x, q_y)| = \sqrt{g^{(2)}(q_x, q_y) - 1}$ map (see Fig. 5.7a). The simplest iterative phase retrieval algorithm, *error reduction*, alternatively enforces the Fourier transform magnitude of the estimated image to be equal to $|F|(= |g^{(1)}|)$, and the structure to be smaller than a given size or within a shape called the 'support' [32]. Here, a variation of the *Shrinkwrap* algorithm [81] was used, in which the support region is determined from the N strongest pixels of a blurred version of the current iterate. The support was updated on each iteration. The number of pixels in the support was initially set to $N = 450$ pixels and the blurring utilized a Gaussian kernel with a RMS width σ that was initially set to 4 pixels. In addition, we constrained the real-space image $\rho(x, y)$ to be real and positive.

Starting with random Fourier phases, iterations alternated between *error reduction* and the *difference map* algorithms [26, 25]. This process was repeated 200 times during which the support area shrank to an area of $N = 300$ pixels, and the Gaussian smoothing kernel size shrank to $\sigma = 0.25$ pixels. The *difference map* algorithm avoids local minima using a combination of constraint operations that reaches a fixed point at the solution [26]. To further reduce the possibility of local minima, the *hybrid input-output* algorithm [32] was used in the iterations 25,50,75,100, and 125.

In Fig. B.4a the normalized RMS error [31] is plotted as a function of iterations for 5 randomly chosen phase retrievals. The metric is defined by

$$E_n^2 = \frac{\sum_{q_x,q_y} |f_n(q_x, q_y) - |F(q_x, q_y)||^2}{\sum_{q_x,q_y} |F(q_x, q_y)|^2}, \tag{B.251}$$

where f_n denotes the Fourier amplitudes of the n^{th} iterate and $|F| = |g^{(1)}|$ the measured amplitudes.

In the presence of noise, a reliable image estimate can be obtained by averaging many trials of the above described procedure [110]. For the present evaluation 1000 of such estimates where computed, each from a different random start. The used real-space operation of selecting the 450 strongest pixels does neither constrain the position of the structure, nor does it distinguish between an image and its centrosymmetric inverse. Therefore each estimation was brought into a common alignment and orientation by correlating to a reference estimate prior to averaging [31]. To demonstrate the convergence, the standard deviation archived for different numbers of averages was determined. Fifty sets of real-space image estimates were computed and in each set n of these estimates were averaged, to return the averages $\langle \rho_m(x, y) \rangle_n$ (with $m = [1, 50]$). The normalized standard deviation σ_n is then defined by

$$\sigma_n^2 = \frac{\sum_{x,y} \frac{1}{50} \sum_{m=1}^{50} |\langle \rho_m(x, y) \rangle_n - \langle \rho_m(x, y) \rangle_{n,m}|^2}{\sum_{x,y} |\langle \rho_m(x, y) \rangle_{n,m}|^2}, \tag{B.252}$$

where $\langle \rho_m(x, y) \rangle_{n,m}$ denotes the average of all 50 averaged images. This normalized standard deviation is plotted in Fig. B.4b as a function of the number of averages n.

[2] The content of this section was already published in [123].

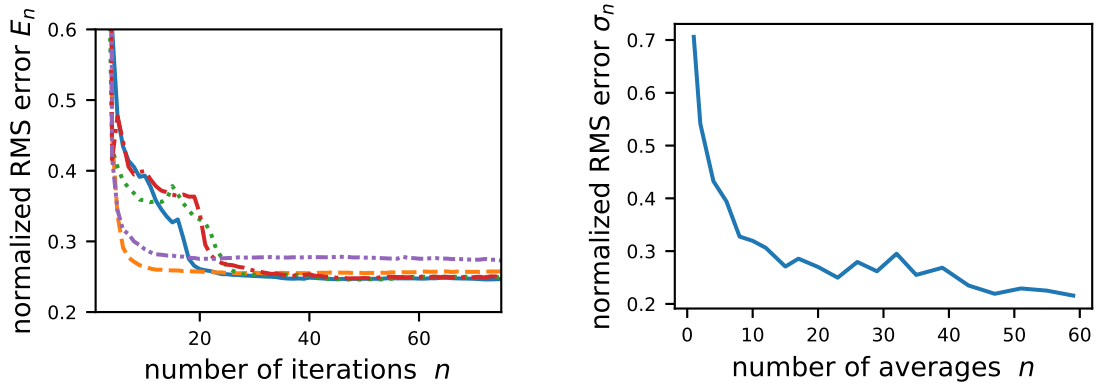

(a) (b)

Fig. B.4.: **(a)** Normalized RMS error as a function of iterations for 5 randomly chosen retrievals. **(b)** Normalized standard deviation of the average of individual iterates, defined by Eqn. (B.252). These figures were already published in [123].

Bibliography

[1] Aschkan Allahgholi, Julian Becker, Annette Delfs, et al. „The Adaptive Gain Integrating Pixel Detector at the European XFEL“. In: *Journal of Synchrotron Radiation* 26.1 (Jan. 2019), pp. 74–82 (cit. on pp. 73, 74).

[2] A. Aquila, A. Barty, C. Bostedt, et al. „The linac coherent light source single particle imaging road map“. In: *Structural Dynamics* 2.4 (2015), p. 041701 (cit. on p. 84).

[3] Kartik Ayyer, P. Lourdu Xavier, Johan Bielecki, et al. „3D diffractive imaging of nanoparticle ensembles using an x-ray laser“. In: *Optica* 8.1 (Jan. 2021), pp. 15–23 (cit. on pp. 84, 85).

[4] Niels Bohr. „I. On the constitution of atoms and molecules“. In: *The London, Edinburgh, and Dublin Philosophical Magazine and Journal of Science* 26.151 (1913), pp. 1–25 (cit. on p. 21).

[5] Max Born. „Quantenmechanik der Stoßvorgänge“. In: *Zeitschrift für Physik* 38.11-12 (Nov. 1926), pp. 803–827 (cit. on p. 9).

[6] Max Born and Emil Wolf. *Principles of optics: electromagnetic theory of propagation, interference and diffraction of light*. Elsevier, 2013 (cit. on pp. 5, 6).

[7] William Lawrence Bragg. „The structure of some crystals as indicated by their diffraction of X-rays“. In: *Proceedings of the Royal Society of London. Series A, Containing Papers of a Mathematical and Physical Character* 89.610 (Sept. 1913), pp. 248–277 (cit. on p. 1).

[8] A. Brunetti, M. Sanchez del Rio, B. Golosio, A. Simionovici, and A. Somogyi. „A library for X-ray–matter interaction cross sections for X-ray fluorescence applications“. In: *Spectrochimica Acta Part B: Atomic Spectroscopy* 59.10 (2004). 17th International Congress on X-Ray Optics and Microanalysis, pp. 1725–1731 (cit. on p. 77).

[9] Sebastian Cardoch, Fabian Trost, Howard A. Scott, et al. „Decreasing ultrafast x-ray pulse durations with saturable absorption and resonant transitions“. In: *Phys. Rev. E* 107 (1 Jan. 2023), p. 015205 (cit. on p. 43).

[10] Henry N. Chapman, Anton Barty, Stefano Marchesini, et al. „High-resolution ab initio three-dimensional x-ray diffraction microscopy“. In: *JOSA A* 23.5 (2006), pp. 1179–1200 (cit. on p. 1).

[11] Pieter Hendrik van Cittert. „Die wahrscheinliche Schwingungsverteilung in einer von einer Lichtquelle direkt oder mittels einer Linse beleuchteten Ebene“. In: *Physica* 1.1-6 (1934), pp. 201–210 (cit. on p. 15).

[12] Anton Classen. „Enhancing x-ray diractive imaging andoptical microscopy by use of intensity correlations“. PhD thesis. Friedrich-Alexander-Universität Erlangen-Nürnberg, 2019 (cit. on pp. 20, 27).

[13]Anton Classen, Kartik Ayyer, Henry N. Chapman, Ralf Röhlsberger, and Joachim von Zanthier. „Incoherent Diffractive Imaging via Intensity Correlations of Hard X Rays“. In: *Phys. Rev. Lett.* 119 (5 July 2017), p. 053401 (cit. on pp. 27, 33, 85).

[14]Jean le Rond d'Alembert. „Recherches sur la courbe que forme une corde tendue mise en vibration“. In: *Memoires de l'Academie royale des sciences et belles lettres. Classe de mathematique.* (1747) (cit. on p. 6).

[15]D. Damiani, M. Dubrovin, I. Gaponenko, et al. „Linac Coherent Light Source data analysis using *psana*“. In: *Journal of Applied Crystallography* 49.2 (Apr. 2016), pp. 672–679 (cit. on p. 107).

[16]Mehdi Delkhosh, Mohammad Delkhosh, and Mohsen Jamali. „Green's Function and its Applications“. In: *Journal of Basic and Applied Scientific Research* 2012 (Sept. 2012), pp. 8865–8876 (cit. on p. 9).

[17]Paul Adrien Maurice Dirac. „A new notation for quantum mechanics“. In: 35.3 (1939), pp. 416–418 (cit. on p. 16).

[18]Paul Adrien Maurice Dirac. „The principles of quantum mechanics“. In: 27 (1981) (cit. on p. 2).

[19]Dainis Dravins, Stephan LeBohec, Hannes Jensen, Paul D. Nuñez, CTA Consortium, et al. „Optical intensity interferometry with the Cherenkov Telescope Array“. In: *Astroparticle Physics* 43 (2013), pp. 331–347 (cit. on p. 66).

[20]Dravins, Dainis, Lagadec, Tiphaine, and Nuñez, Paul D. „Long-baseline optical intensity interferometry - Laboratory demonstration of diffraction-limited imaging“. In: *A&A* 580 (2015), A99 (cit. on pp. 58, 66).

[21]Gregor Drummen. „Fluorescent Probes and Fluorescence (Microscopy) Techniques — Illuminating Biological and Biomedical Research“. In: *Molecules* 17.12 (Nov. 2012), pp. 14067–14090 (cit. on p. 37).

[22]E. Duee, E. Fanchon, J. Vicat, et al. *REFINED CRYSTAL STRUCTURE OF THE 2[4FE-4S] FERREDOXIN FROM CLOSTRIDIUM ACIDURICI AT 1.84 ANGSTROMS RESOLUTION*. Aug. 1994 (cit. on p. 28).

[23]Martin Egli, Valentina Tereshko, Marianna Teplova, et al. „X-ray crystallographic analysis of the hydration of A-and B-form DNA at atomic resolution“. In: *Biopolymers: Original Research on Biomolecules* 48.4 (1998), pp. 234–252 (cit. on p. 1).

[24]H. Ekstein. „Connection between the kinematic and dynamical theories of X-ray diffraction“. In: *Physical Review* 62.5-6 (1942), p. 255 (cit. on p. 9).

[25]V. Elser, I. Rankenburg, and P. Thibault. „Searching with iterated maps“. In: *Proceedings of the National Academy of Sciences* 104.2 (2007), pp. 418–423 (cit. on p. 112).

[26]Veit Elser. „Phase retrieval by iterated projections“. In: *J. Opt. Soc. Am. A* 20.1 (Jan. 2003), pp. 40–55 (cit. on p. 112).

[27]Paul P. Ewald. „Die Berechnung optischer und elektrostatischer Gitterpotentiale“. In: *Annalen der physik* 369.3 (1921), pp. 253–287 (cit. on p. 27).

[28]Paul Peter Ewald. *Fifty Years of X-Ray Diffraction Dedicated to the International Union of Crystallography on the Occasion of the Commemoration Meeting in Munich July 1962*. Springer, 1962 (cit. on p. 79).

[29]Ugo Fano. „Quantum theory of interference effects in the mixing of light from phase-independent sources“. In: *American Journal of Physics* 29.8 (1961), pp. 539–545 (cit. on p. 2).

[30]Artur Feld, Agnes Weimer, Andreas Kornowski, et al. „Chemistry of Shape-Controlled Iron Oxide Nanocrystal Formation“. In: *ACS Nano* 13.1 (2019). PMID: 30540436, pp. 152–162 (cit. on p. 43).

[31]James R. Fienup. „Invariant error metrics for image reconstruction“. In: *Applied optics* 36.32 (1997), pp. 8352–8357 (cit. on p. 112).

[32]James R. Fienup. „Phase retrieval algorithms: a comparison“. In: *Appl. Opt.* 21.15 (Aug. 1982), pp. 2758–2769 (cit. on p. 112).

[33]L.B. Fletcher, H.J. Lee, T. Döppner, et al. „Ultrabright X-ray laser scattering for dynamic warm dense matter physics“. In: *Nature photonics* 9.4 (2015), pp. 274–279 (cit. on p. 85).

[34]Danuta Frackowiak. „The Jablonski diagram“. In: *Journal of Photochemistry and Photobiology B: Biology* 2.3 (1988), p. 399 (cit. on p. 32).

[35]Hideya Gamo. „Triple correlator of photoelectric fluctuations as a spectroscopic tool“. In: *Journal of Applied Physics* 34.4 (1963), pp. 875–876 (cit. on p. 85).

[36]Marco Genovese. „Real applications of quantum imaging“. In: *Journal of Optics* 18.7 (2016), p. 073002 (cit. on p. 85).

[37]Carmelo Giacovazzo, Hugo Luis Monaco, Gilberto Artioli, et al. *Fundamentals of crystallography*. 2011 (cit. on p. 10).

[38]Roy J. Glauber. „Coherent and incoherent states of the radiation field“. In: *Physical Review* 131.6 (1963), p. 2766 (cit. on pp. 17, 18).

[39]Roy J. Glauber. „The Quantum Theory of Optical Coherence“. In: *Physical Review* 130.6 (June 1963), pp. 2529–2539 (cit. on p. 2).

[40]Joseph W. Goodman. *Introduction to Fourier Optics*. en. 2nd ed. McGraw-Hill series in electrical and computer engineering. Electromagnetics. London, England: McGraw-Hill Publishing, Mar. 1996 (cit. on pp. 5, 8).

[41]Joseph W. Goodman. *Statistical Optics (Wiley Series in Pure and Applied Optics)*. Wiley-Interscience, 1985 (cit. on pp. 5, 11, 14, 15, 33, 34, 39).

[42]Leo A. Goodman. „On the Exact Variance of Products“. In: *Journal of the American Statistical Association* 55.292 (1960), pp. 708–713 (cit. on p. 58).

[43]George Green. *An Essay on the Application of mathematical Analysis to the theories of Electricity and Magnetism*. Vol. 1854. 47. De Gruyter, 1854, pp. 161–221 (cit. on p. 9).

[44]F.A. Haight. *Handbook of the Poisson Distribution*. Operations Research Society of America. Publications in operations research. Wiley, 1967 (cit. on p. 97).

[45]Robert Hanbury Brown. „Measurement of Stellar Diameters“. In: *Annual Review of Astronomy and Astrophysics* 6.1 (Sept. 1968), pp. 13–38 (cit. on pp. 58, 66).

[46]Robert Hanbury Brown and Richard Q. Twiss. „A test of a new type of stellar interferometer on Sirius“. In: *Nature* 178 (1956), pp. 1046–1048 (cit. on pp. 2, 58).

[47]Robert Hanbury Brown and Richard Q. Twiss. „Correlation between Photons in two Coherent Beams of Light“. In: *Nature* 177.4497 (Jan. 1956), pp. 27–29 (cit. on pp. 2, 12).

[48]Robert Hanbury Brown and Richard Q. Twiss. „Interferometry of the intensity fluctuations in light-I. Basic theory: the correlation between photons in coherent beams of radiation“. In: *Proceedings of the Royal Society of London. Series A. Mathematical and Physical Sciences* 242.1230 (1957), pp. 300–324 (cit. on p. 72).

[49]Robert Hanbury Brown and Richard Q. Twiss. „Interferometry of the intensity fluctuations in light. II. An experimental test of the theory for partially coherent light“. In: *Proceedings of the Royal Society of London. Series A. Mathematical and Physical Sciences* 243.1234 (1958), pp. 291–319 (cit. on p. 72).

[50]Robert Hanbury Brown and Richard Q. Twiss. „LXXIV. A new type of interferometer for use in radio astronomy“. In: *The London, Edinburgh, and Dublin Philosophical Magazine and Journal of Science* 45.366 (July 1954), pp. 663–682 (cit. on pp. 2, 12).

[51]Eugene Hecht. *Optics*. Old Tappan: Pearson Education, Incorporated, 2017 (cit. on p. 11).

[52]Burton L. Henke, Eric M. Gullikson, and John C. Davis. „X-ray interactions: photoabsorption, scattering, transmission, and reflection at E= 50-30,000 eV, Z= 1-92“. In: *Atomic data and nuclear data tables* 54.2 (1993), pp. 181–342 (cit. on p. 44).

[53]Phay J. Ho, Christopher Knight, and Linda Young. „Fluorescence intensity correlation imaging with high spatial resolution and elemental contrast using intense x-ray pulses“. In: *Structural Dynamics* 8.4 (July 2021), p. 044101 (cit. on pp. 2, 28, 85).

[54]S.O. Hruszkewycz, M. Sutton, P.H. Fuoss, et al. „High contrast x-ray speckle from atomic-scale order in liquids and glasses“. In: *Physical review letters* 109.18 (2012), p. 185502 (cit. on pp. 46, 95).

[55]Nelson Hua, Ivan A. Zaluzhnyy, Stjepan B. Hrkac, Anatoly G. Shabalin, and Oleg G. Shpyrko. „Extracting contrast in an X-ray speckle visibility spectroscopy experiment under imperfect conditions“. In: *Journal of Synchrotron Radiation* 27.6 (2020), pp. 1626–1632 (cit. on p. 46).

[56]Christiaan Huygens. *Traite de la lumiere: Où sont expliquées les causes de ce qui luy arrive dans la reflexion, & dans la refraction. Et particulierement dans l'etrange refraction du cristal d'Islande*. chez Pierre vander Aa, 1885 (cit. on p. 6).

[57]Ichiro Inoue, Yuichi Inubushi, Taito Osaka, et al. „Shortening X-Ray Pulse Duration via Saturable Absorption“. In: *Physical Review Letters* 127.16 (2021), p. 163903 (cit. on p. 43).

[58]Ichiro Inoue, Kenji Tamasaku, Taito Osaka, Yuichi Inubushi, and Makina Yabashi. „Determination of X-ray pulse duration via intensity correlation measurements of X-ray fluorescence“. In: *Journal of Synchrotron Radiation* 26.6 (Nov. 2019), pp. 2050–2054 (cit. on pp. 2, 33, 41, 91–93).

[59]G.E.M. Jauncey. „A Corpuscular Quantum Theory of the Scattering of Polarized X-rays“. In: *Physical Review* 23.3 (1924), p. 313 (cit. on p. 28).

[60]A. Kahoul, A. Abassi, B. Deghfel, and M. Nekkab. „K-shell fluorescence yields for elements with $6 \leq Z \leq 99$“. In: *Radiation Physics and Chemistry* 80.3 (2011), pp. 369–377 (cit. on p. 21).

[61]Franz X. Kärtner, Frederike Ahr, A.-L. Calendron, et al. „AXSIS: Exploring the frontiers in attosecond X-ray science, imaging and spectroscopy“. In: *Nuclear Instruments and Methods in Physics Research Section A: Accelerators, Spectrometers, Detectors and Associated Equipment* 829 (2016), pp. 24–29 (cit. on p. 2).

[62]J.C. Kendrew, G. Bodo, H.M. Dintzis, et al. „A Three-Dimensional Model of the Myoglobin Molecule Obtained by X-Ray Analysis“. In: *Nature* 181.4610 (Mar. 1958), pp. 662–666 (cit. on p. 1).

[63]Kwang-Je Kim. „An analysis of self-amplified spontaneous emission“. In: *Nuclear Instruments and Methods in Physics Research Section A: Accelerators, Spectrometers, Detectors and Associated Equipment* 250.1-2 (1986), pp. 396–403 (cit. on p. 51).

[64]James Kirchner. „Data analysis toolkit# 5: uncertainty analysis and error propagation“. In: *University of California Berkeley Seismological Laboratory. Available online at: http://seismo.berkeley.edu/~kirchner/eps_120/Toolkits/Toolkit_05.pdf* (2001) (cit. on p. 97).

[65]Juraj Knoška, Luigi Adriano, Salah Awel, et al. „Ultracompact 3D microfluidics for time-resolved structural biology“. In: *Nature communications* 11.1 (2020), pp. 1–12 (cit. on p. 43).

[66]M.O. Krause. „Atomic radiative and radiationless yields for K and L shells“. In: *Journal of Physical and Chemical Reference Data* 8.2 (Apr. 1979), pp. 307–327 (cit. on p. 77).

[67]M.O. Krause and J.H. Oliver. „Natural widths of atomic K and L levels, $K\alpha$ X-ray lines and several KLL Auger lines“. In: *Journal of Physical and Chemical Reference Data* 8.2 (Apr. 1979), pp. 329–338 (cit. on pp. 2, 22, 23, 45).

[68]Patrick Krejcik, F.J. Decker, Y. Ding, et al. „Commissioning the new LCLS X-band transverse deflecting cavity with femtosecond resolution“. In: *Proceedings of IBIC2013, Oxford, UK* (2013) (cit. on p. 43).

[69]Max von Laue. „Concerning the detection of X-ray interferences“. In: *Nobel lecture* 13 (1915) (cit. on p. 1).

[70]Michael Leitner, Bogdan Sepiol, Lorenz-Mathias Stadler, Bastian Pfau, and Gero Vogl. „Atomic diffusion studied with coherent X-rays“. In: *Nature materials* 8.9 (2009), pp. 717–720 (cit. on p. 83).

[71]P.G. Lenhert. „The structure of vitamin B12-VII. The X-ray analysis of the vitamin B12 coenzyme“. In: *Proceedings of the Royal Society of London. Series A. Mathematical and Physical Sciences* 303.1472 (1968), pp. 45–84 (cit. on p. 1).

[72]Jie Li, Xiaoming Ren, Yanchun Yin, et al. „53-attosecond X-ray pulses reach the carbon K-edge“. In: *Nature communications* 8.1 (2017), p. 186 (cit. on p. 2).

[73]Xavier Llopart, Jerome Alozy, Rafael Ballabriga, et al. „Timepix4, a large area pixel detector readout chip which can be tiled on 4 sides providing sub-200 ps timestamp binning“. In: *Journal of Instrumentation* 17.01 (2022), p. C01044 (cit. on pp. 2, 31).

[74]Leon M. Lohse, Malte Vassholz, and Tim Salditt. „On incoherent diffractive imaging“. In: *Acta Crystallographica Section A* 77.5 (Sept. 2021), pp. 480–496 (cit. on pp. 33, 38, 91–93).

[75]R. Loudon. „The Quantum Theory of Light“. In: (2000) (cit. on p. 5).

[76]Ivette J. Bermúdez Macias, Stefan Düsterer, Rosen Ivanov, et al. „Study of temporal, spectral, arrival time and energy fluctuations of SASE FEL pulses“. In: *Opt. Express* 29.7 (Mar. 2021), pp. 10491–10508 (cit. on p. 35).

[77]Anders Madsen, Jörg Hallmann, Gabriele Ansaldi, et al. „Materials imaging and dynamics (MID) instrument at the European X-ray Free-Electron Laser Facility“. In: *Journal of Synchrotron Radiation* 28.2 (2021), pp. 637–649 (cit. on p. 73).

[78]Leonard Mandel. „Fluctuations of photon beams: the distribution of the photo-electrons“. In: *Proceedings of the Physical Society* 74.3 (1959), p. 233 (cit. on p. 11).

[79]Leonard Mandel and Emil Wolf. *Optical Coherence and Quantum Optics*. Cambridge: Cambridge University Press, 1995 (cit. on p. 5).

[80]Leonard Mandel and Emil Wolf. „The measures of bandwidth and coherence time in optics“. In: *Proceedings of the Physical Society* 80.4 (1962), p. 894 (cit. on p. 11).

[81]Stefano Marchesini, H. He, Henry N. Chapman, et al. „X-ray image reconstruction from a diffraction pattern alone“. In: *Physical Review B* 68.14 (2003), p. 140101 (cit. on pp. 79, 112).

[82]Valerio Mariani, Andrew Morgan, Chun Hong Yoon, et al. „*OnDA*: online data analysis and feedback for serial X-ray imaging“. In: *Journal of Applied Crystallography* 49.3 (June 2016), pp. 1073–1080 (cit. on p. 44).

[83]James Clerk Maxwell. „VIII. A dynamical theory of the electromagnetic field“. In: *Philosophical Transactions of the Royal Society of London* 155 (Dec. 1865), pp. 459–512 (cit. on p. 5).

[84]Brian W.J. McNeil and Neil R. Thompson. „X-ray free-electron lasers“. In: *Nature Photonics* 4.12 (Nov. 2010), pp. 814–821 (cit. on p. 2).

[85]Lise Meitner. „Über die β-Strahl-Spektra und ihren Zusammenhang mit der γ-Strahlung“. In: *Zeitschrift für Physik* 11 (1922), pp. 35–54 (cit. on p. 21).

[86]Albert A. Michelson. „I. On the application of interference methods to astronomical measurements“. In: *The London, Edinburgh, and Dublin Philosophical Magazine and Journal of Science* 30.182 (July 1890), pp. 1–21 (cit. on p. 11).

[87]John Milnor. „Analytic proofs of the “hairy ball theorem” and the Brouwer fixed point theorem“. In: *The American Mathematical Monthly* 85.7 (1978), pp. 521–524 (cit. on p. 6).

[88]Johannes Möller, Mario Reiser, Jörg Hallmann, et al. „Implications of disturbed photon-counting statistics of Eiger detectors for X-ray speckle visibility experiments“. In: *Journal of synchrotron radiation* 26.5 (2019), pp. 1705–1715 (cit. on pp. 46, 95).

[89]A. Mozzanica, M. Andrä, R. Barten, et al. „The JUNGFRAU detector for applications at synchrotron light sources and XFELs“. In: *Synchrotron Radiation News* 31.6 (2018), pp. 16–20 (cit. on p. 44).

[90]Richard Neutze, Remco Wouts, David Van der Spoel, Edgar Weckert, and Janos Hajdu. „Potential for biomolecular imaging with femtosecond X-ray pulses“. In: *Nature* 406.6797 (2000), pp. 752–757 (cit. on pp. 84, 85).

[91]Keith A. Nugent. „Coherent methods in the X-ray sciences“. In: *Advances in Physics* 59.1 (2010), pp. 1–99 (cit. on p. 1).

[92]Dominik Oberthuer, Juraj Knoška, Max O. Wiedorn, et al. „Double-flow focused liquid injector for efficient serial femtosecond crystallography“. In: *Scientific reports* 7.1 (2017), pp. 1–12 (cit. on p. 43).

[93]Steffen Oppel, Thomas Büttner, Pieter Kok, and Joachim von Zanthier. „Superresolving multiphoton interferences with independent light sources“. In: *Physical review letters* 109.23 (2012), p. 233603 (cit. on p. 85).

[94]M. Ossiander, J. Riemensberger, S. Neppl, et al. „Absolute timing of the photoelectric effect“. In: *Nature* 561.7723 (Sept. 2018), pp. 374–377 (cit. on p. 32).

[95]M. Ossiander, F. Siegrist, V. Shirvanyan, et al. „Attosecond correlation dynamics“. In: *Nature Physics* 13.3 (Nov. 2016), pp. 280–285 (cit. on p. 32).

[96]David Paganin et al. *Coherent X-ray optics*. 6. Oxford University Press on Demand, 2006 (cit. on pp. 5, 7–9).

[97]Yong Woon Parc, Chi Hyun Shim, and Dong Eon Kim. „Toward the Generation of an Isolated TW-Attosecond X-ray Pulse in XFEL“. In: *Applied Sciences* 8.9 (2018) (cit. on pp. 2, 84).

[98]Nolan Peard, Kartik Ayyer, and Henry N. Chapman. „Ab Initio Spatial Phase Retrieval via Fluorescence Intensity Triple Correlations“. In: *arXiv preprint arXiv:2210.03793* (2022) (cit. on p. 85).

[99]Fivos Perakis, Gaia Camisasca, Thomas J Lane, et al. „Coherent X-rays reveal the influence of cage effects on ultrafast water dynamics“. In: *Nature communications* 9.1 (2018), p. 1917 (cit. on p. 46).

[100]Thomas Pfeifer, Yuhai Jiang, Stefan Düsterer, Robert Moshammer, and Joachim Ullrich. „Partial-coherence method to model experimental free-electron laser pulse statistics“. In: *Opt. Lett.* 35.20 (Oct. 2010), pp. 3441–3443 (cit. on p. 35).

[101]Wilhelm Conrad Röntgen. „Uber eine neue Art von Strahlen“. In: *Sitzung Physikal-Medicin Gesellschaft* 137 (1895), pp. 132–141 (cit. on p. 1).

[102]Beatrice Ruta, Y. Chushkin, Giulio Monaco, et al. „Atomic-scale relaxation dynamics and aging in a metallic glass probed by x-ray photon correlation spectroscopy“. In: *Physical review letters* 109.16 (2012), p. 165701 (cit. on p. 83).

[103]E.L. Saldin, E.A. Schneidmiller, and M.V. Yurkov. „Influence of nonlinear effects on statistical properties of the radiation from SASE FEL“. In: *Nuclear Instruments and Methods in Physics Research Section A: Accelerators, Spectrometers, Detectors and Associated Equipment* 407.1-3 (1998), pp. 285–290 (cit. on p. 51).

[104]E.L. Saldin, E.A. Schneidmiller, and M.V. Yurkov. „Statistical properties of radiation from SASE FEL driven by short electron bunches“. In: *Nuclear Instruments and Methods in Physics Research Section A: Accelerators, Spectrometers, Detectors and Associated Equipment* 507.1 (2003). Proceedings of the 24th International Free Electron Laser Conference and the 9th Users Workshop., pp. 101–105 (cit. on p. 35).

[105]Tom Schoonjans, Antonio Brunetti, Bruno Golosio, et al. „The xraylib library for X-ray–matter interactions. Recent developments“. In: *Spectrochimica Acta Part B: Atomic Spectroscopy* 66.11 (2011), pp. 776–784 (cit. on pp. 21–23).

[106]E. Schrödinger. „Quantisierung als Eigenwertproblem“. In: *Annalen der Physik* 385.13 (1926), pp. 437–490. eprint: `https://onlinelibrary.wiley.com/doi/pdf/10.1002/andp.19263851302` (cit. on p. 9).

[107]Marlan O. Scully and M. Suhail Zubairy. *Quantum Optics*. Cambridge University Press, Sept. 1997 (cit. on pp. 5, 16).

[108]M. Marvin Seibert, Tomas Ekeberg, Filipe RNC Maia, et al. „Single mimivirus particles intercepted and imaged with an X-ray laser“. In: *Nature* 470.7332 (2011), pp. 78–81 (cit. on p. 85).

[109]Stephen Seltzer. *XCOM-Photon Cross Sections Database, NIST Standard Reference Database 8*. en. 1987 (cit. on pp. 1, 73).

[110]David Shapiro, Pierre Thibault, Tobias Beetz, et al. „Biological imaging by soft x-ray diffraction microscopy“. In: *Proceedings of the National Academy of Sciences* 102.43 (2005), pp. 15343–15346 (cit. on p. 112).

[111]Yoav Shechtman, Yonina C. Eldar, Oren Cohen, et al. „Phase retrieval with application to optical imaging: a contemporary overview“. In: *IEEE signal processing magazine* 32.3 (2015), pp. 87–109 (cit. on p. 79).

[112]Andrew S.H. Shevchuk, John C.H. Spence, Richard A. Kirian, William S. Graves, and Kevin E. Schmidt. „Imaging by intensity interferometry of x-ray fluorescence at a compact x-ray free-electron laser“. In: *Phys. Rev. A* 104 (2 Aug. 2021), p. 023514 (cit. on p. 85).

[113]A.J.F. Siegert. „On the fluctuations in signals returned by many independently moving scatterers“. In: (1943) (cit. on pp. 12, 25).

[114]Michihiro Suga, Atsuhiro Shimada, Fusamichi Akita, et al. „Time-resolved studies of metalloproteins using X-ray free electron laser radiation at SACLA“. In: *Biochimica et Biophysica Acta (BBA)-General Subjects* 1864.2 (2020), p. 129466 (cit. on p. 85).

[115]Yanwen Sun, Jordi Montana-Lopez, Paul Fuoss, Mark Sutton, and Diling Zhu. „Accurate contrast determination for X-ray speckle visibility spectroscopy“. In: *Journal of Synchrotron Radiation* 27.4 (2020), pp. 999–1007 (cit. on pp. 46, 53, 95, 107).

[116]C. Thiel, Thierry Bastin, John Martin, et al. „Quantum imaging with incoherent photons“. In: *Physical review letters* 99.13 (2007), p. 133603 (cit. on p. 2).

[117]Joseph John Thomson. *Conduction of electricity through gases*. at the University Press, 1906 (cit. on p. 28).

[118]Eite Tiesinga, Peter J. Mohr, David B. Newell, and Barry N. Taylor. „CODATA recommended values of the fundamental physical constants: 2018“. In: *Journal of Physical and Chemical Reference Data* 50.3 (2021), p. 033105 (cit. on pp. 5, 28).

[119]Nikolai V. Tkachenko. *Optical spectroscopy: methods and instrumentations*. Elsevier, 2006 (cit. on p. 13).

[120]Fabian Trost. „Non-local and non-linear aspects of Fresneldiffractograms“. MA thesis. KIT, 2017 (cit. on p. 7).

[121]Fabian Trost, Kartik Ayyer, and Henry N. Chapman. „Photon statistics and signal to noise ratio for incoherent diffraction imaging“. In: *New Journal of Physics* 22.8 (Aug. 2020), p. 083070 (cit. on pp. 57, 63–67, 69–71, 100, 102–105, 131).

[122]Fabian Trost, Kartik Ayyer, Dominik Oberthuer, et al. „Speckle contrast of interfering fluorescence X-rays“. In: *Journal of Synchrotron Radiation* 30.1 (Jan. 2023) (cit. on pp. 28, 43–45, 48, 50–54, 95–98, 107, 108, 131).

[123]Fabian Trost, Kartik Ayyer, Mauro Prasciolu, et al. „Imaging via Correlation of X-Ray Fluorescence Photons“. In: *Phys. Rev. Lett.* 130 (17 Apr. 2023), p. 173201 (cit. on pp. 73–77, 79, 80, 112, 113, 131).

[124]R.Q. Twiss. „Applications of Intensity Interferometry in Physics and Astronomy“. In: *Optica Acta: International Journal of Optics* 16.4 (July 1969), pp. 423–451 (cit. on pp. 2, 61, 85).

[125]P.H. van Cittert. „Kohaerenz-probleme“. In: *Physica* 6.7 (1939), pp. 1129–1138 (cit. on p. 11).

[126]P.H. van Cittert. „Zum Einfluß der Spaltbreite auf die Intensitätsverteilung in Spektrallinien“. In: *Zeitschrift für Physik* 65.7-8 (July 1930), pp. 547–563 (cit. on p. 11).

[127]P.H. van Cittert. „Zum Einfluß der Spaltbreite auf die Intensitätsverteilung in Spektrallinien. II“. In: *Zeitschrift für Physik* 69.5-6 (May 1931), pp. 298–308 (cit. on p. 11).

[128]D.F. Walls and G.J. Milburn. *Quantum Optics*. Springer Berlin Heidelberg, 1994 (cit. on pp. 5, 16).

[129]H.E. White. *Introduction to Atomic Spectra*. Ballard CREOL collection. McGraw-Hill book Company, Incorporated, 1934 (cit. on pp. 22, 32).

[130]Klaus Wille. *Introduction to insertion devices*. 1998 (cit. on p. 28).

[131]Thomas Young and Thomas Young. *A course of lectures on natural philosophy and the mechanical arts*. Printed for J. Johnson, 1807 (cit. on p. 14).

[132]Frits Zernike. „The concept of degree of coherence and its application to optical problems“. In: *Physica* 5.8 (1938), pp. 785–795 (cit. on pp. 11, 15).

List of Figures

List of Tables

Author contributions

The chapters Chapter 3, Chapter 4, and Chapter 5 are based on the following publications. The respective author contributions of the published papers are as follows:

- Chapter 3 is based on Trost et al. Speckle contrast of interfering fluorescence X-rays. J. Synchrotron Rad. 30, 11–23. (2023) [122]
  Author contributions:

  F.T., K.A., J.v.Z., R.R., and H.N.C. designed the experiment. D.O., A.W., A.F., and H.W. provided the sample. **F.T.**, A.K., D.O., O.Y., C.C., S.B., J.K., J.v.Z., R.R., and H.N.C. participated in the data collection. **F.T.** performed the data analysis. The manuscript was written by **F.T.** with input from A.K. and H.N.C. and all co-authors.

- Chapter 4 is based on Trost et al. 2020 New J. Phys. 22 083070 (2020) [121]
  Author contributions:

  F.T. developed the theory (with inputs fom A.K. and H.N.C.) and performed the simulations. The manuscript was written by **F.T.** with input from A.K. and H.N.C.

- Chapter 5 is based on Trost et al. Phys. Rev. Lett. 130, 173201 (2023) [123]
  Author contributions:

  F.T., K.A., N.T., C.C., R.R., J.v.Z., H.N.C. designed the experiment. H.F. and **F.T.** designed, build and tested the experimental setup. M.P., M.B. and S.B. provided the beam shaping samples. K.A., C.L., T.W., A.M., Z.S., and Y.Z., S.C. performed the 'fast feedback data analysis'. **F.T.**, J.L.D., S.S., S.K., K.K.P., J.M., A.Z., R.S., W.L., F.B., B.F., U.B., I.P., S.T., M.G., participated in the data collection. The (final) data analysis was performed by **F.T.** with input from K.A.. The manuscript was written by **F.T.** with input from H.N.C. and all co-authors.

Acknowledgments

First and foremost, I would like to express my deepest gratitude to my PhD supervisor Henry N. Chapman for providing me with the opportunity to successfully carry out this fascinating project. I am especially thankful for the insightful discussions and the support for writing the papers. Working in his group has been a truly memorable experience that will stay in good memory.
My sincere thanks also go to Kartik Ayyer, who supported me throughout the whole project and especially for providing me with a smooth start.
A special thanks goes to my colleagues Holger Fleckenstein and Mauro Prasciolu for their help with the setup and samples for my final experiment.
I would also like to thank Wolfgang Brehm and all my colleagues for the great discussions and their support.
Lastly, I would be remiss in not mentioning my parents Beate and Markus Trost, my girlfriend Nato Gogichashvili, and all of my friends for providing me with unfailing support and continuous encouragement throughout my years of study and through the process of writing this thesis.

Eidesstattliche Versicherung / Declaration on oath

Hiermit versichere ich an Eides statt, die vorliegende Dissertationsschrift selbst verfasst und keine anderen als die angegebenen Hilfsmittel und Quellen benutzt zu haben.

Hamburg, den 25.09.2023

Fabian Trost